

UNIVERSITY OF CALIFORNIA
Santa Barbara

Modelling and Control of Electrostatically Actuated Microcantilever Arrays

A Dissertation submitted in partial satisfaction of the
requirements for the degree Doctor of Philosophy
in Mechanical Engineering

by

Maria Teresa Napoli

Committee in charge:

Professor Bassam Bamieh, Chair

Professor Kimberly Turner

Professor Igor Mezić

Professor Roy Smith

March 2004

The dissertation of Maria Teresa Napoli is approved:

Kimberly Turner

Igor Mezić

Roy Smith

Bassam Bamieh, Committee Chair

March 2004

*to the memory of Mohammed Dahleh
and to my parents*

A rock pile ceases to be a rock pile the moment a single man
contemplates it, bearing within him the image of a cathedral.
-Antoine de Saint-Exupery, author and aviator (1900-1945)

Modelling and Control of Electrostatically Actuated Microcantilever
Arrays.

Copyright ©2004

by

Maria Teresa Napoli

Maria Teresa Napoli

EDUCATION

Ph.D. in Mechanical Engineering — UC Santa Barbara February 2002

Major in Dynamic Systems and Control.

Advisor: Professor Bassam Bamieh

Ph.D. in Electrical Engineering — Universita' di Padova February 2000

Emphasis in Systems Theory and Control

Advisor: Professor Mauro Bisiacco

B.Tech. in Electrical Engineering — Universita' di Padova July 1995

Emphasis in Control Theory

Advisor: Professor Mauro Bisiacco

ACADEMIC EXPERIENCE

Teaching Assistant 1998 ~ 2002

Held office hours and tutorial sessions, and graded homework and exams in the following graduate and undergraduate courses:

Control Systems, Automotive Design, Numerical methods, Linear Systems I - II.

Research Assistant 1998 ~ Present

Worked on control and dynamical systems theory research. It involved fabrication and modelling of multicantilever arrays, fabrication of SEM tips and AFM imaging, experimental charac-

terization of electrostatically actuated microcantilevers,
observer based design of decoupling controller, design of current measuring circuit.

ACADEMIC AREAS OF SPECIALIZATION

• Supporting Coursework

Mathematics: Real Analysis, Functional Analysis, Hilbert Spaces.

Control Systems: Linear System Theory, Robust Control Theory, Nonlinear Systems, Optimal Control, Infinite Dimensional Systems and Control, Stochastic Control.

Dynamical Systems: Classical Mechanics, Dynamical Systems, Advanced Dynamical Systems.

Fabrication And MEMS: Semiconductor Design, Introduction to MEMS, MEMS Analysis and Design.

• Research Areas

Atomic Force Microscopy, Spatially Invariant Distributed Parameters Systems, Optimal Control of Distributed Systems, Microfabrication, Modelling and Control of MEMS.

Publications

Characterization of Electrostatically Coupled Microcantilevers, M. Napoli, W.Zhang, K.Turner and B.Bamieh, submitted to JMEMS, January 2004.

Design of a Decoupling Controller for Electrostatically Coupled Microcantilevers using Current Measurements, M. Napoli, B.Bamieh, to appear Proc. 2004 American Control Conference, June 2004, Boston MA, USA.

A Capacitive Microcantilever : Modeling, Validation and Estimation Using Current Measurements, M. Napoli, B.Bamieh and K.Turner, to appear ASME Journal of Dynamic Systems Measurement and Control, June 2004.

Dynamics of Mechanically and Electrostatically Coupled Microcantilevers, M. Napoli, W.Zhang, K.Turner and B.Bamieh, Proceedings of 12th Int. Conf. On Solid-State Sensors, Actuators and Microsystems, June 2003, Boston MA, USA.

Mathematical Modeling, Experimental Validation and Observer Design for a Capacitively Actuated Microcantilever, M. Napoli, B.Bamieh and K.Turner, Proceedings of 2003 American Control Conference, June 2003, Denver CO, USA.

Understanding Mechanical Domain Parametric Resonance in Microcantilevers, M. Napoli, R.Baskaran, K.Turner and B.Bamieh, Proceedings of 16th IEEE Annual Int, Conf. On Micro Electro Mechanical Systems, January 2003, Kyoto Japan.

Modeling and Observer Design for Array of Electrostatically Actuated Cantilevers, M. Napoli and B.Bamieh, Proceedings of 40th IEEE Conference on Decision and Control, December 2001, Orlando FL, USA.

2D Proper Rational Matrices and Causal I/O Representations of 2D Behavioral Systems, M. Napoli, S.Zampieri, SIAM J. Contr. Opimt., Volume 37, No. 5, Pages 1538 - 1552, 1999.

Optimal Control of Arrays of Microcantilevers, M. Napoli, B.Bamieh, and M.Dahleh, ASME Journal of Dynamic Systems Measurement and Control, Volume 121, Pages 686 - 690, Dec. 1999.

Optimal Control of Arrays of Multicantilevers, M. Napoli, B.Bamieh

and M. Dahleh, Proceedings of 37th IEEE Conference on Decision and Control, December 1998, Tampa FL, USA.

H2 - Norm Minimization for Distributed Continuous Time Systems : an Input/Output Approach, M. Napoli, B.Bamieh and M. Dahleh, Proceedings of 1998 Mathematical Theory of Networks and Systems, July 1998, Padova, Italy.

Causality of 2D Input/Output Representations in the Behavioral Approach, M. Napoli and S.Zampieri, Proceedings of 1998 MTNS, July 1998, Padova, Italy.

ABSTRACT

Modelling and Control of Electrostatically Actuated Microcantilever
Arrays.

by

Mariateresa Napoli

In this dissertation we present the design, modelling and analysis of a device consisting of an array of tightly packed electrostatically actuated microcantilevers. More precisely, each microcantilever in the array constitutes the movable plate of a capacitor and its displacement is controlled by the voltage applied across the plates. We show that, if we take the current as the measured signal, the dynamics of a single cantilever are governed by a special second order linear periodic differential equation, called the Mathieu equation. As for the array configuration, by explicitly incorporating the mechanical and electrostatic coupling into the dynamical equations, we show that the system is described by a set of coupled Mathieu equations. The structural properties of the array, with actuators and sensors distributed over a regular lattice, allow us to cast it in the class of *spatially invariant distributed parameter* systems, which bears important consequences in the rest of the analysis. Both models, for the single cantilever and for the array, are validated through an extensive set of experiments, which demonstrate very good agreement between theoretical predictions and experimental findings.

We propose a novel sensing scheme for the cantilevers' displacement, based on the design of an optimal state observer whose input is the current

through the capacitive cantilevers. We demonstrate in simulations its excellent performance in reconstructing the cantilevers displacement within few nanometers from its actual value. We propose a procedure that uses the optimal design as an analysis tool to tune both the frequency of excitation of the cantilevers and the parameters of a reduced order observer. This way we obtain a system with the best achievable noise rejection properties, measured in terms of \mathcal{H}_∞ -norm of the closed loop system.

The problem of controlling tightly packed arrays of microcantilevers is presented in two case studies, in which the microcantilever arrays considered differ in the model of the coupling interactions. We consider the design a controller for the electrostatically actuated array that, by using the estimate of the cantilever displacement provided by an observer, is able to decouple the cantilevers' dynamics. Simulation results are provided to illustrate its performance. Finally, we present an optimal \mathcal{H}_2 control design for different array of cantilevers and discuss the synthesis of suboptimal controllers.

Contents

Vita	v
Abstract	ix
List of Figures	xiv
1 Introduction	1
1.1 Why MEMS and beams are interesting	1
1.2 Contributions	2
1.3 How the Work Developed	6
1.4 Outline	12
2 System Theory	14
2.1 Optimal Control for Periodic Systems	15
2.2 The Lifted System	19
2.3 Linear Spatially Invariant Distributed Systems	25
3 Parametric resonators	28
3.1 Micro-Oscillators	29

3.2	The Mathieu Equation	31
3.2.1	Perturbation Analysis for the Mathieu Equation	35
3.3	Coupled Mathieu Equations	40
4	Device Design and Fabrication	47
4.1	Fabrication : PolyMUMPS Process	48
4.2	Device and Mask Design	51
5	Mathematical Model	57
5.1	Single Cantilever Model	58
5.2	Multicantilever Model	61
6	Experimental Characterization of the Device	66
6.1	Testing Technique Using a Vibrometer	67
6.2	Testing of a Single Cantilever	68
6.2.1	Combined Harmonic-Parametric Response	83
6.3	Testing of a Pair of Cantilevers	86
6.3.1	Linear Regime of Operation	88
6.3.2	Parametric Resonance	96
7	Observer Design	103
7.1	Optimal Observer Design	103
7.2	The Reduced Order Observer	120
8	Control Design	128
8.1	Decoupling Controller for Arrays of Electrostatically Actuated Cantilevers	129

8.2	Optimal Control for an Array of Microcantilevers	136
8.2.1	Mathematical Model of Microcantilever Arrays with Sample Interaction	138
8.3	\mathcal{H}_2 Optimal Controller	142
8.4	Suboptimal Controllers and Communication Range	144
9	Conclusions and Future Directions	149
9.1	Conclusions	149
9.2	Future Directions	151
A	On the Implementation of the Observer	153
A.1	The Current Measurement	153
A.2	Circuit Design	154
A.3	Offline Implementation of the Observer	156

List of Figures

1.1	A partial SEM image of one of our arrays of electrostatically actuated microcantilevers.	3
1.2	SEM image of Si_3N_4 cantilevers, fabricated in the cleanroom facilities at UCSB.	7
1.3	Image of tip grown by electron beam deposition using SEM.	8
1.4	Double tip caused by drift of the electron beam.	9
1.5	Image of the calibration grid obtained by using our tips. Notice how the image of each square in the pattern is repeated several times: an artifact attributed to the presence of multiple tips.	10
1.6	Image of the calibration grid obtained by using DI tips. . .	11
1.7	AFM image of the atomic lattice of mica. a) Top image showing exagonal arrangement of atoms (inter-atomic distance $\approx 5 \text{ \AA}$; b) 3-D representation of same data.	11
2.1	Schematic representation of lifting for a continuous time signal.	20
2.2	Schematic representation of fast sampling for lifted signals.	21

2.3	Schematic of a spatial invariant structure. The dashed lines represent some form of internal coupling (not necessarily nearest neighbor). All the units are identical and can be independently sensed and actuated.	26
3.1	Mathieu equation: the shaded areas correspond to unstable behavior.	36
3.2	Exponential growth of the signal at the transition from non-parametric to parametric region of oscillation. The simulation used the cantilever parameters.	39
3.3	Variation of oscillation amplitude with a_1 (i.e. driving frequency for a cantilever) across the first region of parametric amplification. The ‘+’ symbols correspond to increasing values of a_1 (frequency is swept up), the ‘o’ to decreasing values (frequency being swept down). The simulation used the cantilever parameters.	40
3.4	Phase portrait of equation (3.18) for different values of perturbation parameter a_1	41
3.5	Schematic representation of the conditions corresponding to a possible loss in stability for two coupled Mathieu equations.	43
3.6	First region of parametric amplification for coupled Mathieu equations. The shaded areas correspond to unstable behavior. N denotes the number of coupled equations considered.	46

4.1	Final design for multicantilever array. The top plates are connected to a sturdy anchor, while the bottom plates are electrically isolated.	51
4.2	Initial design for multicantilever array. All cantilevers are electrically isolated and closely spaced.	52
4.3	Micrograph showing the typical geometry of one of the arrays fabricated with PolyMUMPs.	52
4.4	Micrograph showing the overhang between anchor and cantilevers base, responsible for the strong mechanical coupling.	53
4.5	Micrograph showing an array with about half of the cantilevers correctly released and half touching the bottom plates (a phenomenon known as stiction).	54
4.6	Micrograph showing the gap between top and bottom plates of each cantilever capacitor.	55
4.7	Close up image of one of the cantilever arrays. The lines visible are the electrical connections between bottom plates and metal pads.	56
5.1	A schematic of an electrostatically driven cantilever.	58
5.2	A schematic of the multicantilever array.	61
5.3	A schematic of the coupling capacitance model.	63
6.1	Schematic of the experimental setup, courtesy of [1].	67
6.2	SEM image of a polySi cantilever. The inset shows details of the mechanical connection to the base.	69
6.3	Variation of Q with pressure p	70

6.4	Frequency response of the cantilever: the solid line corresponds to measured data, the dashed one is its least square fit.	71
6.5	Analysis of cantilever response to a step input of amplitude $A = 50 V$. a) Full trace showing exponential decay; b) detail showing oscillation at natural resonant frequency. The red line represents the input in arbitrary units.	73
6.6	Experimental identification of the electrostatic resonance. The circles represent measured values of resonance frequency, the solid line is their linear fit.	74
6.7	Effect of cubic nonlinearity on the frequency response of the cantilever. The dots denote experimental data, the solid lines their fit. Notice how the curve tilts on one side as the effect of the cubic term becomes no longer negligible. . . .	75
6.8	Effect of cubic nonlinearity on the frequency response of the cantilever. The circles correspond to data collected by sweeping the frequency from low to high, the asterisks to data collected by sweeping the frequency from high to low.	76
6.9	Experimental identification of the coefficient of cubic stiffness. Squares denote experimental data, solid lines their fit.	77
6.10	First instability region: experimental data points (circles) and curves with identified parameters. The inset shows the upward shift of the tongue caused by damping.	80

6.11	Time series of typical input and output signals inside the first “tongue” (oscilloscope data). Note the response is at half the driving frequency.	81
6.12	Exponential growth of oscillation following parametric excitation. Experimental data.	82
6.13	Frequency response above critical driving voltage amplitude ($A = 10 V$). The solid and dashed lines have been added to the experimental data points (marked with ‘o’ and ‘+’) to facilitate the reading.	83
6.14	Combined harmonic/parametric frequency response. Note that there are bistable regions (I and III) on either side of the parametric tongue (II).	84
6.15	The first instability region with combined harmonic and parametric excitation. Note that at the boundary between regions I and II, there is still a distinctly sharp transition between small and large amplitude response, making it useful for applications.	85
6.16	SEM micrograph of the device. The insets show details of the mechanical connection to the base and between the cantilevers.	87
6.17	Magnitude of the frequency responses of the coupled cantilevers with different input/output combinations. The circles represents experimental data; the solid line the fitted data.	90

6.18	Fit of PSD of thermal noise to determine Γ : a) cantilever 1, b) cantilever 2. The region between the two peaks is below the noise level of our instrumentation. c,d) Experimental characterization of noise distribution (10^4 samples of the noise signal at the vibrometer output).	93
6.19	Experimental estimation of the electrostatic coefficients. K_{ij} are the coefficients of the electrostatic coupling force, $F_{ec,i}$; K_e is the coefficient of the attractive force, $F_{e,i}$, between the cantilever and its ground plate.	94
6.20	Ansys model of the cantilever pair a), and of the single cantilevers b,c).	95
6.21	First region of coupled parametric amplification, with the electric signal applied to one cantilever only. The three tongues correspond respectively to a) $\omega = 2w_{pk1}$; b) $\omega = 2w_{pk2}$; c) $\omega = w_{pk1} + w_{pk2}$. Picture d) shows the exponential growth of the output inside the region of parametric amplification.	98
6.22	Frequency response above critical driving voltage : a) single cantilever b) coupled cantilevers in region a) of Figure(6.21).	99
7.1	A block diagram of the observer problem.	105
7.2	\mathcal{H}_∞ -norm vs. frequency of excitation for the lifted, fast sampled system.	107
7.3	H_∞ -norm vs. frequency of excitation with a causal observer.	109
7.4	A schematic of the observer. The dashed lines represent the coupling interaction.	110

7.5	Comparison of the performance of the observers defined by P_4 (part b,d) and P_i , $i = 1, 2$ (part a,c) during transient. The plots in a,b) refer to cantilever 1, the plots c,d) to cantilever 2. Notice how the transient of the two observer schemes is not significantly different.	113
7.6	Estimation error at steady state. Parts a,b) refer to cantilever 1, parts c,d) to cantilever 2. Note that the vertical scale is in pm.	114
7.7	Comparison between the components of P_i , $i = 1, 2$ (solid lines) and the corresponding elements of the diagonal blocks \mathbf{P}_{ii} , $i = 1, 2$ of P_4 (circles).	115
7.8	Components of P_4 . The solid lines represent the components that P_4 has in common with P_1, P_2 , also shown in Figure 7.7. The dashed lines are the components of P_4 belonging to the extra diagonal blocks \mathbf{P}_{12} and \mathbf{P}_{21}	116
7.9	Schematic of the distributed observer.	118
7.10	Schematic representation of the small gain theorem for the infinite dimensional array.	120
7.11	Performance of the observers in the presence of measurement noise and initial estimation error. The dashed line is the measured position signal, the solid line its estimate. a) Optimal observer b) Reduced order observer.	124
7.12	Components of $P(t)$	125
7.13	Expected current signal from experimental velocity and position data.	126

7.14	Estimation error for different values of the observer gain: a) $k > 0 \cos(\phi) < 0$, b) $k < 0 \cos(\phi) > 0$	127
8.1	Schematic of the observer based decoupling controller. The dashed lines represent internal coupling.	130
8.2	Steady state oscillation of Cantilever 1 (a) and Cantilever 2 (b) with detail of the transient when the controller is switched on. The solid line is the cantilever oscillation, the dotted line its estimate. Notice the fast transient of the observer.	131
8.3	Oscillation of Cantilever 1 (a) and Cantilever 2 (b) after the controller is switched on, showing the controller transient. This longer transient is dominated by the system's time constant.	132
8.4	Comparison between the decoupled cantilevers oscillation and identical single (uncoupled) cantilevers subject to the same external inputs : a) Cantilever 1, b) Cantilever 2. The solid line represents the decoupled cantilevers oscillation, the dotted line the uncoupled cantilevers oscillation.	133
8.5	Decoupling error (entire trajectory and detail). Note that the scale is nm.	134
8.6	Simulation of sensor noise: current on both cantilevers. . .	135
8.7	Comparison between decoupled and uncoupled oscillation of same cantilevers in the presence of measurement noise. . .	136
8.8	Decoupling error in the presence of measurement noise (entire trajectory and detail).	137

8.9	Comparison between decoupled and uncoupled oscillation of same cantilevers with a reduced order observer.	138
8.10	Decoupling error with a reduced order observer.	139
8.11	A schematic of a multicantilever structure.	141
8.12	Variation of the minimum and maximum modulus singularities.	147
8.13	Variation of the minimum and maximum modulus singularities.	148
A.1	Schematic diagram of the circuit to measure the current. .	155
A.2	Picture showing the PCB and the cantilever die during testing.	155
A.3	a) Circuit output due to $i_{mot} =$, b) Comparaision between estimated (solid line) and measured (dashed line) cantilever displacement.	157

Chapter 1

Introduction

1.1 Why MEMS and beams are interesting

In recent years we have experienced a strong trend towards miniaturization. This trend results partly from the fact that small components can perform tasks that large systems cannot. One fascinating example is offered by microsurgical tools, which allow for new medical operation procedures that are not feasible with conventional methods [2, 3, 4]. At the same time, technology driven from IC-fabrication processes allows the production of miniature components in large volumes and at low prices.

In particular, over the past years, cantilever-based devices have proven to be extremely versatile instruments for applications that include, but are not limited to, high resolution (atomic scale) surface imaging [5, 6, 7, 8, 9], high density (Gb/cm^2) data storage and retrieval [8, 10, 11, 12], optical lithography for advanced device processing [13, 14, 15, 16], biosensors for recognition of biomolecular interactions [17, 18], and chemical sen-

sors [19, 20, 17, 18]. Cantilever transduction provides several principle advantages over other solid-state sensors, namely fabrication simplicity, sensitivity and easy implementation of array architectures. The sensitivity is better than that of other resonant designs because of the low mass and thickness (compared for example to quartz-crystal microbalances and surface-acoustic-wave sensors). Additionally, arrays of cantilevers can readily be fabricated on single silicon chips, allowing mass production.

In order to increase the throughput of microdevices research has evolved along two main lines: the integration of sensors and actuators [21, 22, 23, 24, 25, 26, 27, 28], and the use of array architectures of the probes [23, 24, 29, 11, 12, 9, 8]. The device that has been the object of study in this thesis combines both approaches and consists of an array of independently electrostatically actuated microcantilevers.

Figure 1.1 is a micrograph of one of our devices, which consist of polysilicon cantilevers. Each microcantilever in the array constitutes the movable plate of a capacitor and its displacement is controlled by the voltage applied across the plates. More details about geometric and material characteristics of the devices can be found in Chapter 4.

1.2 Contributions

The novelties in the device considered and the contributions of this thesis are the following:

- **System Design.** Currently, microcantilever arrays are designed with large spacing between the individual elements. This essentially

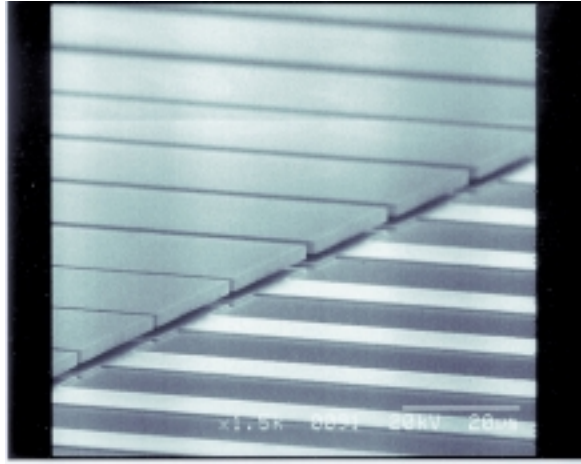


Figure 1.1: A partial SEM image of one of our arrays of electrostatically actuated microcantilevers.

decouples the dynamics of the individual cantilevers that can be considered to behave as isolated units. The drawback of this configuration is a decrease in the potential throughput of the device. Our research has focused on the design and analysis of a tightly packed array of microcantilevers. Indeed, the close spacing and the fact that the cantilevers are connected to a common base introduces a coupling in their dynamics, which is both electrostatic and mechanical. We show how this coupling adds features to the device, which are interesting from an engineering point of view. Moreover we show how it can be removed, when not desired, by an appropriate control action.

- **Mathematical Modelling and Experimental Validation.** Starting from physical principles we develop a model that describes the

dynamics of the cantilever array, including mechanical and electrostatic coupling. For the common case of sinusoidal excitation, we show that the system is governed by a multivariable nonlinear Mathieu equation with coupling. The structural properties of the device, with actuators and sensors distributed over a regular lattice, allow us to regard it as an example of *spatially invariant distributed parameter* system. This observation has important consequences. As a matter of fact, by exploiting the spatial invariance of the problem it is possible to analyze its stability properties and determine existence and location of the regions of parametric amplification. The mathematical model is validated with experiments that include a mapping of the first instability region of the Mathieu equation, both for a single cantilever and for a pair of coupled cantilevers. While parametric amplification has been discussed in small scale resonant systems [30, 31, 32, 33, 34, 35], to our knowledge this is the first experimental mapping of the first parametric instability region in microcantilever resonators [36, 37].

- **Use of an Indirect (Observer Based) Scheme for Cantilever Displacement Detection.** One of the main goals of our research project has been the design of a dynamical system that is capable of providing an estimate of the cantilever displacement, based on the measurement of the current through the cantilevers. This approach, which we call “indirect” sensing, has the advantage of allowing for compact devices by removing the usually cumbersome apparatus used in optical sensing techniques [38, 39, 40, 1].

To this end, capacitive detection offers a major advantage by providing both electrostatic actuation as well as integrated detection, without the need for an additional position sensing device. The common scheme used in capacitive detection is to apply a second AC voltage at a frequency much higher than the mechanical bandwidth of the cantilever. The current output at that frequency is then used to estimate the capacitance, and consequently the cantilever position [41, 42, 43]. This sensing scheme is the simplest position detection scheme available, however, it is widely believed to be less accurate than optical levers or piezoresistive sensing. We propose a novel scheme that avoids the use of a high frequency probing signal by the use of a dynamical state observer whose input is the current through the capacitive cantilever. For the purpose of implementation, this scheme offers significant advantages as it involves simpler circuitry. By using an optimal observer, or by tuning the observers gains, it is conceivable that a high fidelity position measurement can be obtained, thus improving resolution in atomic force microscopy applications. Simulation results are provided that confirm the theoretical predictions.

- **Control Design.** In order to increase the throughput of a multi probe device, it is desirable to have the largest number of probes in the smallest possible space. On the other side, the proximity of the probes induces coupling in their dynamics, which increases the complexity of the overall device and, depending on the application, can deteriorate its performance.

By explicitly incorporating coupling into the model equations, we show how it is possible to design controllers that “electronically diagonalize” the system. The important consequence of this approach is that we do not need to impose constraints on the geometrical parameters of the device (in particular, the lateral spacing between cantilevers) to obtain decoupled dynamics. It is the controller that allows us to recover this property and that “diagonalizes” the system. We consider two control problems: a decoupling controller for the electrostatically actuated array and an optimal controller for a different multicantilever structure. In both cases we propose a novel architecture, where the overall controller is distributed, thus reflecting the structure of the device.

1.3 How the Work Developed

Prof. Dahleh’s lab had owned an Atomic Force Microscope (AFM) for a few years already when I first arrived at UCSB in 1997. Many of his students were or had been involved in research projects regarding the AFM, and sure enough I was soon involved too. At that time research on scanning probe instruments was exploring the problem of the parallelization of probes. We started by considering modelling and control issues for an array configuration of scanning probes [44].

In 1999 Prof. Dahleh became interested in having one such device for experimental investigations. This is how I started working at the fabrication of an array of cantilevers, under the guidance of Dr. Ami Chand (now

at VEECO, Inc.). In November of that year we produced our first set of cantilevers. Figure 1.2 shows one of them. The array in the figure consists

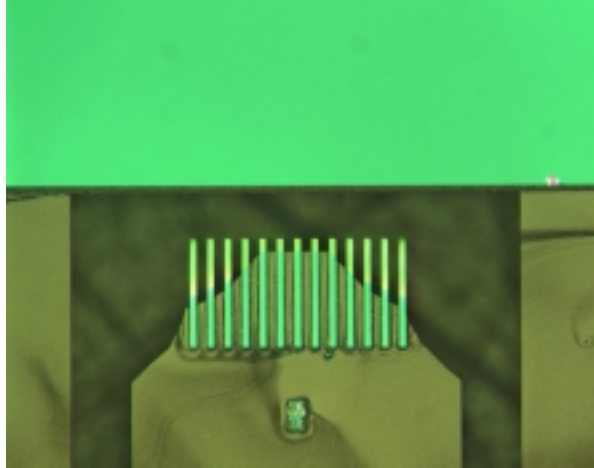


Figure 1.2: SEM image of Si_3N_4 cantilevers, fabricated in the cleanroom facilities at UCSB.

of thirteen Si_3N_4 cantilevers of different lengths, $30\mu m$ wide, $1\mu m$ thick and $50\mu m$ apart. The process used two masks and backside etching for the release of the microbeams.

Initially, we had planned to make the structure active by depositing piezoelectric material and implementing the controller that we had studied previously [44]. However, this idea was temporarily set aside and we decided to grow tips by electron beam deposition on our cantilevers, using a Scanning Electron Microscope (SEM). It was already known that these tips, grown out of the vacuum residual gases of an SEM, were sharper, much taller and harder than those obtained by conventional fabrication

methods [45, 46, 47]. However, we were not interested in improving the process and/or the tip characteristics. Our idea was to use the tips as part of a deconvolution algorithm to reconstruct more accurate images from data collected by commercial (blunter) tips.

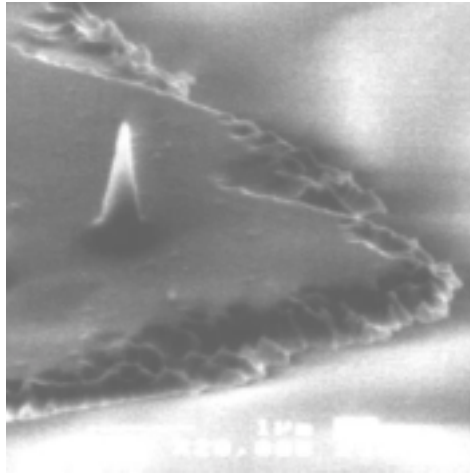


Figure 1.3: Image of tip grown by electron beam deposition using SEM.

The deposition process was successful and Fig.1.3 shows one of the tips obtained. The irregular profile of the cantilever edges, visible in the picture, is caused by residuals of paraffin oil used to start the growth process. The procedure turned out to be quite challenging. A significant drift of the electron beam was noticed, with the effect of changing the initial area of growth, leading to the deposition of a second neighbor tip, as shown in Fig.1.4.

However, even when this problem was overcome, the tips turned out to be not utilizable. Eventually we had to surrender to the fact that we could not exactly center the tips on the cantilever, at least not with our

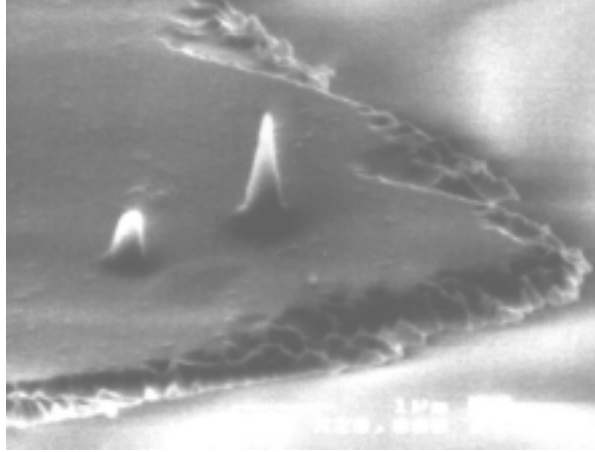


Figure 1.4: Double tip caused by drift of the electron beam.

design of the probes. The asymmetry in the placement caused torsion in the cantilever, while scanning in contact mode, resulting in a distortion of the image. Figure 1.5 is the image of a calibration grid obtained with our tips and it should be compared to Fig.1.6, which shows the same grid imaged with a commercial tip. It can be noted that the image of each element of the grid in Fig.1.5 is repeated several times : a kind of image aberration that is usually attributed to a double or multiple tip [48].

Simultaneously, and for the same project, I was trying to become more familiar with the AFM. Obtaining images with atomic resolution proved to be a much harder task than expected. In the end, the critical issue turned out to be the isolation of the instrument from any source of vibrations. After trying several arrangements (floating platform, vibration isolation table), the problem was finally solved by moving the AFM on the ground floor of the Engineering building. Figure 1.7 shows an image of the atomic

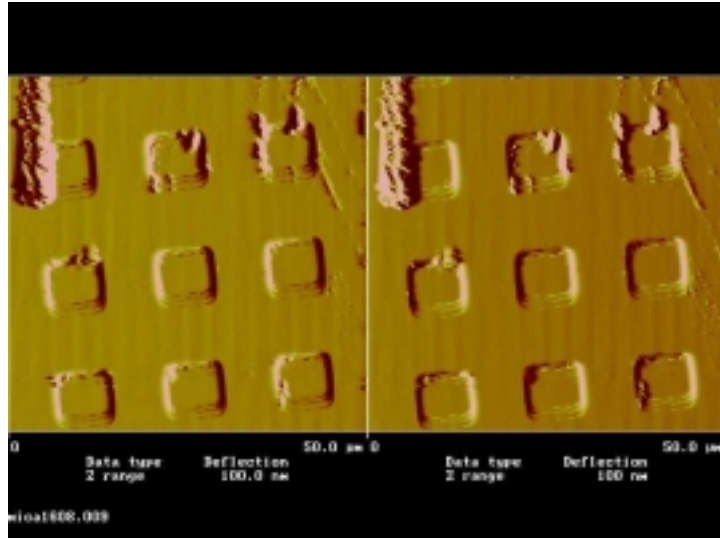


Figure 1.5: Image of the calibration grid obtained by using our tips. Notice how the image of each square in the pattern is repeated several times: an artifact attributed to the presence of multiple tips.

lattice of mica that I was able to obtain afterwards.

By the end of 2001 we resumed work on our original project, which dealt with control of cantilever arrays. At this time, though, we were thinking of capacitive actuation. We have preferred capacitive actuation over other integrated schemes (e.g. piezoelectric [23, 24, 49], piezoresistive [21, 25], thermal [26]) because it offers both electrostatic actuation as well as integrated detection, without the need for an additional position sensing device. Moreover, in contrast to piezoelectric films, which had been our first choice, capacitive actuation is compatible with IC manufacturing techniques: an important property when we have the integration of the device with control circuitry in mind.

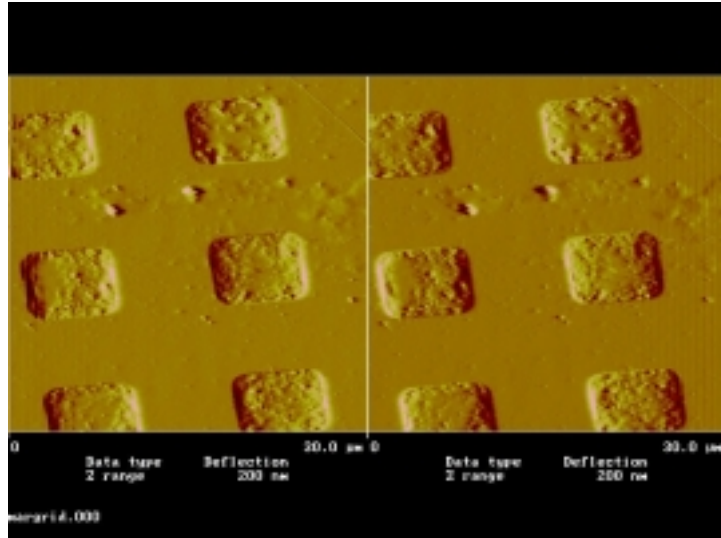
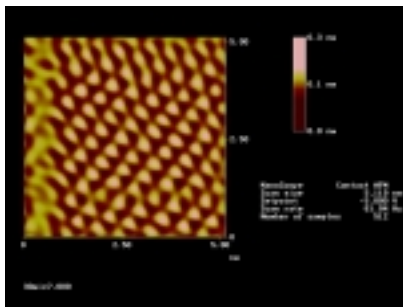
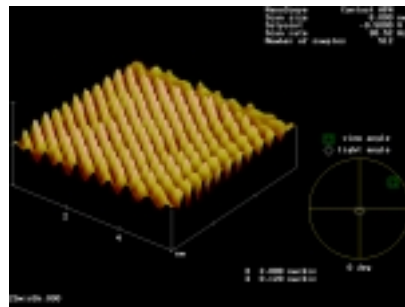


Figure 1.6: Image of the calibration grid obtained by using DI tips.



a)



b)

Figure 1.7: AFM image of the atomic lattice of mica. a) Top image showing exagonal arrangement of atoms (inter-atomic distance $\approx 5 \text{ \AA}$; b) 3-D representation of same data.

1.4 Outline

This dissertation is organized as follows. Chapter 3 offers a brief introduction to the topic of MEMS sensors and the phenomenon of parametric resonance. We introduce the Mathieu equation, which will turn out to play an important role in the modelling of our device, and discuss its stability properties. In Chapter 2 we present some relevant mathematical tools and theoretical results that will be applied to the analysis of the multicantilever device. We introduce the theory of optimal filtering for periodic systems that will be used for the design of an optimal observer based on current measurements. The concept of lifting for periodic systems is presented. We use this transformation to measure the performance (in terms of I/O norm) of a time-varying system, by associating it with an equivalent discrete time-invariant system. Finally, we present the theory of spatially invariant distributed systems, which is used to model the dynamics of an array of coupled cantilevers. In Chapter 4 we describe the PolyMUMPS fabrication process, which was used to fabricate the multicantilever device. We discuss also some of the design choices that were made regarding the configuration of the arrays and some of the geometrical parameters of the cantilevers. The mathematical model that we propose to describe the dynamical behavior of electrostatically actuated cantilevers is presented in Chapter 5. In particular, we consider separately the case of a single cantilever and that of an infinite dimensional array. In Chapter 6 we illustrate the results of the experiments performed to characterize the cantilevers and to validate the model proposed, both in the linear regime of operation and in parametric resonance. The experiments were performed on a

single cantilever and on pairs of coupled cantilevers. Chapter 7 describes the design of both optimal and reduced order observers. Simulation results demonstrate their ability to reconstruct the cantilever displacement from a current measurement. In a real implementation we expect that by an optimal tuning of the observers parameters we would be able to obtain same or better measurement precision than in the commonly used optical apparatuses. Finally, in Chapter 8 we show how the dynamics of coupled cantilevers can be “electronically diagonalized” by the use of an appropriate control action. The concept of electronic decoupling is illustrated through two examples: an optimal \mathcal{H}_2 design and a decoupling controller. The multicantilever arrays considered in the two cases differ in the model of the coupling interactions. In both cases, we show that by means of a distributed controller, we do not need to impose constraints on the geometrical parameters of the device (in particular, the lateral spacing between cantilevers) to obtain decoupled dynamics. It is the use of control that “diagonalizes” the system.

*

Chapter 2

System Theory

In this chapter we introduce the mathematical tools and discuss some theoretical results that will be applied to the analysis of the multicantilever device. The challenge in this task originates essentially from two factors. First of all, the dynamics of each single cantilever are time-varying. The stability of time-varying periodic systems has been discussed in Section 3.2. Section 2.1 in this chapter presents the theory of optimal filtering for periodic systems, adapted from the results of [50] for the more general time-varying case. The following Section 2.2 introduces the essential concepts of the lifting technique, by which periodic systems can be associated to an equivalent discrete time-invariant (but infinite dimensional in the I/O spaces) system. This tool will be used to compute the I/O norm of the periodic system and for an early design of the optimal filter (Section 7.1).

The second challenging factor comes from the fact that we consider the array to consist of an infinite number of cantilevers. Such a structure is evidently an abstraction, since in practice any array will consist of only a

finite number of cantilevers. However, the drawbacks deriving from this assumption are largely compensated by the results that can be obtained from this theoretical approach. Under the assumption that all cantilevers are identical, the multicantilever array can be cast in the class of spatially invariant distributed systems. Section 2.3 introduces some fundamental aspects of this class of systems, and shows how by Fourier transformation in the spatial domain, the study of an infinite dimensional system can be reduced to the analysis of a parameterized family of finite dimensional systems. This approach is convenient, since it enables to extend some of the standard results and techniques from finite dimensional systems theory to this setting in a quite straightforward way.

2.1 Optimal Control for Periodic Systems

One of the main goals of our research is to replace the direct measurement of the cantilever displacement, commonly performed via optical levers [38, 39] or interferometric methods [40, 51], by an indirect measurement based on a state observer. The reason to prefer this approach is twofold. First, it would allow for more compact devices. The methods cited above at the present time require quite cumbersome apparatus, that defeat the efforts of miniaturization of the probe/sensing part of the device. AFM users, for instance, know how disproportionate is the dimension of the sensing cantilever compared to the part of the instrument devoted to detect the cantilever motion. Second, by optimal tuning of the observer parameters it is conceivable that a high fidelity position measurement can be obtained,

thus improving resolution and overcoming the physical limitations of the apparatuses mentioned above. For the vibrometer technique, for instance, it is known that the expected 2nm accuracy in the measurement of displacement cannot be guaranteed when the frequency of vibration exceeds 15kHz [52].

The observer problem for the cantilever displacement is formulated in Section 7.1 as an \mathcal{H}_∞ filtering problem for periodic systems [53]. Whence in this section we present some general results on the theory of \mathcal{H}_∞ filtering for periodic systems. Our source is [50] and in that paper the interested reader will be able to find a more detailed analysis, considering both finite and infinite horizon problems, as well as smoothing, for the general case of time-varying systems. Here we adapt those results to the special class of periodic systems.

We consider the following linear system

$$\begin{aligned} \dot{x} &= A(t)x + B(t)w \\ y &= C(t)x + D(t)w \end{aligned} \tag{2.1}$$

where $x \in \mathbb{R}^n$ is the state, $y \in \mathbb{R}^p$ is the measured output, $w \in \mathbb{R}^m$ is the noise and A, B, C, D are T -periodic matrix functions of time. The filtering problem amounts to finding a causal system that, using the measurement y , provides an estimate \hat{x} of the state x . In particular, in the \mathcal{H}_∞ setting the filter is designed to minimize the performance index

$$J := \sup_{0 \neq w \in \mathcal{L}_2} \frac{\|x - \hat{x}\|_2^2}{\|w\|_2^2},$$

i.e. to minimize the maximum energy of the estimation error over all possible (bounded energy) disturbances.

Some technical assumptions and definitions need to be introduced before presenting the main result. More precisely, we assume in the following that

- $(A(t), B(t))$ is stabilizable,
- $(C(t), A(t))$ is detectable,
- $D(t) \begin{bmatrix} B'(t) \\ D'(t) \end{bmatrix} = \begin{bmatrix} 0 \\ I \end{bmatrix}$.

The definition of stabilizability and detectability for periodic systems are formally identical to the corresponding definitions for time invariant systems.

Definition 2.1 [54] *System (2.1) is stabilizable if there exists a T -periodic matrix $K(t)$ such that the system*

$$\dot{x} = [A(t) - B(t)K(t)]x$$

is asymptotically stable.

A test for stabilizability is given in the following theorem.

Theorem 2.2 [54] *Let $\Phi(t, 0)$ be the state transition matrix of system (2.1), with $\Phi(0, 0) = I$. The system is stabilizable iff for each eigenvalue λ of $\Phi(T, 0)$ such that $|\lambda| \geq 1$, the conditions*

$$\Phi'(T, 0)\eta = \lambda\eta, \quad \eta \in \mathbb{C}^n,$$

$$B'(t)\Phi'(0, t)\eta = 0 \quad \text{for a.e. } t \in [0, T]$$

imply $\eta = 0$.

Note that the conditions given in the previous theorem can be interpreted as the conventional requirement on the controllability of the unstable modes of the system. In fact if $\eta \neq 0$, $y = \Phi'(0, t)\eta$ represents a solution that grows unbounded and is orthogonal to the input range, i.e. it is not controllable. Also in the case of periodic systems the notion of detectability is dual to the notion of stabilizability and therefore can be easily derived from the condition stated above.

The following theorem presents the main result of [50] adapted here to the case of a periodic system.

Theorem 2.3 *There exists a filter such that $J < \gamma^2$ iff there exists a T -periodic symmetric matrix function $P(t)$, that is absolutely continuous and differentiable a.e. in $[0, T]$ and satisfies*

$$\text{i) } \dot{P}(t) = A(t)P(t) + P(t)A(t)' - P(t)[C(t)'C(t) - \frac{1}{\gamma^2}I]P(t) + B(t)B(t)',$$

ii) *The system*

$$\dot{p} = [A(t) - P(t)(C'(t)C(t) - \frac{1}{\gamma^2}I)]p$$

is exponentially stable.

Under these assumptions, the filter is given by

$$\dot{\hat{x}} = A(t)\hat{x} + P(t)C'(t)(y - C(t)\hat{x}) \quad \hat{x}(0) = 0.$$

An implicit assumption of the theorem stated above is the knowledge of the initial condition for the differential equation i) that corresponds to the periodic stabilizing solution. In general such an initial condition is unknown. In order to compute it, we define the mapping $\mathcal{P} : R^{n \times n} \rightarrow R^{n \times n}$,

$$\mathcal{P}(M) = M - P(T), \tag{2.2}$$

where $P(T)$ is the solution, computed at time T , of

$$\dot{P}(t) = A(t)P(t) + P(t)A'(t) - P(t)R(t)P(t) + Q(t), \quad P(0) = M, \quad (2.3)$$

where $R(t) = C(t)'C(t) - \frac{1}{\gamma^2}I$ and $Q(t) = B(t)B'(t)$. If M is a matrix corresponding to any of the steady-state periodic solutions of (2.3), then $\mathcal{P}(M) = 0$. Thus the problem is converted to that of finding the fixed points of this equation. This can be done numerically by using the secant method and defining the iterative scheme :

$$M_{k+1} = M_k - [M_k - M_{k-1}] [\mathcal{P}(M_k) - \mathcal{P}(M_{k-1})]^{-1} \mathcal{P}(M_k).$$

Once the initial condition has been determined, the optimal filter can be found by solving the periodic Riccati differential equation *i*). Note that the filter has the structure of a standard observer.

2.2 The Lifted System

The lifting technique is a very useful theoretical tool for dealing with periodic systems. The advantage of lifting is that it allows us to associate with a T -periodic system G , an equivalent discrete shift-invariant system \hat{G} . Intuitively speaking, this is done by decomposing the input and output signals of G into a sequence of segments, corresponding to the signals over successive intervals of length T , as schematically represented in Figure 2.1. Whence, each signal can be regarded as the discrete collection of these trajectory pieces, i.e. as a discrete signal whose samples are defined over the Banach space $X[0, T]$, where X is the space, usually $\mathcal{L}_\infty[0, \infty]$, where the system signals are defined. It can be shown (see [55] for instance) that this

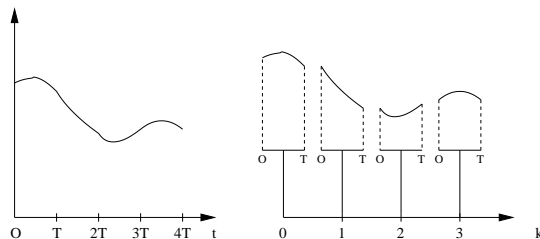


Figure 2.1: Schematic representation of lifting for a continuous time signal.

induces a rearrangement of the original T -periodic system G , such that its lifted equivalent \hat{G} is shift-invariant. In fact, there is a strong correspondence between a system and its lifting, that preserves not only algebraic system properties, such as cascade decomposition and feedback, but also internal stability and induced system norms.

Even though the equivalent lifted system has the very desirable properties of being linear, shift-invariant and norm preserving, it is infinite dimensional, since by construction its input/output spaces are infinite dimensional. Therefore problems we are interested in, like optimal observer design or norm computation, become more difficult to solve.

The approach we have followed, along the lines of [56], is to convert the infinite dimensional problem to an almost equivalent finite dimensional one. Here, by almost equivalent we mean that the problem we finally solve is an approximation of the original one. The idea is to fast-sample the lifted system so that the infinite dimensional input/output spaces are replaced by finite dimensional ones. Figure 2.2 is a schematic representation of the fast sampling concept. It has been proved [56] that the rate of convergence of this approximation is $\frac{1}{n}$, if T is the period of the system and $\frac{T}{n}$ the

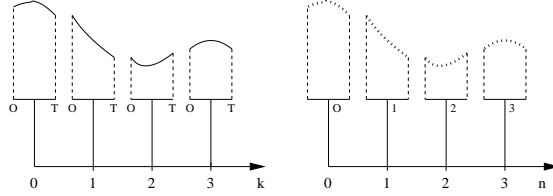


Figure 2.2: Schematic representation of fast sampling for lifted signals.

sampling rate. Hence, by increasing the number of samples per period we can approximate the original system to any prescribed degree of accuracy [56].

In the following, we compute the lifted-sampled state space representation of

$$\begin{aligned}
 \dot{x} &= A(t)x + B_1w \\
 z &= C_1x + D_{12}u \\
 y &= C_2(t)x + D_{21}w
 \end{aligned} \tag{2.4}$$

used in the \mathcal{H}_∞ filtering problem (7.1), introduced in Section 7.1 for the optimal observer problem formulation. Here $A(t)$ and $C_2(t)$ are the state and output matrices of the state space representation of a single cantilever (Section 5.7). The inputs are w , representing system and sensor noise, and u , the output of the optimal \mathcal{H}_∞ filter. In [56], analytical expressions to compute the system matrices corresponding to the approximate problem are provided. Here we extend those results to the case of periodic system matrices. First of all we rearrange the terms in equations (2.4), introducing the fictitious output

$$y_o = [1 \ 0]x = C_o x,$$

so that we can isolate the time-invariant part of the state equation (7.1)

and view its time-varying part as a feedback from the output y_o

$$\begin{aligned}
x' &= A_o x & + B_1 w & & + B_3 v \\
z &= C_1 x & & + D_{12} u \\
y &= C_2(t)x & + D_{21} w & & \\
y_o &= C_o x \\
v &= -K(t)y_o,
\end{aligned} \tag{2.5}$$

where $A_o = \begin{bmatrix} 0 & 1 \\ -a & -c \end{bmatrix}$, $B_3 = \begin{bmatrix} 0 \\ 1 \end{bmatrix}$ and $K(t) = 2q \cos 2t$. Note that a , c and q have been defined in Section 5.1 and are functions of the system physical parameters. The advantage in rewriting the system in this form is that we are able to compute analytically its lifted state space representation. The lifted representation, in fact, requires the computation of the state transition matrix. While for the Mathieu equation this cannot be done analytically, equation (2.5) poses no problems.

If we denote by \underline{s}_k the N dimensional vector containing the N samples of $s(t)$ corresponding to the k -th time period, $[kT, (k+1)T)$

$$\underline{s}_k := \begin{bmatrix} s(kT) \\ s(kT + \frac{T}{N}) \\ s(kT + \frac{2T}{N}) \\ \vdots \\ s((k+1)T - \frac{T}{N}) \end{bmatrix},$$

the state equations of the approximate problem (lifted and sampled) cor-

responding to (2.5) turn out to be

$$\begin{aligned}
x_{k+1} &= \underline{\mathbf{A}}x_k & + \underline{\mathbf{B}}_1 \underline{\mathbf{w}}_k & & + \underline{\mathbf{B}}_3 \underline{\mathbf{v}}_k \\
z_k &= \underline{\mathbf{C}}_1 x_k & + \underline{\mathbf{D}}_{11} \underline{\mathbf{w}}_k + \underline{\mathbf{D}}_{12} \underline{\mathbf{u}}_k & + \underline{\mathbf{D}}_{13} \underline{\mathbf{v}}_k \\
y_k &= \underline{\mathbf{C}}_2 x_k & + \underline{\mathbf{D}}_{21} \underline{\mathbf{w}}_k & & + \underline{\mathbf{D}}_{23} \underline{\mathbf{v}}_k \\
y_{ok} &= \underline{\mathbf{C}}_o x_k & + \underline{\mathbf{D}}_{o1} \underline{\mathbf{w}}_k & & + \underline{\mathbf{D}}_{o2} \underline{\mathbf{v}}_k \\
v_k &= -\underline{\mathbf{K}} y_{ok},
\end{aligned} \tag{2.6}$$

where the presence of the new D_{ij} matrices is a result of the lifting. The analytical expression of all the matrices in (2.6) can be computed as shown in [56], with the exception of the matrices coming from the time-varying part of the system (last three equations in 2.6), which are

$$\begin{aligned}
\underline{\mathbf{C}}_2 &= \left[C_0 \quad e^{A_o T_s} C_{\frac{1}{N}}^T \quad e^{2A_o T_s} C_{\frac{2}{N}}^T \quad \dots \quad e^{A_o T_s (N-1)} C_{1-\frac{1}{N}}^T \right]^T \\
\underline{\mathbf{D}}_{21} &= \begin{bmatrix} D_{21} & 0 & 0 & \dots & 0 \\ C_{\frac{1}{N}} \tilde{B}_1 & D_{21} & 0 & \dots & 0 \\ C_{\frac{2}{N}} e^{A_o T_s} \tilde{B}_1 & C_{\frac{2}{N}} \tilde{B}_1 & D_{21} & \ddots & 0 \\ \vdots & & \ddots & \ddots & \vdots \\ C_{1-\frac{1}{N}} e^{A_o T_s (N-2)} \tilde{B}_1 & \dots & & C_{1-\frac{1}{N}} \tilde{B}_1 & D_{21} \end{bmatrix} \\
\underline{\mathbf{D}}_{23} &= \begin{bmatrix} 0 & 0 & 0 & \dots & 0 \\ C_{\frac{1}{N}} \tilde{B}_3 & 0 & 0 & \dots & 0 \\ C_{\frac{2}{N}} e^{A_o T_s} \tilde{B}_3 & C_{\frac{2}{N}} \tilde{B}_3 & 0 & \ddots & 0 \\ \vdots & & \ddots & \ddots & \vdots \\ C_{1-\frac{1}{N}} e^{A_o T_s (N-2)} \tilde{B}_3 & \dots & & C_{1-\frac{1}{N}} \tilde{B}_3 & 0 \end{bmatrix}
\end{aligned}$$

and

$$\underline{\mathbf{K}} = \begin{bmatrix} 2q & 0 & \dots & 0 \\ 0 & 2q \cos(\frac{T}{N}) & 0 & \dots & 0 \\ 0 & 0 & 2q \cos(\frac{2T}{N}) & & 0 \\ \vdots & & \dots & \ddots & \\ 0 & & \dots & & 2q \cos(\frac{N-1}{N}T) \end{bmatrix},$$

with

$$e^{A_o T_s} = \begin{bmatrix} \cos \sqrt{a} T_s & \frac{1}{\sqrt{a}} \sin \sqrt{a} T_s \\ -\sqrt{a} \sin \sqrt{a} T_s & \cos \sqrt{a} T_s \end{bmatrix},$$

$C_k = C_2(kT)$ and \tilde{B}_j is the sampled matrix corresponding to B_j in (2.5). Finally, by defining the following matrices

$$\begin{aligned} F &= \underline{\mathbf{A}} - \underline{\mathbf{B}}_3 \underline{\mathbf{K}}(I + \underline{\mathbf{D}}_{o2} \underline{\mathbf{K}})^{-1} \underline{\mathbf{C}}_o, \\ G_1 &= \underline{\mathbf{B}}_1 - \underline{\mathbf{B}}_3 \underline{\mathbf{K}}(I + \underline{\mathbf{D}}_{o2} \underline{\mathbf{K}})^{-1} \underline{\mathbf{D}}_{o1}, \\ H_1 &= \underline{\mathbf{C}}_1 - \underline{\mathbf{D}}_{13} \underline{\mathbf{K}}(I + \underline{\mathbf{D}}_{o2} \underline{\mathbf{K}})^{-1} \underline{\mathbf{C}}_o, \\ H_2 &= \underline{\mathbf{C}}_2 - \underline{\mathbf{D}}_{23} \underline{\mathbf{K}}(I + \underline{\mathbf{D}}_{o2} \underline{\mathbf{K}})^{-1} \underline{\mathbf{C}}_o, \\ J_{11} &= \underline{\mathbf{D}}_{11} - \underline{\mathbf{D}}_{13} \underline{\mathbf{K}}(I + \underline{\mathbf{D}}_{o2} \underline{\mathbf{K}})^{-1} \underline{\mathbf{D}}_{o1}, \\ J_{21} &= \underline{\mathbf{D}}_{21} - \underline{\mathbf{D}}_{23} \underline{\mathbf{K}}(I + \underline{\mathbf{D}}_{o2} \underline{\mathbf{K}})^{-1} \underline{\mathbf{D}}_{o1}, \end{aligned}$$

and $J_{12} = \underline{\mathbf{D}}_{12}$, the generalized plant associated to the approximate problem is given by

$$G_{approx} := \left[\begin{array}{c|cc} \underline{\mathbf{F}} & \underline{\mathbf{G}}_1 & 0 \\ \hline \underline{\mathbf{H}}_1 & \underline{\mathbf{J}}_{11} & \underline{\mathbf{J}}_{12} \\ \underline{\mathbf{H}}_2 & \underline{\mathbf{J}}_{21} & 0 \end{array} \right], \quad (2.7)$$

which describes a finite dimensional discrete shift-invariant system. From this point on, the analysis can be carried out in a straightforward way, relying on known results from classical system theory.

2.3 Linear Spatially Invariant Distributed Systems

The recent technological advances in the field of micro devices have made feasible the implementation of new control structures, consisting of large arrays of spatially distributed controllers and sensors [29, 11]. In turn, these architectures have awakened an increasing interest in the theory of spatially distributed systems, which represent the appropriate mathematical tool for their modelling and study.

Spatially invariant systems are an important subclass in the family of spatially distributed systems. Systems belonging to this class are composed of identical units, with independent actuation and sensing capabilities, distributed on a regular lattice. Their variables x can be modelled as functions of both time and space, $x = x(t, k)$, with the time variable causal and the spatial variable completely a-causal. Examples are offered by strings of vehicles or platoons [57, 58, 59], arrays of sensors and actuators in flow control problems [60, 61, 62, 63], arrays of microcantilevers in scanning probe devices [29, 44, 53]. Figure 2.3 is a schematic representation of a distributed spatially invariant system.

Roughly speaking, spatial invariance means that the dynamics of the system are independent from the “point of observation”: shifting the spatial variable by a fixed amount does not affect the dynamics of the system. It should be noted that this property implies the assumption that the elements are fully distributed over the spatial coordinate, i.e. are infinite in number as depicted in Fig.2.3. This fact implies that the overall struc-

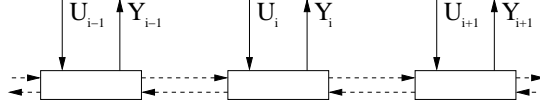


Figure 2.3: Schematic of a spatial invariant structure. The dashed lines represent some form of internal coupling (not necessarily nearest neighbor). All the units are identical and can be independently sensed and actuated.

ture is described by an infinite dimensional system. Such a structure is evidently an abstraction from a real case, however the drawbacks deriving from this assumption are largely compensated by the results that can be obtained from this theoretical approach.

In terms of a state space representation, spatial invariance implies that the matrix operators $\mathcal{A}, \mathcal{B}, \mathcal{C}, \mathcal{D}$ in

$$\begin{aligned} \frac{d}{dt}x(t, \cdot) &= \mathcal{A}x(t, \cdot) + \mathcal{B}u(t, \cdot) \\ y(t, \cdot) &= \mathcal{C}x(t, \cdot) + \mathcal{D}u(t, \cdot), \end{aligned} \quad (2.8)$$

are Toeplitz and translation invariant. We refer to [64, 65] for a rigorous mathematical treatment of this topic.

Indeed, the property of spatial invariance turns out to play a very important role in the analysis of these systems. As a matter of fact, it makes it possible to apply a Fourier transformation in the spatial coordinate. The Fourier transform of a two dimensional real-valued function $s(t, k)$ is a complex-valued function defined as

$$S(t, \theta) = \sum_{k=-\infty}^{\infty} s(t, k)e^{-ik\theta} \quad ,$$

with $\theta \in [0, 2\pi]$. Similarly to its one dimensional counterpart, it transforms translation invariant operators into multiplication operators. Hence, equation (2.8) becomes

$$\begin{aligned}\dot{\hat{x}}(t, \theta) &= \hat{\mathcal{A}}(\theta)\hat{x}(t, \theta) + \hat{\mathcal{B}}(\theta)\hat{u}(t, \theta) \\ \hat{y}(t, \theta) &= \hat{\mathcal{C}}(\theta)\hat{x}(t, \theta) + \hat{\mathcal{D}}(\theta)\hat{u}(t, \theta),\end{aligned}\tag{2.9}$$

where the symbol $\hat{\cdot}$ denotes the Fourier transform in space.

Notice that equation (2.9) describes a standard finite dimensional model, the only difference being the presence of the parameter $\theta \in [0, 2\pi]$. Hence, by means of the Fourier transform we have associated the *infinite dimensional distributed* system with a *finite dimensional parametric* model. This fact has the important consequence of allowing the almost straightforward extension of many of the results valid for classical finite dimensional systems to spatially invariant distributed systems [65, 64]. As a matter of fact, “global” structural properties (stability, controllability, observability, etc.), where by global we mean relative to the entire infinite dimensional structure, can be studied for each system of the family using the well-known methods for finite dimensional systems, and then verified at each value of the parameter $\theta \in [0, 2\pi]$.

*

Chapter 3

Parametric resonators

In this chapter, we introduce the concepts of parametric oscillator and parametric resonance. In particular, Section 3.2 is devoted to discussing some relevant properties of the Mathieu equation that in Section 3.3 are extended to the case of coupled Mathieu equations. In fact, it will be proven in Chapter 5 that the dynamics of electrostatically actuated micro-cantilevers are described by either a single or coupled Mathieu equations. There are several applications that arise from the exploitation of parametric amplification, from extremely sensitive mass sensors [66, 67] to mechanical filters [1, 65, 68]. We do not explore this direction in this dissertation, but consider the ability to induce parametric resonance and to map the first region of instability (Chapter 6) as a further tangible sign of the validity of our model.

3.1 Micro-Oscillators

A simple model of a mechanical oscillator is that of a mass-spring-damper system. Using a lumped parameters representation, this oscillator can be described by a second order linear differential equation,

$$\ddot{x} + c\dot{x} + ax = f(t), \quad (3.1)$$

where the coefficients have been scaled by the mass and $f(t)$ represents a forcing input. The values of c and a depend on the physical properties of the oscillator and determine the characteristics of its response to external excitations. For instance, the damping of the response depends on c and when this coefficient is small, the frequency of free oscillation is equal to $\omega = \sqrt{a}$. Therefore, any change in the value of these parameters is reflected in the change of some observable (i.e. measurable) characteristic property of the response of the oscillator. What makes micro-oscillators particularly interesting, is the fact that their size makes them sensitive to extremely small changes of their parameters. Whence, they are able to detect very small variations of any physical quantity causing the change. For instance, in biosensors, the absorption of molecules on the surface of a cantilever causes an increase in the mass and surface stress. These induce bending in the cantilever and a shift in its resonant frequency, whose value can be measured experimentally and related to the physical/chemical properties of the adsorbate. This sensitivity has been exploited in a wide variety of applications [20, 69, 70] and has resulted in micro-scales that can measure masses down to the attograms [71, 72, 73], calorimeters with femtojoules resolution [18, 74, 75, 76] and force detectors that sense forces

in the nanonewtons [18, 77].

For small excitations, a system such as (3.1) will produce a large response only if the frequency of excitation is close to a natural frequency. Oscillators that exhibit this property are called *harmonic*, to differentiate them from the class of so-called *parametric* oscillators. The latter are typified by the Hill equation

$$\ddot{x} + c\dot{x} + (a + f(t))x = 0,$$

where c and a are constant coefficients as in (3.1), and $f(t)$ is typically a periodic function of time [78, 79]. It should be noted that in this equation the input appears as a time varying modification of a system parameter, while in the harmonic case (3.1) the external excitation enters the equation of motion as an inhomogenous term. This fact leads to significant differences in the response behavior of the two classes of oscillators. In particular, parametric systems respond strongly when the frequency of excitation is related to the natural frequency by a resonance condition, without necessarily being equal to it. Hence, large responses may be generated even when the excitation frequency is remote from the system's natural frequency, but related to it through an integer, or fractional, multiple. The resulting motion is unstable and grows exponentially with time. Its magnitude is not affected by damping, and is governed only by the nonlinear effects that come into play as a result of the large displacements. Damping is responsible only for creating a minimum threshold in the excitation amplitude, below which parametric amplification cannot be induced. This reason makes parametric resonance difficult to observe at the macroscale. On the contrary, micro-oscillators which are quite often operated in vac-

uum, can be driven into parametric mode with relative ease.

The interest in devices that exhibit parametric behavior comes from the fact that it represents a mechanism of mechanical amplification that can improve the sensitivity of micro-resonators in all of the applications mentioned above. In fact, as the size of the components gets smaller, so does the magnitude of their displacement, with the result being that the transduction mechanism has to operate close to the background noise. Hence, the large amplification generated by parametric resonance can dramatically increase their sensitivity [66].

The Mathieu equation belongs to the class of parametric systems. Given its relevance in the modelling of a electrostatically actuated microcantilevers, we devote the next two sections to analyze its properties in some more detail.

3.2 The Mathieu Equation

Our interest in the Mathieu equation stems from the fact that it models the dynamical behavior of an electrostatically actuated cantilever, as shown in Section 5.1. We present here only the main results regarding its characterization, when necessary to understand the material presented in the rest of the dissertation. We refer the interested reader to the abundant literature on the topic for a more thorough analysis [78, 79, 80, 81, 82, 83].

The Mathieu equation takes the form

$$\ddot{z} + (a - 2q \cos 2t)z = 0, \quad (3.2)$$

and is a second order linear differential equation with periodic coefficients.

It was first introduced by Mathieu in 1868 [84] to model the vibrational modes of a stretched membrane having an elliptical boundary. Since then, a considerable amount of research effort has been devoted to studying its peculiar stability properties in terms of its parameters a and q [80, 81, 83, 85].

By defining the vector $x = [z \ z]^T$, equation (3.2) can be rewritten in state space form as follows

$$\dot{x} = \begin{bmatrix} 0 & 1 \\ -a + 2q \cos 2t & 0 \end{bmatrix} x = A(t)x, \quad (3.3)$$

which defines a linear, T -periodic system, $A(t) = A(t + T)$ (here $T = \pi$). From standard results on the solutions of systems of differential equations, it is known that the real solutions of equation (3.3) form a 2-dimensional linear subspace of $C^1(\mathbb{R}^2)$. Let x_1 and x_2 be any two independent solutions of equation (3.3). The *fundamental* matrix of the system is defined as

$$\Phi(t) := [x_1 \ x_2] \in C^1(\mathbb{R}^{2 \times 2}),$$

and owes its name to the fact that any other solution can be written uniquely as a linear combination of its columns

$$x(t) = \Phi(t)v, \quad (3.4)$$

with $v \in \mathbb{R}^2$.

It is not difficult to show that if $x(t)$ is a solution of a T -periodic linear system, so is $x(t + T)$. Hence, by definition of $\Phi(t)$ and equation (3.4) we can write

$$\Phi(t + T) = \Phi(t)C, \quad (3.5)$$

with $C \in \mathbb{R}^{2 \times 2}$. By setting $t = 0$ in equation (3.5) we can derive the following equation, which defines the so-called *principal matrix* C of the system

$$C = \Phi(0)^{-1}\Phi(T). \quad (3.6)$$

The reason to introduce C is that it defines the *characteristic multipliers*, which are tightly related to the stability properties of a periodic system. A scalar $\lambda \in \mathbb{C}$ is said to be a characteristic multiplier if there exists a nontrivial solution $x(t)$ of equation (3.3), such that

$$x(t + T) = \lambda x(t). \quad (3.7)$$

It is evident now that the stability of the system depends on λ . In fact, from equation (3.7) it follows that $x(t + nT) = \lambda^n x(t)$, $n \in \mathbb{N}$. Hence, the system will be asymptotically stable if all the λ 's are inside the unit disk, neutrally stable if they are on the unit circle and unstable if at least one lies outside the unit disk.

It can be proved that the characteristic multipliers coincide with the eigenvalues of C . As a matter of fact, from equations (3.4) and (3.5),

$$\begin{aligned} x(t) = \Phi(t)v &\implies x(t + T) = \Phi(t + T)v \\ &= \Phi(t)Cv \end{aligned},$$

so that, if v is an eigenvector of C ,

$$x(t + T) = \lambda \Phi(t)v = \lambda x(t).$$

Note that, even though C depends on the particular Φ considered, its eigenvalues are invariant, that is all matrices defined by equation (3.6)

are similar. Hence the definition of the characteristic multipliers is unambiguous. Moreover, without loss of generality, we can restrict ourselves to considering the particular C corresponding to $\Phi(0) = I$, i.e. $C = \Phi(T)$. In terms of stability, C plays for periodic systems the same role that the state matrix A plays for time-invariant systems. The characteristic equation of C

$$\det(\lambda I - \Phi(T)) = 0,$$

can be written more explicitly as

$$\lambda^2 - (\text{trace}\Phi(T))\lambda + \det\Phi(T) = 0, \quad (3.8)$$

so that by means of Liouville's formula and equation (3.3)

$$\det\Phi(T) = e^{\int_0^T \text{trace}A(\sigma)d\sigma} = 1,$$

the characteristic equation of C for the Mathieu equation can finally be rewritten as

$$\lambda^2 + b\lambda + 1 = 0, \quad (3.9)$$

with $b = \text{trace}\Phi(T)$. This last equation implies that the product of the two characteristic multipliers of a Mathieu equation is always equal to one, $\lambda_1\lambda_2 = 1$, and so that the system cannot be asymptotically stable. More precisely, from equation (3.9) we can infer that the solutions are (simply) stable if $|\text{trace}\Phi(T)| < 2$ and unstable if $|\text{trace}\Phi(T)| > 2$. The condition $|\text{trace}\Phi(T)| = 2$ defines the transition between stable and unstable behavior. When this condition is satisfied the system has a stable periodic solution, of period $T = \pi$ for $\text{trace}\Phi(T) = 2$ and $T = 2\pi$ for $\text{trace}\Phi(T) = -2$.

Unfortunately, if we insist on an exact analysis of the stability problem, this is all the information we can obtain. As a matter of fact, the computation of the characteristic multipliers relies on the computation of the state transition matrix over one period, which for the Mathieu equation cannot be done analytically. The same argument holds also for the Floquet transformation [81, 83, 86], where an appropriate change of coordinates (defined assuming the knowledge of $\Phi(t)$) allows to obtain an equivalent time-invariant system, whose stability properties could in principle be easily analyzed. Indeed, one has to resort to approximation methods, like numerical computation of $\Phi(T)$, averaging or perturbation methods.

3.2.1 Perturbation Analysis for the Mathieu Equation

The general procedure of perturbation theory is to identify a small parameter, usually denoted by ϵ , such that when ϵ is zero the problem becomes solvable. In the case of equation (3.2), the small parameter is q . By letting $\epsilon = -2q$, we obtain the equation

$$\ddot{z} + az + \epsilon \cos 2tz = 0. \quad (3.10)$$

For $\epsilon = 0$ equation (3.10) describes a simple harmonic oscillator whose solution, z_o , can be easily computed. For $\epsilon \neq 0$ the solution of (3.10) can be written in the form of a series expansion in ϵ

$$z = z_o + \epsilon z_1 + \epsilon^2 z_2 + \dots, \quad (3.11)$$

so that the original problem is decomposed into an infinite sequence of relatively easy ones: computing the coefficients of the series.

A detailed derivation, using this method, of the stable/unstable regions as a function of the parameters a and q can be found for instance in [80]. Figure 3.1 portrays these characteristic tongue-like shaped regions: parameter pairs (a, q) belonging to the shaded areas correspond to unstable behavior; for parameter pairs belonging to the white areas all solutions are bounded; if (a, q) belongs to a boundary curve, the equation has one periodic solution (of period π or 2π).

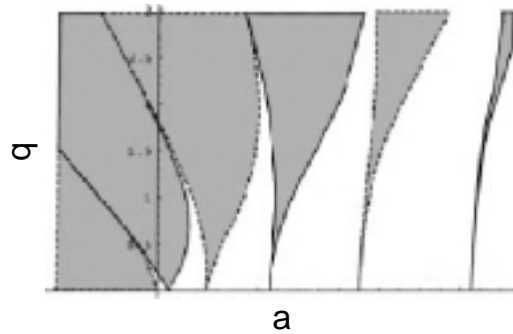


Figure 3.1: Mathieu equation: the shaded areas correspond to unstable behavior.

In the rest of this section, we derive the equations for the boundary curves of the first unstable region. The result will be used in Chapter 6 to compare the theoretical prediction with experimental results. Following [83], the perturbation method we use is the so-called two variable expansion, which is equivalent to standard averaging. This method exploits the fact that, for many vibration problems, the expected solution involves two time scales: the time scale of the periodic motion itself and a slower time scale, which represents the approach to the periodic motion. The method

proposes to distinguish between these two time scales, by associating a separate independent variable with each one. Let $\xi = t$ and $\eta = \epsilon t$ be the fast and slow varying time coordinates respectively, and write $x(t) = x(\xi, \eta)$. Equation (3.10) is modified accordingly as

$$\frac{\partial^2 z}{\partial \xi^2} + 2\epsilon \frac{\partial^2 z}{\partial \xi \partial \eta} + \epsilon^2 \frac{\partial^2 z}{\partial \eta^2} + (a + \epsilon \cos 2\xi)z = 0.$$

Expanding z in power series as in (3.11), substituting in the previous equation and collecting terms of equal power in ϵ , we obtain

$$\frac{\partial^2 z_o}{\partial \xi^2} + z_o = 0 \quad (3.12)$$

$$\frac{\partial^2 z_1}{\partial \xi^2} + z_1 = -2 \frac{\partial^2 z_o}{\partial \xi \partial \eta} - (a_1 + \cos 2\xi)z_o \quad (3.13)$$

where we have introduced also a power expansion of $a = 1 + a_1\epsilon + a_2\epsilon^2 + \dots$ and considered only the terms of first order. Taking the general solution to equation (3.12) to be of the form

$$z_o(\xi, \eta) = A(\eta) \cos \xi + B(\eta) \sin \xi,$$

and substituting in equation (3.13), we get after few algebraic manipulations

$$\begin{aligned} \frac{\partial^2 z_1}{\partial \xi^2} + z_1 = & 2 \frac{dA}{d\eta} \sin \xi - 2 \frac{dB}{d\eta} \cos \xi \\ & - a_1 (A \cos \xi + B \sin \xi) \\ & - \frac{A}{2} (\cos 3\xi + \cos \xi) \\ & - \frac{B}{2} (\sin 3\xi - \sin \xi). \end{aligned}$$

Removal of resonance terms gives the following slow-flow equations

$$\begin{aligned} \frac{dA}{d\eta} &= \frac{1}{2}(a_1 - \frac{1}{2})B \\ \frac{dB}{d\eta} &= -\frac{1}{2}(a_1 + \frac{1}{2})A. \end{aligned} \quad (3.14)$$

Equilibrium points of the slow flow correspond to periodic motions of the Mathieu equation : by studying the stability of these linear equations (3.14) we can conclude that the Mathieu equation is stable if $|a_1| > \frac{1}{2}$. Hence in the a - q parameter space the following two curves represent the transition from stable to unstable regions

$$a = 1 \pm \frac{\epsilon}{2} = 1 \pm q, \quad (3.15)$$

Inside that tongue, solutions to (3.10) grow exponentially in time, while outside the tongue they are quasiperiodic functions of time.

By considering higher order expansions, it is possible to determine the other regions of instability, depicted in Figure (3.1). In particular, it can be proved that for $\epsilon = 0$ instabilities occur at

$$a = n^2, \quad n \in \mathbb{N}. \quad (3.16)$$

The expressions for the boundary curves are quite complicated and are not reported here.

Instead, it is interesting to consider the case of (3.10) with a cubic nonlinearity

$$\ddot{z} + az + \epsilon \cos 2tz + \epsilon a_3 z^3 = 0. \quad (3.17)$$

Following the procedure outlined above, the slow-flow equations (3.15) become [66, 83, 87]

$$\begin{aligned} A' &= \frac{1}{2}(a_1 - \frac{1}{2})B + \frac{3a_3}{8}B(A^2 + B^2), \\ B' &= -\frac{1}{2}(a_1 + \frac{1}{2})A - \frac{3a_3}{8}A(A^2 + B^2), \end{aligned} \quad (3.18)$$

which can be solved numerically to obtain the first region of parametric resonance. The effect of the nonlinearity is to bound the amplitude of the

oscillations. More precisely, going from a non-parametric to a parametric region, the signal still grows exponentially (Fig. 3.2), but its amplitude remains bounded and varies with the value of the perturbation parameter a_1 (Fig. 3.3).

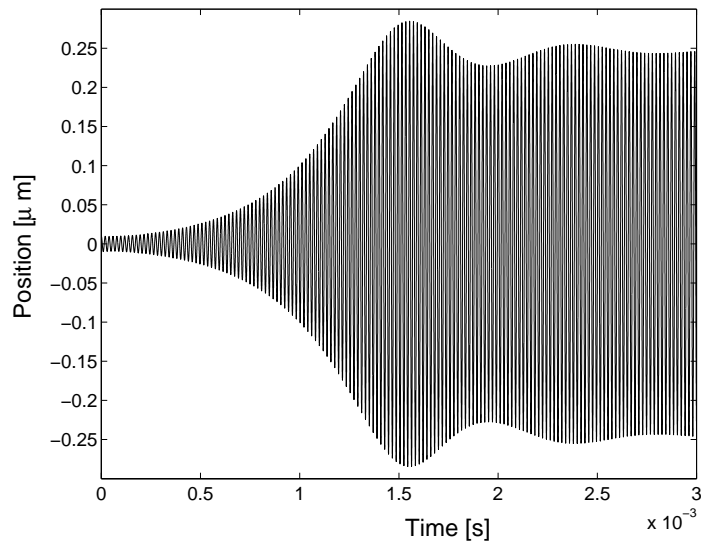


Figure 3.2: Exponential growth of the signal at the transition from non-parametric to parametric region of oscillation. The simulation used the cantilever parameters.

Note that in the simulations of Fig. 3.2 and 3.3 we have used (3.17) with the experimentally identified parameters of our cantilevers. In fact, we will show in Section 5.1 that the dynamics of single electrostatically actuated cantilevers are governed by a Mathieu equation. Note that, in terms of the cantilevers' physical parameters, the first parametric region is centered around $a = 2\omega_r$, with ω_r natural resonant frequency of the cantilever (see Section 6.2). Similar results will be reproduced experimentally in Section

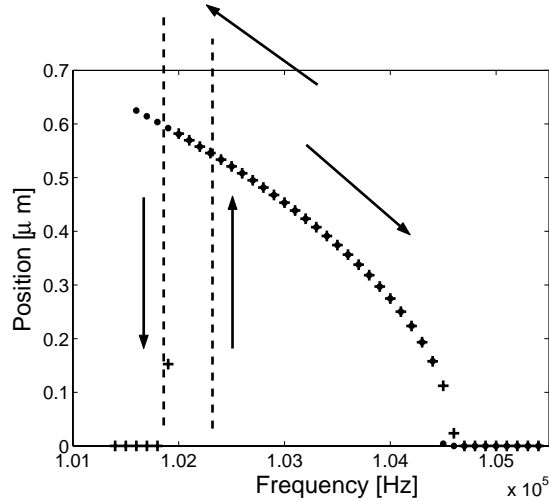


Figure 3.3: Variation of oscillation amplitude with a_1 (i.e. driving frequency for a cantilever) across the first region of parametric amplification. The ‘+’ symbols correspond to increasing values of a_1 (frequency is swept up), the ‘o’ to decreasing values (frequency being swept down). The simulation used the cantilever parameters.

6.2 (Fig. 6.12 and 6.13). From Fig. 3.3 it is evident that (3.17) has a bistable region on the left side of the first parametric region, a result confirmed by Fig. 3.4, which represents a simulation of the phase portrait of (3.18).

3.3 Coupled Mathieu Equations

In this section, we extend the analysis of parametric amplification to the case of coupled Mathieu equations. In fact, in Chapter 5 we show that, as a consequence of the mechanical and electrostatic coupling, multicantilever

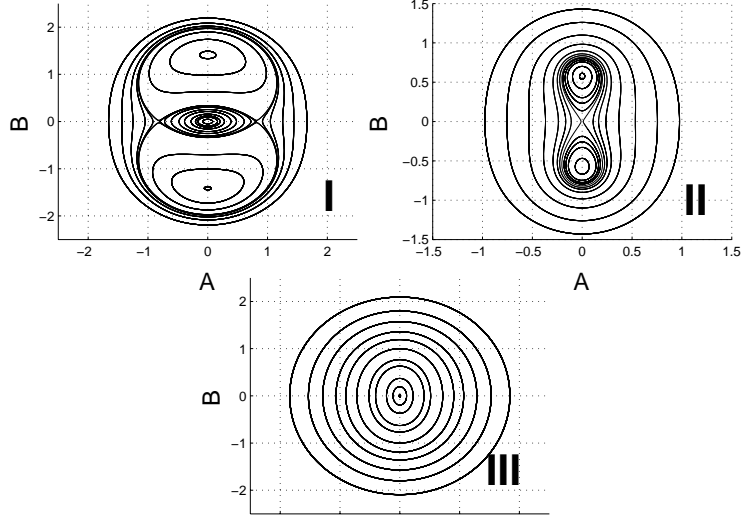


Figure 3.4: Phase portrait of equation (3.18) for different values of perturbation parameter a_1 .

arrays are modelled by equations of this kind.

We consider, at first, the case of two coupled Mathieu equations:

$$\begin{aligned} \ddot{z}_1 + (a_1 - 2q_1 \cos 2t)z_1 + (b_1 - 2b_2 \cos 2t)z_2 &= 0, \\ \ddot{z}_2 + (a_2 - 2q_2 \cos 2t)z_2 + (b_1 - 2b_2 \cos 2t)z_1 &= 0, \end{aligned} \quad (3.19)$$

where we allow the coefficient of coupling to be time-varying. By defining the vector $Z = [z_1, z_2]^T \in \mathbb{R}^2$, (3.19) can be rewritten as

$$\ddot{Z} + [A - \epsilon Q \cos(2t)]Z = 0, \quad (3.20)$$

whose structure is that of a standard Mathieu equation (3.2), except that now A and Q are matrices,

$$A = \begin{bmatrix} a_1 & b_1 \\ b_1 & a_2 \end{bmatrix} \quad \epsilon Q = \begin{bmatrix} 2q_1 & 2b_2 \\ 2b_2 & 2q_2 \end{bmatrix}.$$

Equation (3.20) describes a periodic system and, as stated in the previous section, the stability of its solutions depends on the eigenvalues of the principal matrix, $\Phi(T)$. More precisely, the stability of these trajectories is equivalent to the stability of the equilibrium points of the discrete time-invariant system having $\Phi(T)$ as its state matrix. We want to prove that for $\epsilon = 0$ in (3.20), the origin is a strongly stable [for Definition see [82] pg.117] equilibrium point of $\Phi(T)$. Then, by definition, the “perturbed” solution obtained for small values of ϵ is stable as well.

For $\epsilon = 0$, (3.20) is time-invariant and describes a two-dimensional harmonic oscillator

$$\ddot{Z} + AZ = 0. \quad (3.21)$$

The eigenvalues μ_j of the corresponding $\Phi(T)$ are given by

$$\mu_j = e^{\lambda_j T}, \quad j = 1, \dots, 4 \quad (3.22)$$

where the λ_j 's correspond to the eigenvalues of a state space representation of (3.21) and are purely imaginary pairs since there is no damping. As a consequence, the μ_j 's are on the unit circle. Using Liouville's theorem we can prove that the product of the μ_j 's, for any value of ϵ , is always equal to 1. Together, these two facts imply that the origin is strongly stable. As a matter of fact, these conditions constrain the eigenvalues of the perturbed state transition matrix to move in complex conjugate pairs along the unit circle, and therefore describe stable dynamics. The only cases when the perturbed system can have unstable eigenvalues, is when at least one pair of μ 's overlaps and is equal to ± 1 , or when the two pairs of μ 's overlap, as represented schematically in Fig. 3.5. In fact, in these cases the μ 's can leave the unit circle, still satisfying the condition on their product.

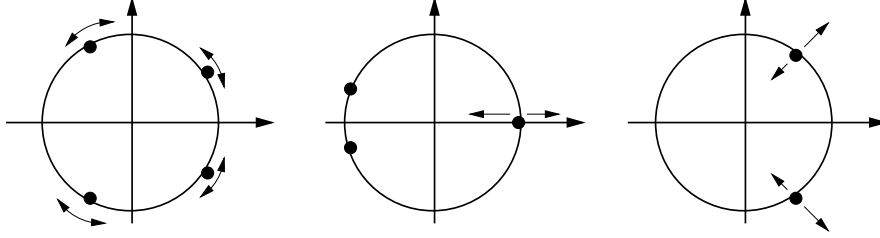


Figure 3.5: Schematic representation of the conditions corresponding to a possible loss in stability for two coupled Mathieu equations.

This loss of stability corresponds to the cases $|\lambda_j|T = \pi n$, and $(|\lambda_i| \pm |\lambda_j|)T = 2\pi n$, $n \in \mathbb{N}$. It is not difficult to prove that

$$|\lambda_j| = \sqrt{\eta_i} \quad i = 1, 2$$

where the η 's are the eigenvalues of A . Hence, in terms of these eigenvalues the unstable tongues are located at

$$\eta_i = n^2, \quad \eta_1^2 \pm \eta_2^2 = 4n^2 \quad n \in \mathbb{N}, i = 1, 2 \quad (3.23)$$

which is the equivalent of (3.16) for two coupled Mathieu equations. Note that, in the coupled case, the eigenvalues of A play the same role as the constant a in a standard Mathieu equation. Moreover, (3.23) implies that, for two coupled Mathieu equations, each region of parametric amplification is composed of more than one tongue. In Section 6.3.2 we will show that experimentally we found the first parametric region to be composed of three subtongues.

To conclude this section, we analyze the case of an infinite number of coupled Mathieu equations. While in any practical system the number of

cantilevers and therefore the number of coupled equations will necessarily be finite, in the limit for a large number of cantilevers, spatially invariant distributed models represent the correct abstraction. Moreover, in case of a large number of units, the drawbacks deriving from this assumption are compensated by the results that can be obtained from this theoretical approach.

In case of an infinite number of coupled Mathieu equations, (3.19) becomes

$$\ddot{z}_i + (a - 2q \cos 2t)z_i + \sum_{j \neq i} (b_{1,j} - 2b_{2,j} \cos 2t)z_j = 0, \quad i, j \in \mathbb{Z}$$

which, by Fourier transformation in the spatial coordinate (Section 2.3), can be written as

$$\hat{\ddot{z}} + [\hat{a}(\theta) - 2\hat{q}(\theta) \cos 2t]\hat{z} = 0, \quad (3.24)$$

with $\hat{a}(\theta) = a + \sum_{m \neq n} b_{1,j} e^{-i\theta m}$ and $\hat{q}(t, \theta) = q + \sum_{m \neq n} b_{2,j} e^{-i\theta m}$. The symbol $\hat{\cdot}$ here denotes Fourier transformation in space.

Equation (3.24) is a parameterized family of Mathieu equations. As discussed in Section 2.3, its stability can be studied for each equation of the family and then verified for each value of $\theta \in [0, 2\pi]$ [64, 88]. More precisely, each θ in (3.24) defines a standard Mathieu equation and therefore determines a set of unstable tongues. As a consequence, (3.24) is also characterized by regions of instability, which are given by the union of these tongues. If we consider, for instance, the case of nearest neighbor interaction ($b_{1,j} = b_{2,j} = 0, \quad \forall j \geq 2$), the unstable regions of (3.24) for $q = b_{21} = 0$ are given by

$$a(\theta) = a + 2b_{12} \cos \theta = n^2, \quad \theta \in [0, 2\pi] \quad (3.25)$$

that is they are intervals, as opposed to points for the single Mathieu equation (3.16).

Figure 3.6 represents the first region of parametric resonance for the case of two, ten and one hundred coupled equations. It should be contrasted with the first tongue in Fig. 3.1 that represents the same region for a single Mathieu equation. Also in this case, shaded areas denote unstable behavior. The simulation considered identical coupled equations, with nearest neighbor interaction and with $a = \frac{b_{1,2}}{2} = 100$. The boundaries were approximated using (3.15).

Note that, as the number of cantilevers increases, the part of the a -axis that belongs to the unstable region increases as well, as predicted by (3.25). This simple example illustrates the point that for large number of units, or cantilevers in our case, the theory of distributed systems is indeed the correct abstraction and that tangible guidelines for the analysis and the control design of such structures can be obtained using the methods of distributed systems theory.

*

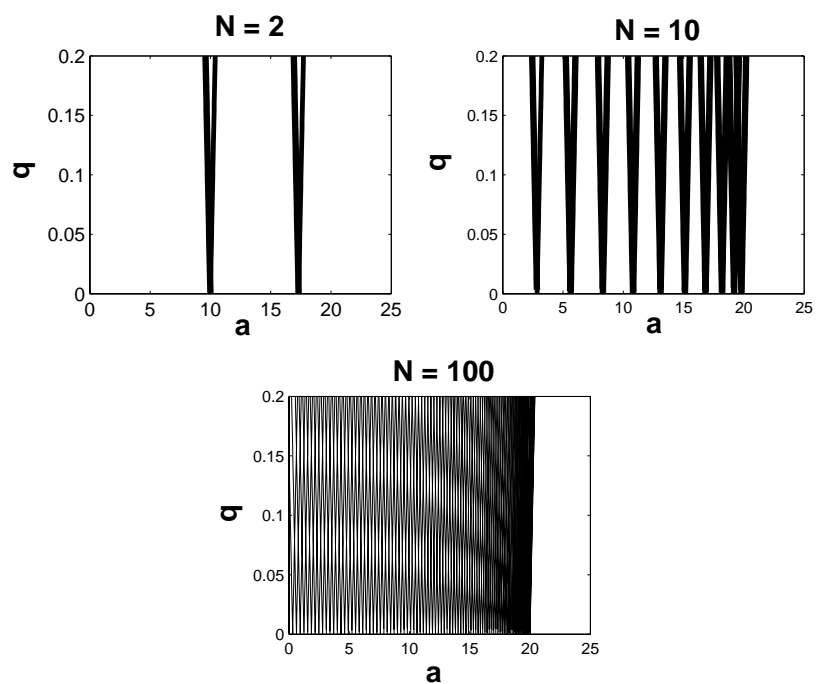


Figure 3.6: First region of parametric amplification for coupled Mathieu equations. The shaded areas correspond to unstable behavior. N denotes the number of coupled equations considered.

Chapter 4

Device Design and Fabrication

It was considered more cost effective to outsource the fabrication of the device, that was in fact commissioned to Cronos (div. of JDS Uniphase from 2000-2002), a commercial MEMS manufacturer. The company has developed and standardized three fabrication processes, referred to as MUMPs® (Multi-User MEMS Processes). Customers whose devices can be fabricated within the fixed sequence of steps involved by each process can submit orders to have the company carry out the fabrication. Our cantilever arrays were fabricated with PolyMUMPs, a three-layer polysilicon surface micro-machining process that is briefly illustrated in Section 4.1.

The process is repeated in successive runs, according to a calendar decided by the company. We reserved two die locations during run 47, that took place around March 2002. Some relevant data about this run, as measured by the company at the completion of the process, is reported at the end of Section 4.1. As with any other customer, we had to submit the design of the layout of the eight masks utilized in the fabrication process.

Section 4.2 discusses some of the design choices that were made.

A detailed information about calendar, process and design rules can be found at the URL [http : //www.memscap.com/memrus](http://www.memscap.com/memrus). Note that the company has been acquired by MEMSCAP as of November 1, 2002.

4.1 Fabrication : PolyMUMPS Process

The PolyMUMPs process derives from work performed at the Berkeley Sensors and Actuators Center at the University of California in the late 80's. Several modifications have been made since then to make it suitable for a multi-user environment. The process consists of a non-patternable nitride isolation layer, a polysilicon ground (plane) layer, two structural polysilicon layers, two oxide release layers, and one metal layer for electrical connection and reflectivity enhancement. The thickness of all layers has been chosen to suit most users, so that the process would be capable of supporting many different designs on a single silicon wafer.

The fabrication process begins with a $100mm$ n-type (100) silicon wafer, which is first heavily doped with phosphorus. This helps to prevent or reduce charge feedthrough to the substrate from electrostatic devices on the substrate. Next a $600nm$ low-stress LPCVD (low pressure chemical vapor deposition) silicon nitride is deposited on the wafers as an electrical isolation layer. This is followed by the deposition of a $500nm$ LPCVD polysilicon film, denoted as Poly0. Poly0 is then patterned by photolithography, a step that includes the coating of the wafers with photoresist, exposure of the photoresist with the appropriate mask and developing of

the exposed photoresist to create the desired etch mask for the subsequent pattern transfer into the underlying layer. After patterning the photoresist, the Poly0 layer is etched in an RIE (reactive ion etch) system. A $2\mu m$ PSG (phosphosilicate glass) sacrificial layer is deposited by LPCVD and annealed at $1050^{\circ}C$ for 1 hour in argon. This layer, known as First Oxide, is removed at the end of the process to free the first mechanical layer of polysilicon. The sacrificial layer is lithographically patterned with the anchor mask and reactive ion etched. After etching the anchor, the first structural layer of polysilicon, Poly1, is deposited at a thickness of $2\mu m$ and doped, by anneal of a thin ($200nm$) layer of PSG. This layer is etched to produce a hard mask for the subsequent polysilicon etch, and finally removed by RIE. After Poly1 is etched, a second PSG layer ($2\mu m$) is deposited (Second Oxide), annealed and patterned. At this stage, two different etch masks can be used: to etch in the Second Oxide down to Poly1, or to etch both First and Second Oxide, down to the level of Poly0 (or nitride). After this step, the second structural layer of polysilicon, Poly2, is deposited ($1.5\mu m$ thick), followed by a deposition of $200nm$ of PSG. As with Poly1, the thin PSG acts as both an etch mask and dopant source for Poly2. The wafer is annealed for one hour at $1050^{\circ}C$, before Poly2 is patterned and the PSG layer is etched by RIE. The final deposited layer is a $0.5\mu m$ metal layer, that provides for probing, bonding, electrical routing and highly reflective mirror surfaces. The wafer is patterned lithographically and the metal is deposited and patterned using lift-off. The wafers are diced and usually shipped to users for the sacrificial oxide release, which is done by immersing the chip in a bath of 49% HF, followed by DI water

Film	T [\AA]	SD [\AA]	SR [ohm/sq]	R [ohm-cm]
Nitride	6193	238	-	-
Poly0	5166	36	29.51	$1.53e^{-3}$
Oxide1	19870	793	-	-
Poly1	20334	168	10.54	$2.14e^{-3}$
Oxide2	7581	200	-	-
Poly2	15056	386	15.53	$2.34e^{-3}$
Metal	5628	-	0.05	$2.81e^{-6}$

Table 4.1: Some relevant data for Run 47 provided by the manufacturer. T = thickness, SD = standard deviation, SR = sheet resistance, R = resistivity.

and then critical point drying to reduce stiction.

The fabrication of our devices was part of run 47. Table 4.1 contains relevant data for this run relative to the different layers, as measured at the completion of the process. Here T is thickness, SD is standard deviation, SR is sheet resistance and R is resistivity. The values of thickness are included because they correspond to geometrical parameters of the device. They are used in Chapter 6 to compute the expected value of some characteristic parameters of the device (resonant frequency, electrostatic stiffness, etc.). The values of the electrical parameters are given for completeness, and to confirm that the polysilicon layers are conductive.

4.2 Device and Mask Design

In our design the cantilevers are arranged in arrays of ten elements, which we considered a number large enough to infer properties on the dynamical behavior of large arrays of electrostatically coupled units. A 3D schematic of the array is shown in Figure 4.1.

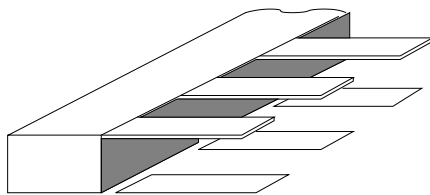


Figure 4.1: Final design for multicantilever array. The top plates are connected to a sturdy anchor, while the bottom plates are electrically isolated.

Notice that neither scales nor proportions are respected in this drawing, which has only illustrative purposes. As can be seen, the top plates are connected to a common base, while the bottom plates lay on the wafer surface and are electrically isolated.

This configuration was preferred over the one shown in Figure 4.2, where the cantilevers are separate, closely spaced units to make the device more robust to mechanical shocks, deriving for instance from the use of probes in testing, or the needle in the wire-bonder.

With the design shown in Figure 4.1 the top cantilevers share the same electrical connection, which is typically grounded, while the independent driving signals are applied through the bottom plates. Figure 4.3 is a micrograph of one of the arrays fabricated.

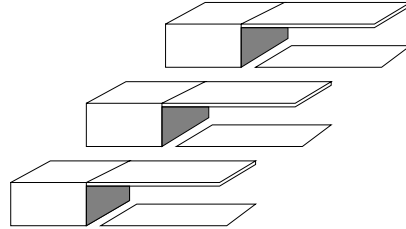


Figure 4.2: Initial design for multicantilever array. All cantilevers are electrically isolated and closely spaced.

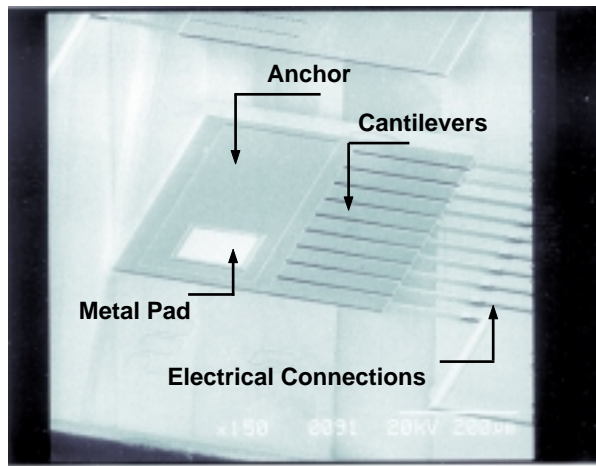


Figure 4.3: Micrograph showing the typical geometry of one of the arrays fabricated with PolyMUMPs.

More importantly, this configuration introduces mechanical coupling in the dynamics of the cantilevers, made even stronger by the presence of an overhang between anchor and cantilever beam, as depicted in Figure 4.4, which shows also a detail from the side view .

The length of the cantilevers in each array is the same, but each die

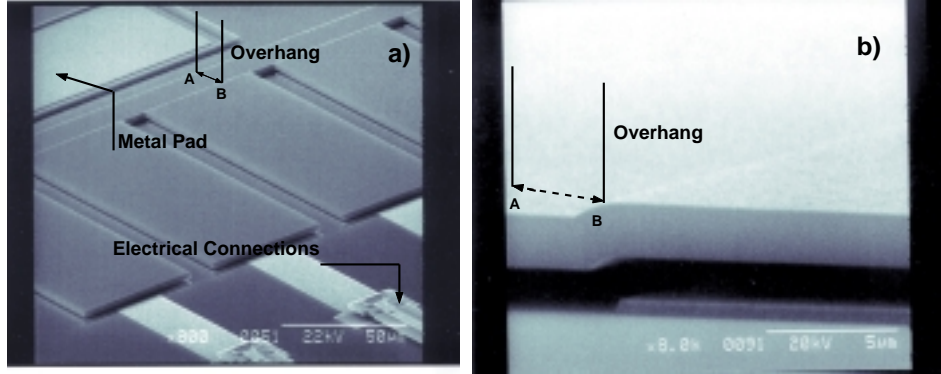


Figure 4.4: Micrograph showing the overhang between anchor and cantilevers base, responsible for the strong mechanical coupling.

contains arrays with different cantilevers lengths, in view of studying the effects of coupling on different geometries and also maximize the chances of obtaining working devices. In particular, the following values of length were considered : $L = 100 - 150 - 200 - 250 - 300 - 500 \mu m$. In all the dies utilized during testing, the 300 and 500 μm cantilevers were bent, touching the substrate; the 250 μm were occasionally standing, while the 100 – 150 – 200 μm were in most cases working devices. Figure 4.5 shows an array where half of the cantilevers are released and straight, and half are bent and touching the substrate.

The width of the cantilevers was chosen based on the minimum distance allowed by the PolyMUMPs process between neighboring cantilevers. Since this distance could be 5 μm at the least, we chose the width to be $w = 50\mu m$, in a ratio of $\frac{1}{10}$ so that the electrostatic coupling would be significant. Moreover, in order to study different cases of coupling strength,

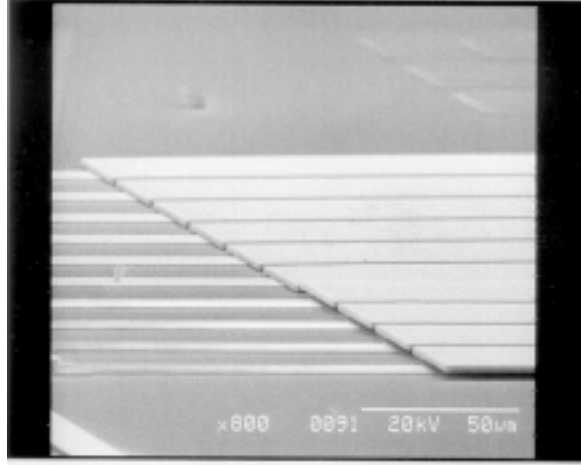


Figure 4.5: Micrograph showing an array with about half of the cantilevers correctly released and half touching the bottom plates (a phenomenon known as stiction).

the spacing between the cantilevers was designed to be either $5\mu m$ or $10\mu m$.

The gap between top and bottom plates was not a design parameter, but was fixed to $d = 2\mu m$, i.e. the thickness of the first oxide layer. Its micrograph is shown in Figure 4.6.

Finally, Figure 4.7 shows a close up image of one of the arrays.

As described in the previous section, the PolyMUMPs process consists of a non-patternable nitride isolation layer, a polysilicon ground (plane) layer, two structural polysilicon layers, two oxide release layers, and one metal layer for electrical connection and reflectivity enhancement. Up to eight masks can be designed for the patterning of these layers, according to need. We used only six of them. The first one patterned Poly0 to form

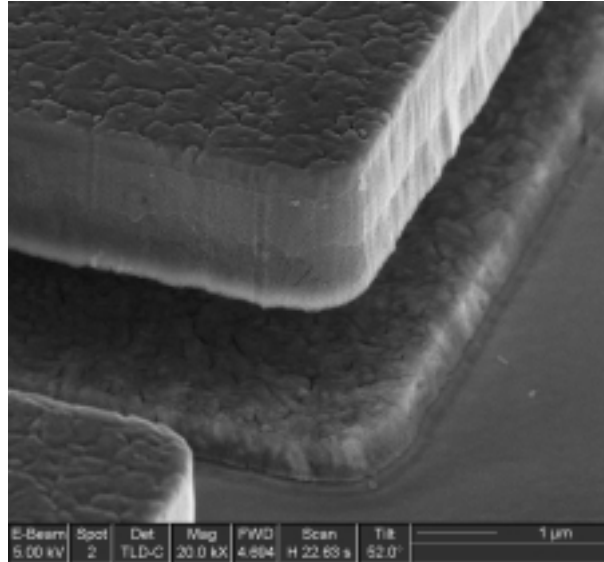


Figure 4.6: Micrograph showing the gap between top and bottom plates of each cantilever capacitor.

the bottom plates of the cantilevers capacitors and a bottom layer for the electrical contacts. The second one was used to pattern the First Oxide to obtain the anchors of the cantilevers. The third one patterned the Poly1 layer, to obtain the top plates of the cantilevers and the common anchor. The fourth one etched both First and Second Oxide to form a mask for the deposition of Poly2 for the electrical connections and the metal pad over the anchor. The fifth one removed the Poly2 from unwanted places, leaving it along the electrical connections only. The sixth and final mask was used for the metal deposition.

*

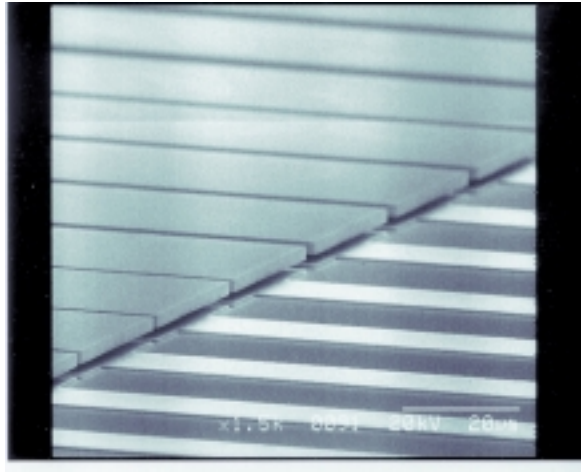


Figure 4.7: Close up image of one of the cantilever arrays. The lines visible are the electrical connections between bottom plates and metal pads.

Chapter 5

Mathematical Model

The translation of the qualitative physical behavior of a system into quantitative mathematical terms is a fundamental step in the engineering process. This chapter is devoted to the derivation of a mathematical model for both a single electrostatically actuated cantilever, (Section 5.1), and for a multicantilever array, (Section 5.2).

For a single cantilever and for the common case of sinusoidal excitation, we demonstrate, by using simple parallel plate theory that the dynamics are governed by a special second order linear periodic differential equation: the Mathieu equation. The model for a multicantilever array is similarly derived after incorporating the description of the coupling interactions that are both mechanical and electrostatic. In Section 5.2, we show how this results in a coupled Mathieu equation.

5.1 Single Cantilever Model

The schematic of a single cantilever sensor is shown in Figure 5.1. It consists of two adjacent electrically conductive beams forming the two plates of a capacitor. One of the beams is rigid, while the other (hereafter referred to as the cantilever) is fairly soft and represents the movable part of the structure. In the following, the cantilever is treated as a lumped-

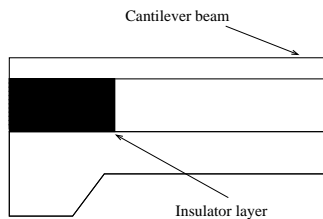


Figure 5.1: A schematic of an electrostatically driven cantilever.

parameter system, and hence described by only taking into account its first bending mode, and neglecting all higher order flexible modes. This approximation is quite common in the study of the dynamics of scanning probe cantilevers [89, 90, 91].

If the length of the cantilever is much bigger than its distance from the bottom plate, the capacitance can be expressed as

$$C(z) = \frac{\epsilon_o A}{d - z}, \quad (5.1)$$

where $\epsilon_o = 8.85 \cdot 10^{-12} \text{As/Vm}$ is the permittivity in vacuum, A is the area of the plates, d is the gap between them and z is the vertical displacement of the cantilever from its rest position.

If we adopt the parallel plate approximation and apply a voltage $V(t)$, then F_e , the electrostatic attractive force between the capacitor plates, can be expressed as

$$F_e = -\frac{d}{dz} \left[\frac{1}{2} C(z)^2 V(t) \right] = \frac{1}{2} \frac{\epsilon_o A}{d^2} \frac{V^2(t)}{\left(1 - \frac{z}{d}\right)^2}, \quad (5.2)$$

which under the further assumption that $\frac{z}{d} \ll 1$ and neglecting higher order terms, can be approximated as

$$F_e = \frac{1}{2} \frac{\epsilon_o A}{d^2} \left(1 + 2\frac{z}{d}\right) V^2(t). \quad (5.3)$$

Whence the equation of motion is given by

$$m\ddot{z} + \nu\dot{z} + kz = \frac{1}{2} \frac{\epsilon_o A}{d^2} \left(1 + 2\frac{z}{d}\right) V^2(t), \quad (5.4)$$

where $k = \frac{Ewt^3}{4L^3}$ is the spring constant of the cantilever (flexure-mode), E is the Young's modulus of the constitutive material, and L , w , t are length, width and thickness of the cantilever respectively.

If we apply a sinusoidal voltage $V(t) = V_o \cos \omega_o t$, equation (5.4) can be rewritten, after few algebraic steps, as

$$z'' + cz' + (a - 2q \cos 2t)z = u_f(t), \quad (5.5)$$

where the prime denotes the derivative with respect to the scaled time $\tau = \omega_o t$; c is a small damping coefficient, resulting from both air friction and structural losses, $a = \frac{k}{m\omega_o^2} - \frac{\epsilon_o A V_o^2}{md^3 \omega_o^2}$, $q = \frac{\epsilon_o A V_o^2}{2md^3 \omega_o^2}$, and $u_f(t) = q d \cos^2(t)$.

Equation (5.5) is an instance of the Mathieu equation, a well-known and studied differential equation that arises in boundary condition problems involving the wave equation. When $u_f(t) \equiv 0$, this equation has very

peculiar stability properties that have been extensively investigated and are recalled in Section 3.2. In our case of interest, where $u_f(t) \neq 0$ and periodic, one can prove that, for any pair of parameters a and q , the forced equation retains the same stability properties as the unforced one [81].

In our model, we consider the current generated as the output y of the system

$$y = i(t) = \frac{d}{dt}[CV(t)] = -\frac{\epsilon_o A}{d^2} \frac{V}{(1 - \frac{z}{d})^2} \dot{z} + \frac{\epsilon_o A}{d} \frac{\dot{V}}{(1 - \frac{z}{d})},$$

whose first order approximation is given by

$$y = c_1(t)z + c_2(t)z' + v_f(t), \quad (5.6)$$

where $c_1(t) = -\frac{\epsilon_o AV_o w_o}{d^2} \sin t$, $c_2(t) = \frac{\epsilon_o AV_o}{d^2} \cos t$, and $v_f(t) = \frac{\epsilon_o AV_o w_o}{d} \sin t$.

Introducing the vector $x = [z \ z']^T$, we can derive from (5.5) and (5.6) the state space representation of the cantilever model

$$\begin{aligned} x' &= A(t)x + B(t)u_f(t) \\ y &= C(t)x + v_f(t), \end{aligned} \quad (5.7)$$

where $A(t) = \begin{bmatrix} 0 & 1 \\ -a + 2q \cos 2t & -c \end{bmatrix}$; $B = \begin{bmatrix} 0 \\ 1 \end{bmatrix}$ and $C(t) = [c_1(t) \ c_2(t)]$.

Note that (5.7) is a linear time-varying and T -periodic model, with $T = \pi$. Section 6.2 offers a detailed account of the experimental validation of this model.

In the following section we show how this model can be modified to describe the dynamics of a tightly packed array of cantilevers, where the coupling interactions need to be taken into account.

5.2 Multicantilever Model

In this section we derive a mathematical model for the parallel connection of several electrostatically actuated microcantilevers. As illustrated

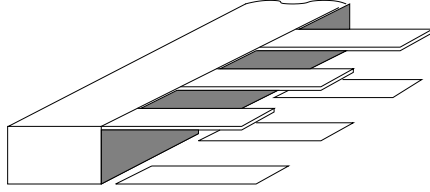


Figure 5.2: A schematic of the multicantilever array.

in Section 4.2 and schematically shown in Figure 5.2, the architecture we selected for the array configuration has the cantilevers connected to a common anchor, while the bottom plates are electrically isolated. Even though in this fashion each cantilever can be independently actuated, the proximity introduces coupling in their dynamics. More precisely, the coupling is mechanical because the microbeams are connected to the same base, and electrical due to the fringing fields generated by the capacitors nearby. As a consequence, the model introduced in the previous section for a single cantilever has to be modified to take into account this interaction.

The force acting on each microbeam consists of several components, so that the overall linearized equation of motion for the vertical displacement z_i , $i = 1, 2$, of each cantilever can be written as

$$\ddot{z}_i + \nu_i \dot{z}_i + \omega_{r_i}^2 z_i = F_{e,i} + F_{mc,i} + F_{ec,i}^\perp, \quad (5.8)$$

where ν_i and ω_{r_i} are the normalized damping coefficient and the natural resonant frequency of the i -th cantilever respectively. Here $F_{e,i}$ expresses

the electrostatic force between the capacitor plates of the i -th cantilever. As illustrated in the previous section, by using parallel plate theory, its linearized expression can be shown to be

$$F_{e,i} = \frac{\epsilon_o A}{2md^2} \left(1 + 2\frac{z_i}{d}\right) V_i^2,$$

where again $\epsilon_o = 8.85 \cdot 10^{-12} \text{As/Vm}$ is the permittivity in vacuum, d is the gap between the electrodes, A is the area of the capacitor plates, m their mass, and V_i is the voltage applied.

The mechanical coupling force $F_{mc,i}$ originates from the fact that the cantilevers are connected to the base through an overhang, visible in Figure 4.4 of Section 4.2. $F_{mc,i}$ has been modelled as a spring like force, proportional to the difference in the vertical displacement of the cantilevers,

$$F_{mc,i} = \sum_{j \neq i} \gamma_{i,j} (z_i - z_j).$$

Due to the symmetry of the array, the coefficients $\gamma_{i,j}$ are even functions of j , i.e. $\gamma_{i,j} = \gamma_{i,-j}$. Moreover, as it is reasonable to expect from a physical point of view, their value decays to zero as j tends to infinity.

As far as the electrostatic coupling is concerned, we assume that the voltage applied to each capacitor results in a charge induced on each cantilever. This can be expressed as

$$q_1 = \bar{c}_{1,1} V_1 + \bar{c}_{1,2} V_2 + \dots + \bar{c}_{1,N} V_N, \quad (5.9)$$

$$q_2 = \bar{c}_{2,1} V_1 + \bar{c}_{2,2} V_2 + \dots + \bar{c}_{2,N} V_N, \quad (5.10)$$

$$\vdots \quad (5.11)$$

$$q_N = \bar{c}_{N,1} V_1 + \bar{c}_{N,2} V_2 + \dots + \bar{c}_{N,N} V_N. \quad (5.12)$$

Note that when all conductors are grounded except the i th, which is kept at 1 Volt, $\bar{c}_{i,j}$ are equal to the charges q_j on the various cantilevers. Hence, from reciprocity it follows that $\bar{c}_{i,j} = \bar{c}_{j,i}$. Moreover, in order to maintain the i th cantilever at 1 V and the others at zero potential, q_i must be positive and all other charges negative. Therefore

$$\bar{c}_{i,i} \geq 0 \quad (5.13)$$

$$\bar{c}_{i,j} \leq 0 \quad i \neq j. \quad (5.14)$$

The interaction between these induced charges is described via a point charge model. The basic idea is shown schematically in Figure (5.3), that depicts only the case of two capacitors. Each cantilever is represented as a charged particle, q_i , and the mutual interaction is described by Coulomb's law

$$\begin{aligned} F_{ec,i} &= \frac{1}{4\pi\epsilon_o} \frac{q_i q_j}{r^2} \\ &= \frac{1}{4\pi\epsilon_o} \frac{(\sum_k \bar{c}_{i,k} V_k)(\sum_m \bar{c}_{j,m} V_m)}{[p_{ij}^2 + (z_i - z_j)^2]}, \quad j \neq i \end{aligned}$$

where $p_{ij} = |i - j|p$ is the pitch distance between the i -th and j -th capac-

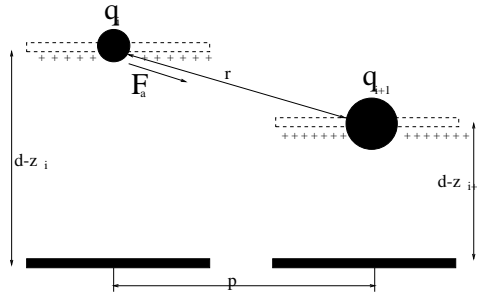


Figure 5.3: A schematic of the coupling capacitance model.

itors, and z_i is the vertical displacement of the i -th cantilever. We assume

that the lateral stiffness of the cantilevers is large enough to prevent any lateral motion, so that the only component of the force that mainly affects their behavior is the vertical one, whose first order approximation, in the case of two cantilevers, is given by

$$F_{ec,i}^\perp = F_{ec,i} \frac{z_i - z_j}{\sqrt{p_{ij}^2 + (z_i - z_j)^2}} = [c_{ii}V_i^2 + c_{i,j}V_iV_j + c_{j,j}V_j^2](z_i - z_j). \quad (5.15)$$

From equation (5.8) and for the special case of identical cantilevers, $\omega_{ri} = \omega_{rj} = \omega_r$, and equal inputs, $V_i = V_j = V_o \cos(\omega_o t) \forall j$, the state equations for the i -th cantilever become

$$\begin{aligned} x_1(t, i)' &= x_2(t, i) \\ x_2(t, i)' &= [-a_1 + 2q_1 \cos 2t]x_1(t, i) - cx_2(t, i) + u(t, i) + \\ &\quad + \sum_{j \neq i} [\Gamma_{i,j} + a_{ij} - a_{ij} \cos 2t] x_1(t, j), \end{aligned} \quad (5.16)$$

where the prime denotes the derivative with respect to the scaled time $\tau = \omega_o t$; $a_1 = a - \bar{a}$, $q_1 = q + \frac{\bar{a}}{2}$, with a and q defined in equation 5.5, \bar{a} being the sum of the convergent series $\bar{a} = \sum_{j \neq i} (\Gamma_{i,j} + a_{ij})$, $\Gamma_{i,j} = \frac{\gamma_{i,j}}{\omega_o^2}$, $a_{ij} = \frac{V_o^2}{2\omega_o^2} \sum_j k_{i,j}$, and $k_{i,j} = \sum_j c_{i,j}$. Note that here i is the spatial variable, introduced to denote the cantilevers in the array.

Equations (5.16) provide a local description of the system, where by local we mean limited to the i -th cantilever. However, no term in equations (5.16) is specific to the i -th cantilever, i.e. modulo a shift in the spatial index, these equations describe the dynamical behavior of any cantilever in the structure. Systems that satisfy this property are called *spatially-invariant* [64]. Some fundamental results in the theory for this class of systems have been presented in Section 2.3. In particular, we have seen that

by applying the Fourier transform in the spatial coordinate, the infinite dimensional system (5.16) can be associated with a parameterized family of finite dimensional ones

$$\begin{aligned}\hat{x}_1(t, \theta) &= \hat{x}_2(t, \theta) \\ \hat{x}_2(t, \theta) &= [-a(\theta) + 2q(\theta) \cos 2t] \hat{x}_1(t, \theta) - c \hat{x}_2(t, \theta) + \hat{u}(t, \theta)\end{aligned}\tag{5.17}$$

where the symbol $\hat{}$ denotes the Fourier transform in space, $\hat{a}(\theta) = a - \sum_{m \neq n} (\Gamma_{n,m} + a_{n,m}) e^{-i\theta m}$, $\hat{q}(t, \theta) = q - \sum_{m \neq n} a_{n,m} e^{-i\theta m}$. In the special case of a nearest-neighbor interaction, the parameters of equation (5.17) are given explicitly by

$$a(\theta) = a - 2(\Gamma_{12} + a_{12}) \cos \theta$$

and

$$q(\theta) = q - 2a_{12} \cos \theta.$$

*

Chapter 6

Experimental Characterization of the Device

This chapter describes the experiments that were performed to both characterize the dynamical behavior of electrostatically actuated cantilevers and validate the model proposed in Chapter 5.

The measurements were taken using the vibrometer testing technique, whose principle of operation is described in Section 6.1. Section 6.2 presents the experiments performed for the characterization of the dynamics of a single cantilever. The results show very good agreement with the behavior predicted by the model, both in the linear regime of operation and in parametric resonance. A similar analysis was conducted on pairs of coupled cantilevers. The results of testing are discussed in Section 6.3 and are used to provide validation for the model of the array of cantilevers.

6.1 Testing Technique Using a Vibrometer

Laser vibrometry was used to perform the experiments for characterization of cantilever dynamics and validation of the proposed model. The instrumentation suite is the one developed and characterized in [1, 92].

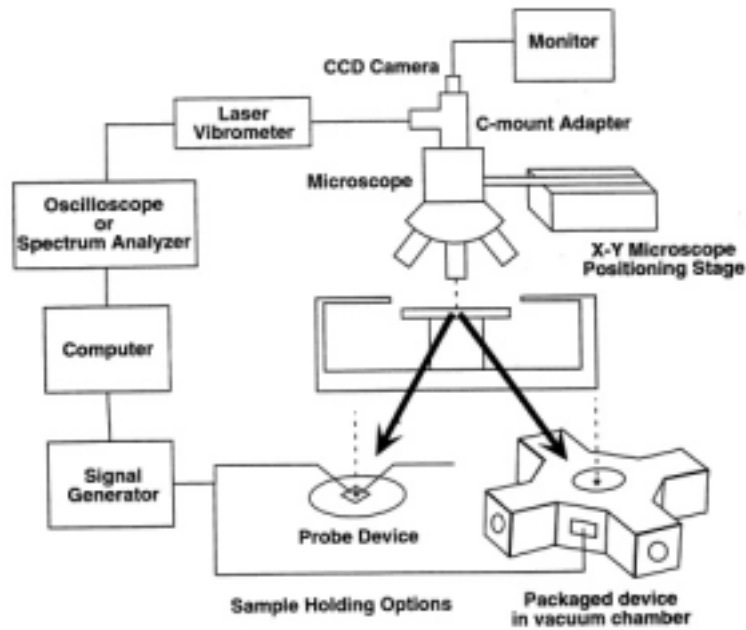


Figure 6.1: Schematic of the experimental setup, courtesy of [1].

Figure 6.1 is a schematic of the experimental setup. The device, packaged in a 24-pin IC carrier (Spectrum Semiconductor Materials, HYB20408), is lodged in a vacuum chamber and wire-bonded to the contact pins. The connection to the rest of the laboratory test equipment is via an electrical feed-through on the vacuum chamber. The pressure inside the chamber can be regulated and was kept at $p = 8\text{mtorr}$ during the experiments.

The excitation voltage for driving the devices being tested is generated by a power source (Hewlett Packard, HP3245A), while the oscillation velocity and position are measured at the free end of the cantilever using a laser vibrometer (Polytec, OFV 3001, OFV 511). The laser beam is focused onto the device using an optical microscope, which can be positioned over the sample via a computer controlled, mechanical x-y positioning mechanism. The measurement is based on interferometry, in which the idea is to split the laser beam into two (coherent) beams: one that impinges on the device tested, the other on a reference target. The relation between the difference in phase and the difference in path length traversed by the two beams is then translated into displacement of the beam. Due to the relatively high working frequency and the small displacement of the cantilevers ($f \approx 50\text{kHz}$ and $x = O(\text{nm})$), we worked with velocity measurements, which for high frequencies are more reliable and accurate than position measurements [52].

The results of these measurements are recorded and analyzed with a signal analyzer (Hewlett Packard, HP89410A) and oscilloscope (Tektronics, TDS 420A). The instruments are interfaced to a PC, where data can be stored for further analysis.

6.2 Testing of a Single Cantilever

We started out our experimental investigation of the dynamics of electrostatically actuated cantilever arrays by analyzing the behavior of a single cantilever. We realized that it was necessary to isolate the cantilever under

test from the others in the same array, by physically removing all cantilevers nearby. Because of mechanical coupling, which was stronger than initially expected, the dynamics of a given cantilever was heavily influenced by its neighbors, even when the neighbors were grounded. The first attempts at cutting the cantilevers with a Focused Ion Beam (FIB) was unsuccessful, because the ion beam would charge the capacitor plates and snap them into contact. Hence, we had to resort to breaking them off manually using a conventional probe tip.

The experiments reported in this section were conducted on $200\mu m \times 50\mu m \times 2\mu m$, highly doped polysilicon cantilevers, with a gap between the electrodes of about $2\mu m$. The cantilevers were fabricated using the MUMPS/CRONOS process, which was described in Section 4.1. Figure 6.2 is a micrograph of an actual device. The mechanical response of the

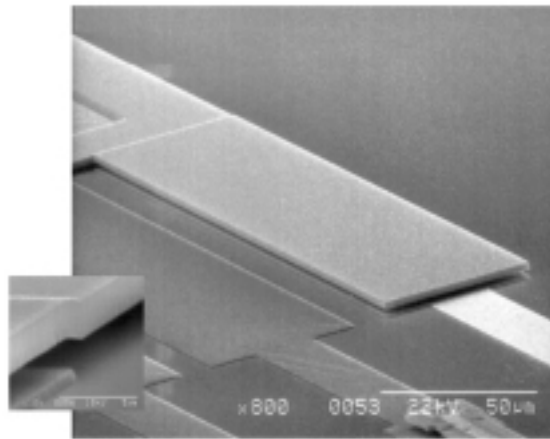


Figure 6.2: SEM image of a polySi cantilever. The inset shows details of the mechanical connection to the base.

cantilever was tested in vacuum using laser vibrometry [1] to measure velocity near its free end.

A preliminary set of experiments were done to verify that the value of the pressure used was low enough to guarantee a stable value of the quality factor Q , whence reliable data. The quality factor Q is a measure of energy loss in a system, and is defined as the ratio between the frequency of peak amplitude in the frequency response, f_r , and the bandwidth of the points f_1 and f_2 between which the amplitude is reduced by a factor of $\frac{1}{\sqrt{2}}$:

$$Q = \frac{f_r}{f_2 - f_1}.$$

Figure 6.3 shows the relation between Q and pressure. As expected, as the pressure p is lowered, Q increases, until it settles to an approximately constant value, independent of p .

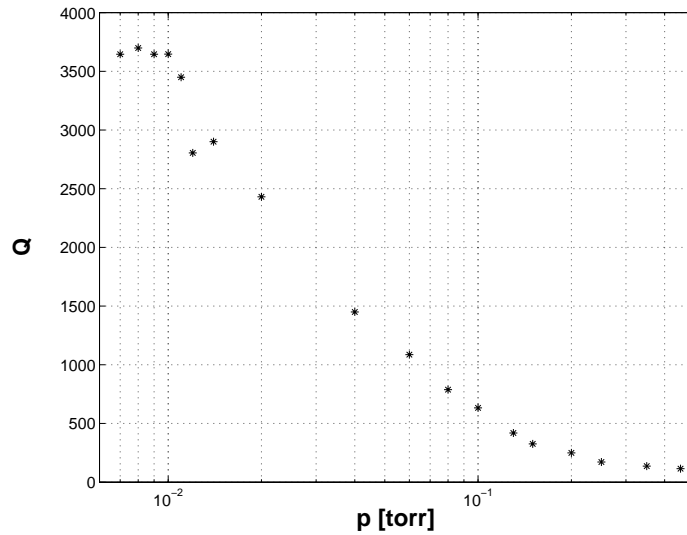


Figure 6.3: Variation of Q with pressure p .

The rest of the experiments reported in this dissertation was performed at a nominal pressure of $p = 8\text{mtorr}$, well within the flat region for the value of Q . Therefore we could disregard small fluctuations in the value of p , since these would not affect Q .

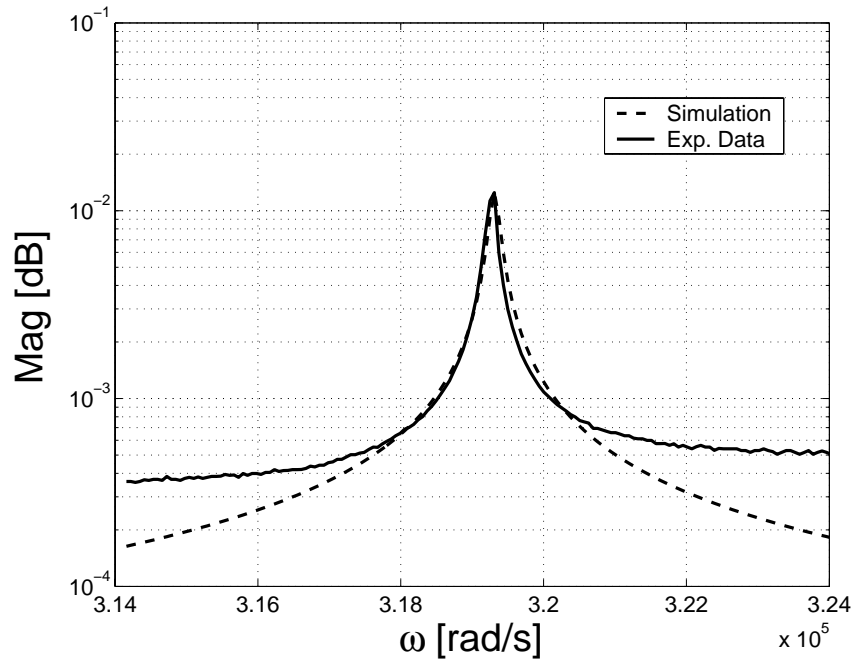


Figure 6.4: Frequency response of the cantilever: the solid line corresponds to measured data, the dashed one is its least square fit.

In our first experiments, we attempted to identify the system using as a simple mass-spring-damper model. In fact, when the amplitude V_o of the AC actuation voltage is small enough, the coefficient q in equation (5.5) is negligible, and the beam can be approximately described by an ordinary

second order differential equation,

$$\ddot{z} + 2\xi\omega_r\dot{z} + \omega_r^2z = u^2(t). \quad (6.1)$$

Figure 6.4 shows the magnitude, both measured and identified, of the frequency response of this model, excited by a square-rooted sinusoidal signal. A least square fitting of the data gives a resonant frequency of approximately $f_r = 50800$ Hz, a damping coefficient $\xi = 2.1 \times 10^{-4}$, while the quality factor $Q = 2200$ is, as expected, quite high. The value of these parameters was confirmed by time domain identification experiments as well. Figure 6.5 shows the measured velocity of the cantilever when subject to a step input. In fact, the descending fronts of the step can be considered to act as an impulse excitation. Hence, the frequency of free vibration of the beam corresponds to its natural frequency. At the same time, an exponential fit of the decay rate of this free response can be used to identify the damping factor ξ . The results obtained by this method were in very good agreement with those obtained by frequency identification, with an error in the order of 2%.

The Young's modulus for Cronos' polysilicon is $E = 158 \pm 10$ GPa and its density is $\rho = 2300$ Kg/m³. We assume that the effective thickness t of the capacitor coincides with its nominal value. Hence, from the experimental value of the resonant frequency and the formula $\omega_{rn} = \frac{1}{2} \frac{t}{L^2} \sqrt{\frac{E}{\rho}}$, we infer that the effective length of the capacitor plate is about $L = 160$ μm , opposed to a designed value of 200 μm .

It can be demonstrated experimentally that, by applying an external voltage to the cantilever, its resonant frequency ω_r is shifted by an amount that depends on the amplitude of that voltage. This phenomenon is easily

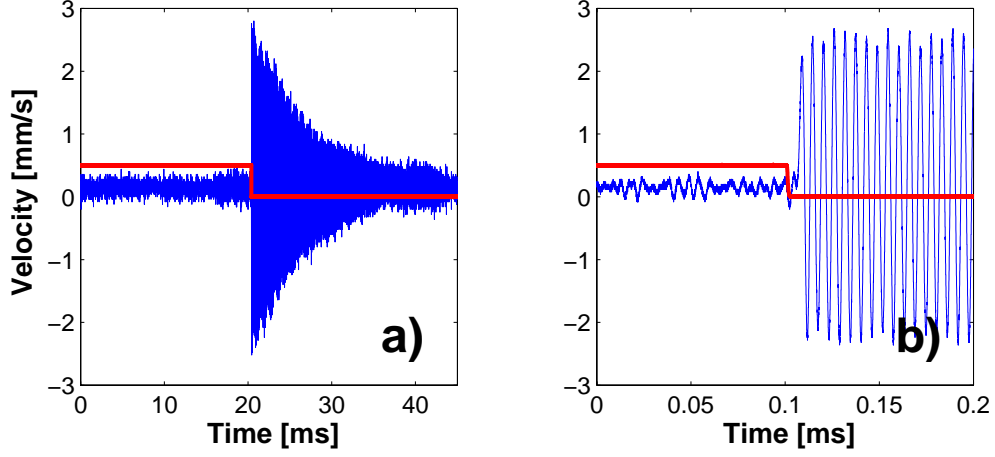


Figure 6.5: Analysis of cantilever response to a step input of amplitude $A = 50 \text{ V}$. a) Full trace showing exponential decay; b) detail showing oscillation at natural resonant frequency. The red line represents the input in arbitrary units.

explained by examining equation (5.5), from which we derive the following relation between resonant frequency and voltage applied

$$\omega_r^2 = \omega_{rn}^2 - \omega_e^2 V_o^2, \quad (6.2)$$

where ω_{rn} denotes the natural resonant frequency of the beam, and $\omega_e^2 = \frac{\epsilon_o A}{md^3}$ is what we call “electrostatic resonance”. To identify the value of ω_e we performed a set of experiments in which we applied a sinusoidal voltage

$$u(t) = V_{DC} + V_{AC} \cos \omega t,$$

with V_{DC} varying from $V_{DC} = -500 \text{ mV}$ to $V_{DC} = 300 \text{ mV}$, with increments of 100 mV . In this case, V_o of equation (6.2) is the effective input

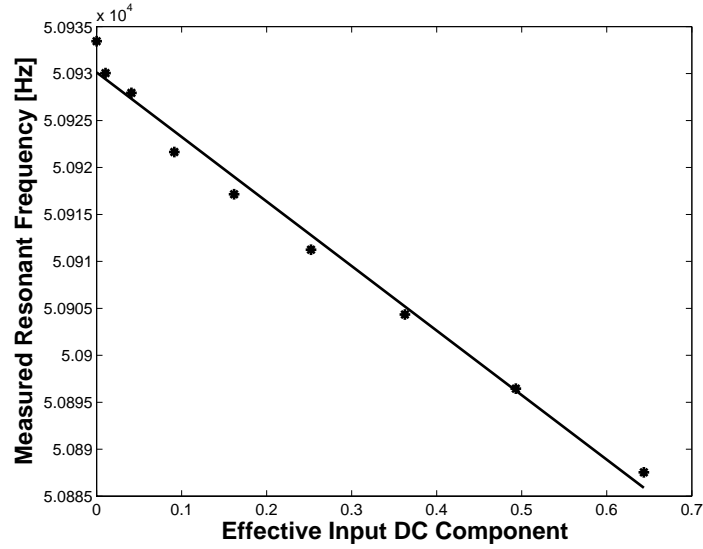


Figure 6.6: Experimental identification of the electrostatic resonance. The circles represent measured values of resonance frequency, the solid line is their linear fit.

DC component, $V_o^2 = V_{DC}^2 + \frac{1}{2}V_{AC}^2$. Figure 6.6 shows the experimental data collected, marked with a circle, and their linear fit, which gives a value of $\omega_e^2 = 2.63 \times 10^8 \text{ rad}^2/\text{s}^2\text{V}^2$, which is in good agreement with its theoretical value.

As the amplitude of the driving signal increases, the motion of the beam becomes larger and the linear approximation of equation (6.1) is no longer appropriate. A non linear cubic term, due to both mechanical and electrostatic forces, appears in the equation, which needs to be modified as follows:

$$\ddot{z} + 2\xi\omega_r\dot{z} + \omega_r^2z + a_3z^3 = u^2(t). \quad (6.3)$$

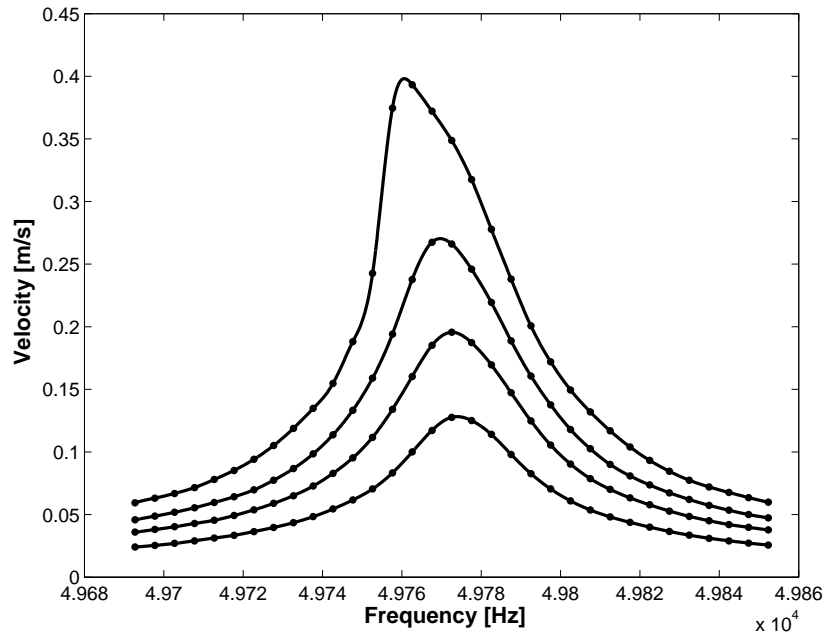


Figure 6.7: Effect of cubic nonlinearity on the frequency response of the cantilever. The dots denote experimental data, the solid lines their fit. Notice how the curve tilts on one side as the effect of the cubic term becomes no longer negligible.

The effect of the cubic nonlinearity is visible in Fig.6.7, which depicts the experimentally measured frequency response of the cantilever, when the input amplitude is varied from $V_o = 1$ V to $V_o = 2.5$ V in increments of 0.5 V. As the amplitude of V_o increases, the frequency response starts to tilt on one side, showing the characteristic behavior of a Duffing oscillator. The sign of the cubic coefficient determines the side to which the curve tilts. The two cases are known as the softening spring ($a_3 < 0$) and the

hardening spring ($a_3 > 0$), with the case depicted in Fig.6.7 corresponding to a negative coefficient.

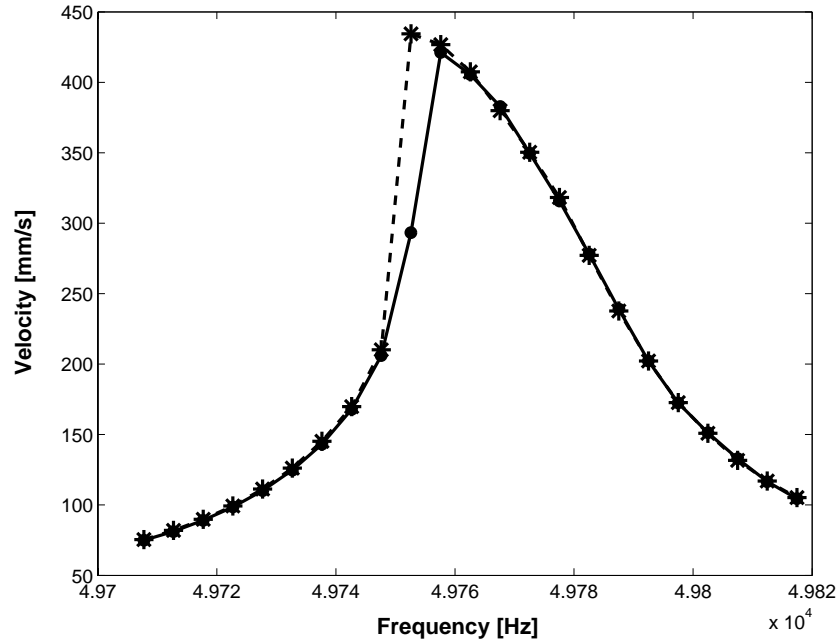


Figure 6.8: Effect of cubic nonlinearity on the frequency response of the cantilever. The circles correspond to data collected by sweeping the frequency from low to high, the asterisks to data collected by sweeping the frequency from high to low.

In dynamical systems terms, the tilt in the frequency response corresponds to the existence of a bistable region, where one small-amplitude and one large-amplitude stable harmonic solution coexist. Depending on the initial conditions, the solution of (6.3) converges to one of these two coexisting periodic attractors. Experimentally, this is reflected by the fact that the resonance response measured sweeping the frequency from low to

high is different from the one obtained by reversing the sweep direction (see Fig.6.8). It should be noted that in this region, there also exists an unstable solution, which cannot be recorded experimentally.

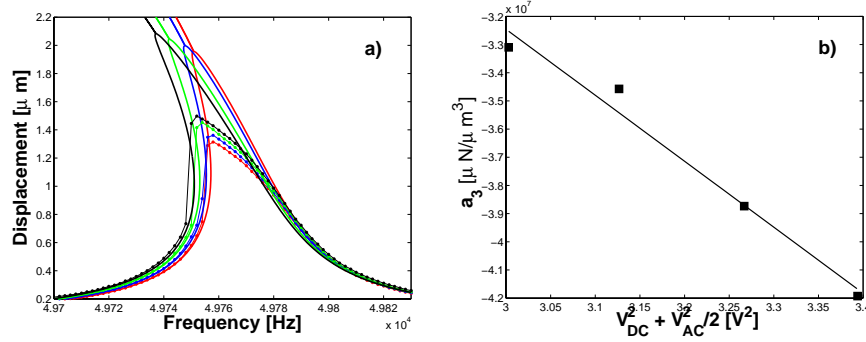


Figure 6.9: Experimental identification of the coefficient of cubic stiffness. Squares denote experimental data, solid lines their fit.

The coefficient of cubic stiffness a_3 can be decomposed into the sum of two parts: the mechanical contribution a_{3m} and the electrostatic contribution $a_{3e} = -\frac{2\epsilon_o A}{md^5}$. The expression for a_{3e} is derived from the power expansion of the electrostatic force F_e (see (5.3)). Note that it is multiplied by the square of the voltage amplitude, therefore its effect becomes stronger with increasing inputs. Figure 6.9 a) shows the least square fit of frequency response curves obtained for different values of the input voltage (from $V_o = 2.45$ V to $V_o = 2.6$ V with increments of 50 mV). Part b) of the same figure is the linear interpolation of the fitted data, which gives an estimate for the mechanical cubic stiffness of $a_{3m} = 3.6 \times 10^7 \frac{\mu\text{N}}{\mu\text{m}^3}$, and for the electrostatic stiffness $a_{3e} = 2.3 \times 10^7 \frac{\mu\text{N}}{\mu\text{m}^3}$, comparable to its theoretical

expected value $a_{3,e-theo} = 2.1 \times 10^7 \frac{\mu\text{N}}{\mu\text{m}^3}$.

Not only does the effect of the nonlinearities become more prominent as the input increases, but also the value of the coefficient q of the time varying term in (5.5)—which we have neglected so far—becomes larger. Hence the time invariant approximation (6.3) is no longer suitable for describing the dynamical behavior of the system and we need to return to the full non linear time-varying equation

$$\ddot{z} + c\dot{z} + [a - 2q \cos 2\omega_o t]z + a_3 z^3 = u^2(t), \quad (6.4)$$

where $c = 2\xi\omega_r$, $a = \omega_r^2$ and $q = \frac{\epsilon_o A V_o^2}{2md^3}$ from Section 5.1. Equation (6.4) is an example of a non linear, damped Mathieu equation with forcing. Its properties, in the absence of damping, external forcing and nonlinearity, have been discussed in some detail in Section 3.2, in which it was shown that the a - q parameter space can be divided into tongue-shaped stable/unstable regions.

These regions can be redrawn in terms of the physical parameters of the device. Let's neglect for the moment damping, external forcing and nonlinearity. If we rescale the time variable $\tau = \omega_o t$ in (6.4), we have

$$z'' + [\tilde{a} - 2\tilde{q} \cos 2\tau]z = 0, \quad (6.5)$$

with $\tilde{a} = \frac{a}{\omega_o^2}$ and $\tilde{q} = \frac{q}{\omega_o^2}$. Equation (6.5) is now a standard Mathieu equation, for which in Section 3.2 we have shown that the unstable regions occur for $\tilde{a} = n^2$, $n \in \mathbb{N}$. Thus, we obtain that the driving frequencies ω_o that cause unstable responses in the system are given by

$$\omega_o = \frac{\omega_r}{n} \approx \frac{\omega_{rn}}{n} \quad n \in \mathbb{N}, \quad (6.6)$$

where we have used the definition of $a = \omega_r^2 = \omega_{rn}^2 - \omega_e^2 V_o^2$, with the second equality coming from (6.2). Similarly, the boundaries of the first instability region, given by $\tilde{a} = 1 \pm \tilde{q}$ for (6.5), are defined in terms of frequency and amplitude of excitation by

$$\omega_o^2 = 2\omega_r^2 - 2 \left(1 \mp \frac{1}{2} \right) \omega_e^2 V_o^2, \quad (6.7)$$

which are obtained using the definition of q . It can be proved that the presence of a damping term has only the effect of shifting the tongues upwards in the a - q parameter space. In our setup this is of little consequence, because the magnitude of the shift is relatively small. However this is not always the case and in fact this is the reason why parametric resonance is difficult to observe at the macroscale.

Figure 6.10 is a comparison between the experimental data relative to the boundaries of the first instability region, and the same curves obtained from two sets of parameters. The solid line in Fig. 6.10 is the best fit of the experimental data using (6.7), the dash-dotted line is the fit of (6.7), in which the value of the parameters is that of the frequency response identification. In these experiments the cantilever was excited by a square rooted sinusoidal input, to avoid the presence of a harmonic component in the input. Thus, the condition (6.6) has to be modified as $\omega_o \approx \frac{2\omega_{rn}}{n}$. In fact, in this case the time scaling required to transform the dynamical equation into an equation equivalent to (3.2) is $\tau = \frac{\omega_o t}{2}$.

Inside the “tongue”, the cantilever oscillation does not grow unbounded, as predicted by the linear analysis. As discussed in Section 3.2, the presence of a nonlinear cubic term in (6.4) has the effect of bounding the amplitude of the oscillation. What we observe when driving the cantilever in the

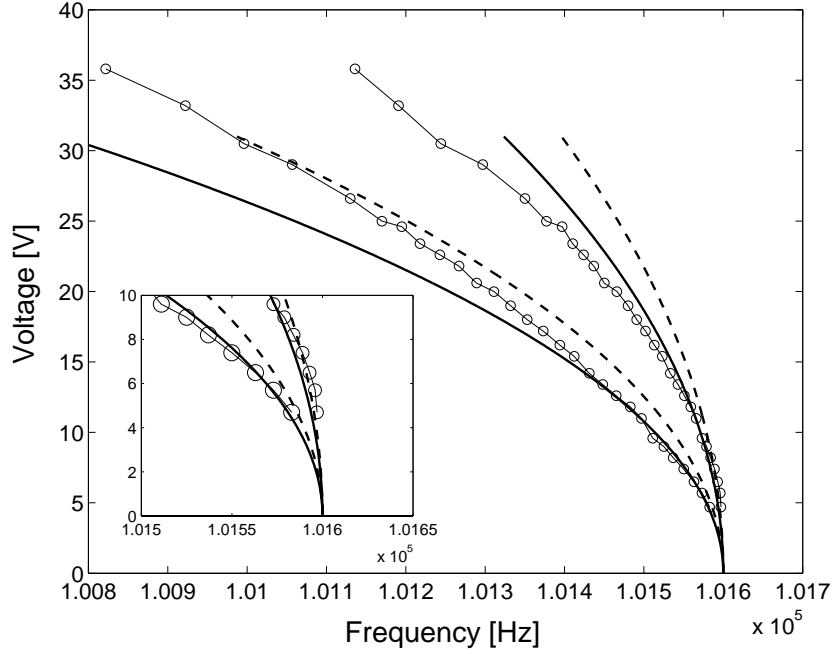


Figure 6.10: First instability region: experimental data points (circles) and curves with identified parameters. The inset shows the upward shift of the tongue caused by damping.

parametric resonance regime is a subharmonic 2:1 oscillation of the beam [83]. As shown in Fig.6.11, the cantilever vibrates at half the frequency of excitation (oscilloscope data). Also, note that during the transition from non-parametric to parametric region, the response shows a characteristic exponential growth (see Fig. 6.12).

Above the critical driving voltage amplitude, and for driving frequencies near the first parametric resonance, the response of the cantilever has the shape depicted in Fig.6.13. The two curves shown represent data collected by sweeping the driving frequency from low to high ('+' points) and

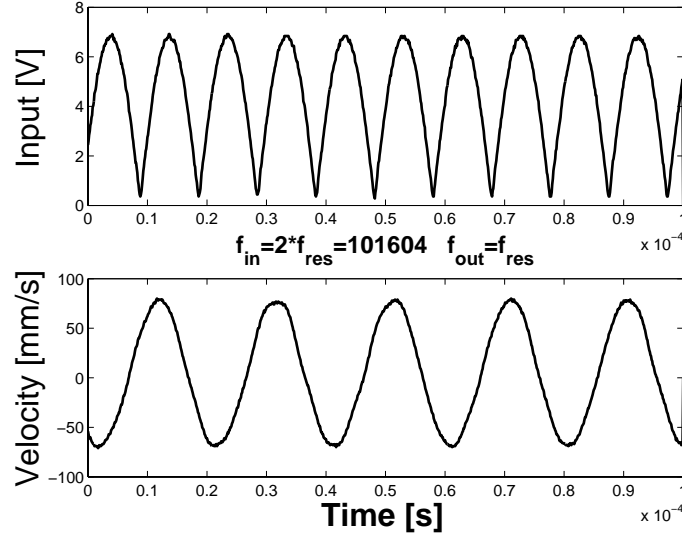


Figure 6.11: Time series of typical input and output signals inside the first “tongue” (oscilloscope data). Note the response is at half the driving frequency.

from high to low (‘o’ points), as indicated by the arrows. The vertical axis represents the amplitude of the periodic (half frequency) velocity of the beam, while the horizontal axis is the frequency of excitation. We noted earlier that this kind of plot is typical of oscillators having a cubic nonlinearity (Duffing). What is worth noting here is the sharp transition of the output response (vertical segment of ‘+’ data) that marks the entrance into the parametric region (region **II**). Since this transition always occurs for the same value $\omega_1 \approx 2\omega_r$, related to the resonant frequency of the beam, the phenomenon has potentially many applications, from the realization of mechanical filters [42, 43, 65, 68] to extremely sensitive mass sensors

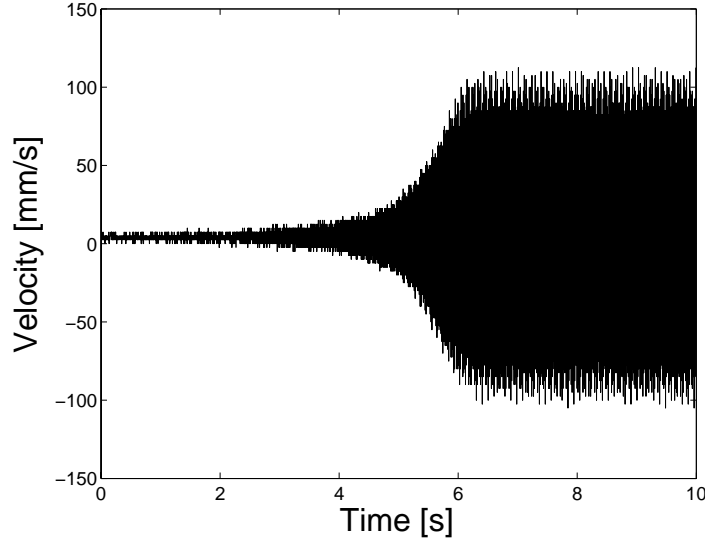


Figure 6.12: Exponential growth of oscillation following parametric excitation. Experimental data.

[66]. Inside the parametric region, the system exhibits a stable periodic oscillation, whose amplitude decreases as the driving frequency increases, until it goes to zero upon exiting the region (region **III**). Note that the size of the interval $[\omega_1 \ \omega_2]$ corresponds to the width of the parametric tongue represented in Fig. 6.10 for the considered input amplitude value. If we reverse the process and start decreasing the frequency, the output amplitude, which is zero at the beginning, starts to increase as soon as we enter the parametric region. This subharmonic periodic solution remains stable even after leaving the region and its amplitude keeps increasing (region **I**). However, it is only a matter of time before it collapses to zero. The location of this second jump is not predictable and depends on the amplitude of the frequency decrements, i.e. on the initial conditions.

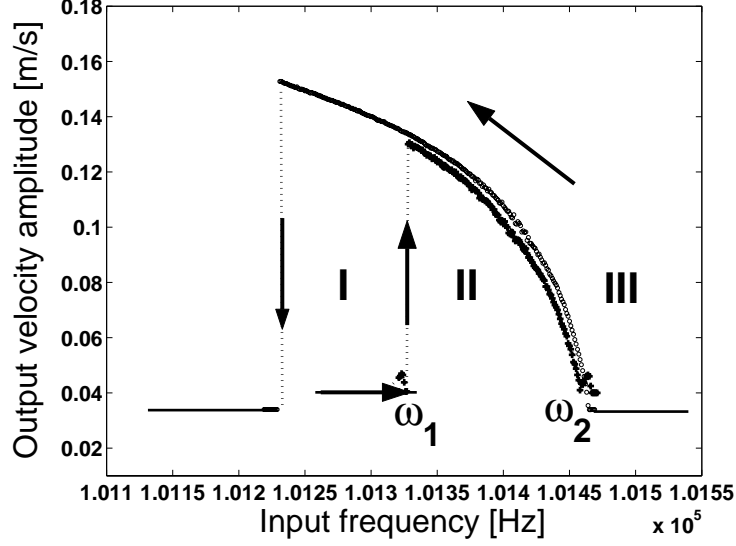


Figure 6.13: Frequency response above critical driving voltage amplitude ($A = 10\text{ V}$). The solid and dashed lines have been added to the experimental data points (marked with ‘ o ’ and ‘+’) to facilitate the reading.

To conclude this section, we point out that these experimental results reproduce the expected behavior obtained by analysis and simulations in Section 3.2.

6.2.1 Combined Harmonic-Parametric Response

When driving the system with a sinusoidal voltage, $V(t) = V_{DC} + V_o \cos \omega t$, equation (6.4) becomes

$$z'' + cz' + (a - 2p \cos t - 2q \cos 2t)z + a_2 z^3 = b_o + b_1 \cos t + b_2 \cos 2t, \quad (6.8)$$

where $p = \frac{\epsilon_o A V_{DC} V_o}{2md^3 w_o^2}$, $b_o = V_{DC}^2 + \frac{V_o^2}{2}$, $b_1 = pd$, and $b_2 = qd$. When the frequency of the driving signal is close to the resonant frequency w_r of the

cantilever, this input has both harmonic (w) and parametric ($2w$) components. It has been observed experimentally that the steady-state frequency sweep response above a critical drive amplitude changes dramatically from the pure parametric case, shown in Fig.6.13.

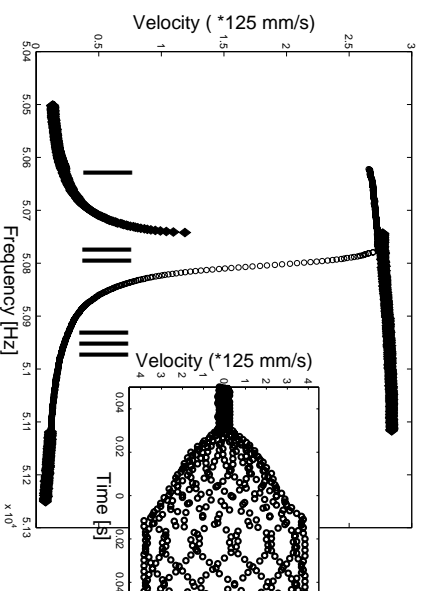


Figure 6.14: Combined harmonic/parametric frequency response. Note that there are bistable regions (I and III) on either side of the parametric tongue (II).

The symbol ‘ \diamond ’ corresponds to the frequency being swept up and the symbol ‘ \circ ’ to the frequency being swept down. The figure also shows the time response when the cantilever forcing is changed from a non-parametric region to a parametric region. Notice that the rate of growth, initially characteristic of harmonic resonance, becomes exponential, as expected for parametric mode of oscillation. Fig.6.15 shows the mapping of the parametric resonance region in the drive amplitude–frequency plane.

The effect of the direct forcing is to transform the trivial stable solution of region III into a non-trivial frequency dependent stable periodic solution.

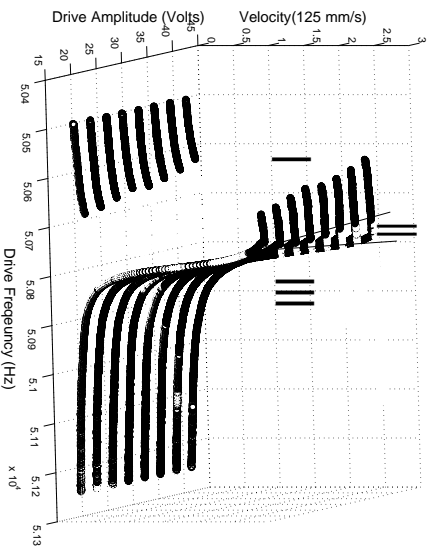


Figure 6.15: The first instability region with combined harmonic and parametric excitation. Note that at the boundary between regions I and II, there is still a distinctly sharp transition between small and large amplitude response, making it useful for applications.

When driven in region I or III, the response of the cantilever is one of the two stable states, depending on the initial conditions. The overall response is richer than the pure parametric case because of the presence of bi-stable regions. The sharp transition from a small periodic response to a large one with change of drive frequency is also seen in this case. Hence applications that use these sharp transitions can be implemented in this mode as well. As it is extremely hard to avoid a harmonic forcing term in most sinusoidally driven applications, the presence of a sharp transition is extremely promising.

6.3 Testing of a Pair of Cantilevers

As a second natural step in the experimental investigation of the dynamics of electrostatically actuated cantilever arrays, we have analyzed the case of a pair of cantilevers. This can be considered as the simplest example of an array because it has all the important features of more complex configurations, such as independent actuation and coupled dynamics. Hence, studying it can provide useful insight into the behavior of larger arrays and validation for the infinite array model as well.

Figure 6.16 shows the geometry of the device. It consists of two microbeams connected to the same base, each forming a micro-capacitor. By applying a voltage across the plates, each cantilever can be independently actuated. As discussed in the previous section and as shown in Fig. 6.16, all nearby cantilevers in the array had to be removed, because the strong mechanical coupling between them would corrupt the measurements.

Similar to the single cantilever case, each beam is $200\mu m \times 50\mu m \times 2\mu m$ highly doped polysilicon, with a gap between the electrodes of about $2\mu m$ and separated by a distance of $5\mu m$.

In this case also, experiments were performed in vacuum ($p = 8$ mtorr), using laser vibrometry [1] to measure velocity near the free end of each cantilever. The close spacing and the fact that the cantilevers are connected to a common base introduces coupling in their dynamics, which is both electrostatic and mechanical. Even though this might be considered a drawback of the design, the close spacing allows for a higher throughput device. We will show how the electrostatic coupling adds features to the device, which are interesting from an engineering point of view. Moreover,

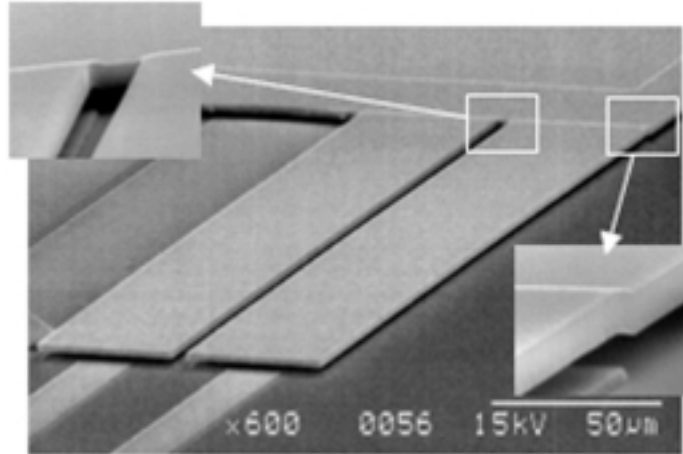


Figure 6.16: SEM micrograph of the device. The insets show details of the mechanical connection to the base and between the cantilevers.

in Section 8.1, we demonstrate how the system can be effectively decoupled using an appropriate control strategy.

In Section 5.2, we have derived a model for an array of microcantilevers that explicitly incorporates the mechanical and electrostatic couplings. Recall that the mechanical coupling was modelled as a spring like force, while the electrostatic coupling was modelled as a Coulomb interaction force between charged particles. By specializing that model to the case of two cantilevers, and for the particular but relevant case of $V_i = V_{oi} \cos \omega t$, we obtain the following linearized equation of motion for the vertical dis-

placement z_i of each cantilever:

$$\begin{aligned} & \begin{bmatrix} \ddot{z}_1 \\ \ddot{z}_2 \end{bmatrix} + \begin{bmatrix} \nu_1 & 0 \\ 0 & \nu_2 \end{bmatrix} \begin{bmatrix} \dot{z}_1 \\ \dot{z}_2 \end{bmatrix} + \\ & + \left\{ \begin{bmatrix} \omega_1^2 & \gamma_1 \\ \gamma_1 & \omega_2^2 \end{bmatrix} + \begin{bmatrix} \epsilon_1 & \gamma_2 \\ \gamma_2 & \epsilon_2 \end{bmatrix} \cos(2\omega t) \right\} \begin{bmatrix} z_1 \\ z_2 \end{bmatrix} = \begin{bmatrix} b_1 & 0 \\ 0 & b_1 \end{bmatrix} \begin{bmatrix} V_1^2 \\ V_2^2 \end{bmatrix} \end{aligned} \quad (6.9)$$

where $\omega_i^2 = \omega_{r_i}^2 - \Gamma - (K_e V_{o_i}^2 + K_T)$, $\epsilon_i = -(K_e V_{o_i}^2 + K_T)$, $\gamma_1 = \Gamma + K_T$, $\gamma_2 = K_T$, $K_T = (K_{11} V_{o_1}^2 + K_{12} V_{o_1} V_{o_2} + K_{22} V_{o_2}^2)/2$, $b_1 = K_e d/2$ and $K_e = \epsilon_o A/(md^3)$; or equivalently, introducing the vector $Z = [z_1 \ z_2]^T \in \mathbb{R}^2$, $U = [V_1^2 \ V_2^2]^T$ and defining the appropriate matrices

$$\ddot{Z} + \nu \dot{Z} + [\Delta + \epsilon E \cos(2\omega t)]Z = kU, \quad Z \in \mathbb{R}^{2 \times 1} \quad (6.10)$$

where ϵ represents a small perturbation parameter. The results presented in the rest of this section will justify this notation.

Eq.(6.10) represents a system of periodic differential equations, which we refer to as a *vector Mathieu equation*, since its algebraic structure is reminiscent of the famous Mathieu equation. In the absence of coupling, they reduce to a pair of independent scalar Mathieu equations, which describe the dynamics of an isolated beam [37].

6.3.1 Linear Regime of Operation

The first set of experiments was performed to characterize the system in its linear regime of operation, that is for small input signals. When the amplitude of the applied voltage V_{o_i} in Eq.(6.10) is small, the time-varying

coefficients can be neglected and the device is described by a system of second order ordinary differential equations.

$$\ddot{Z} + \nu\dot{Z} + \Delta Z = kU. \quad (6.11)$$

Let G_{ij} denote the transfer function from the voltage input applied to the j -th cantilever to the velocity output measured on the i -th cantilever, when the other voltage input is set to zero. The analytical expression of these transfer functions can be found to be

$$G_{ii} = \frac{b_1 s(s^2 + \nu_i s + \omega_{r_i}^2 - \Gamma + K_{ii} V_{o_i}^2)}{(s^2 + \nu_i s + \omega_{r_i}^2 - \Gamma - (K_e - K_{ii}) V_{o_i}^2)(s^2 + \nu_j s + \omega_{r_j}^2 - \Gamma + K_{ii} V_{o_i}^2) - (\Gamma - K_{ii} V_{o_i}^2)^2},$$

$$G_{ij} = -\frac{b_1 s(\Gamma - K_{ii} V_{o_i}^2)}{(s^2 + \nu_i s + \omega_{r_i}^2 - \Gamma - (K_e - K_{ii}) V_{o_i}^2)(s^2 + \nu_j s + \omega_{r_j}^2 - \Gamma + K_{ii} V_{o_i}^2) - (\Gamma - K_{ii} V_{o_i}^2)^2},$$

which, by introducing the appropriate parameters, can be rewritten in the following form, which is more convenient for subsequent analysis

$$G_{ii} = \frac{b_1 s(s^2 + \nu_i s + \omega_{z_i}^2)}{(s^2 + a_{1i} s + \omega_{pk1}^2)(s^2 + a_{2i} s + \omega_{pk2}^2)}, \quad (6.12)$$

$$G_{ij} = \frac{c_i s}{(s^2 + a_{1i} s + \omega_{pk1}^2)(s^2 + a_{2i} s + \omega_{pk2}^2)}.$$

Figure (6.17) represents the experimental and fitted data of these frequency responses. Notice the presence of two peaks in the frequency response of each single cantilever, a consequence of coupling, predicted by Eq.(6.12). This frequency characteristic leads to potentially interesting applications in the field of micromechanical (pass-band) filters [93]. The peaks correspond to the so-called normal modes of the system and their values coincide approximately to ω_{pk1} and ω_{pk2} . The center frequency is determined primarily by the frequencies of the constituent resonators, while the spacing between the modes is determined largely by the strength of the mechanical

coupling. This fact can be used advantageously to implement filters with tunable center frequencies. In fact, the center frequency can be adjusted by applying an appropriate DC bias, as illustrated by (6.2) in the previous section. It can be proved that each mode peak corresponds to a distinct, physical mode shape. In particular the oscillation of the microbeams is in phase for $\omega = \omega_{pk1}$ and in anti-phase for $\omega = \omega_{pk2}$ [94].

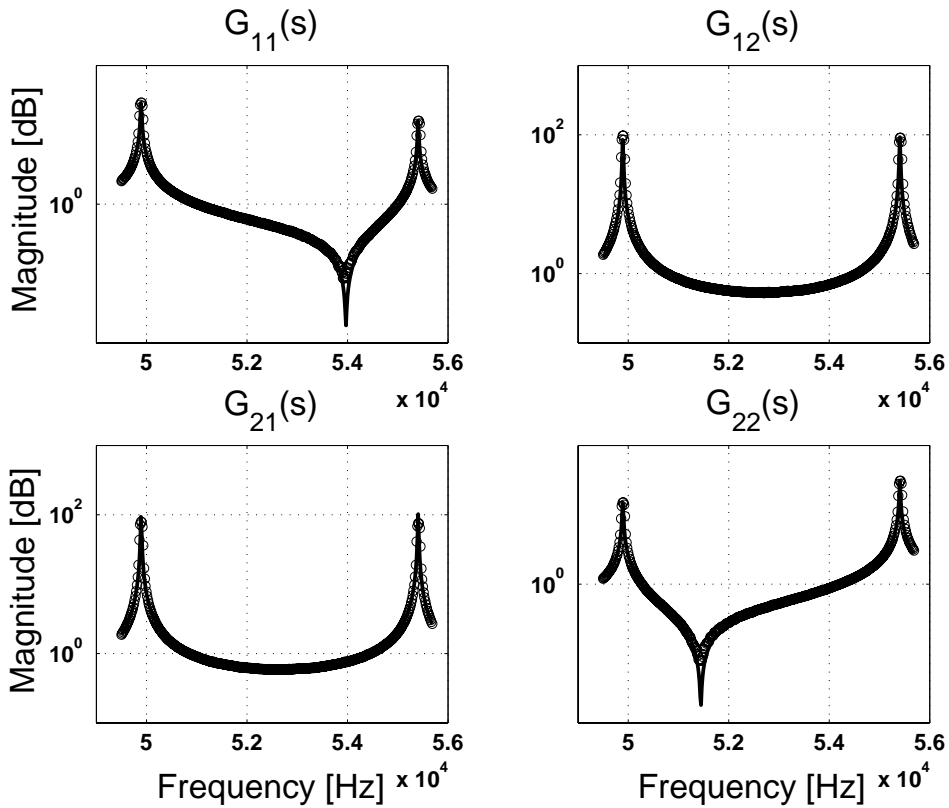


Figure 6.17: Magnitude of the frequency responses of the coupled cantilevers with different input/output combinations. The circles represents experimental data; the solid line the fitted data.

By fitting our model to the experimental data, as shown in Figure (6.17), we find that the resonant frequencies of the isolated beams are $\omega_{r1} = 48870Hz$ and $\omega_{r2} = 51520Hz$ respectively, while the quality factors are $Q_1 = Q_2 \approx 3000$. The difference between the values of ω_{r1} and ω_{r2} , in spite of the fact that the beams have the same geometry and material, is to be attributed to the asymmetry of the anchor in the point where it connects to the beams, visible in Figure(6.16) and also in the ANSYS model of Figure(6.20).

Identification of Mechanical and Electrostatic Coupling Coefficients

The coefficient of mechanical coupling Γ was estimated using the Power Spectral Density (PSD) of the vibrations induced by thermal noise. In fact, by setting both inputs to zero, the electrostatic coupling is eliminated and the effect of Γ can be isolated. More precisely, the location of the peaks in the frequency responses is, in this case, solely determined by Γ . Figure (6.18 c,d) shows the experimental characterization of noise that, as expected, has a Gaussian distribution. From stochastic filtering theory it is known that the PSD S_y of the output of a linear system G excited by random noise e is given by

$$S_y(\omega) = G(\omega)G(\omega)^*S_e(\omega) = |G(\omega)|^2S_e(\omega), \quad (6.13)$$

where S_e is the PSD of the input noise. In our case, since the system has two inputs, and the noise on each of them is mutually independent,

Eq.(6.13) becomes

$$\begin{aligned} S_{y_i}(\omega) &= |G_{ii}(\omega)|^2 S_{e_i}(\omega) + |G_{ij}(\omega)|^2 S_{e_j}(\omega), \\ &= (|G_{ii}(\omega)|^2 + |G_{ij}(\omega)|^2) S_e(\omega), \end{aligned} \quad (6.14)$$

where the last equality follows from the fact that e_1 and e_2 have the same stochastic description. Since the PSD S_e of thermal noise is constant, Eq.(6.14) suggests a way to extrapolate the value of Γ from the value of the normal modes. Parts a) and b) of Figure (6.18) show the comparison between measured data and a fit using Eq.(6.14). Note that the region between the two peaks is below the noise level of our instrumentation, hence a good fit cannot be obtained.

By examining the numerator of G_{11} and G_{22} in (6.12), we can notice the presence of a resonant zero, visible also in Fig.(6.17) as a dip in the magnitude plot of these functions. This zero frequency is called antiresonance [94], and its value is approximately equal to $\omega_{zi}^2 = \omega_{ri}^2 - \Gamma + K_{ii}V_{oi}^2$. This expression highlights that its existence is due to the mechanical and electrostatic coupling, and its location changes with the amplitude of the driving voltage. This property gave us a way to estimate the values of the electrostatic coefficients K_{11} and K_{22} , as shown in Figure 6.19 a) and b). In fact, the shift in the zero location depends linearly on the voltage applied, and the coefficient of proportionality is given by K_{11} for G_{11} and K_{22} for G_{22} . In a similar fashion, the coefficient K_e was estimated from the shift in the poles with the applied AC voltage. Finally, the coefficient K_{12} was estimated by applying the same voltage to both inputs. In this case the system is specified by only two transfer functions, whose analytical expression can be easily derived from (6.11). In particular, the numerator

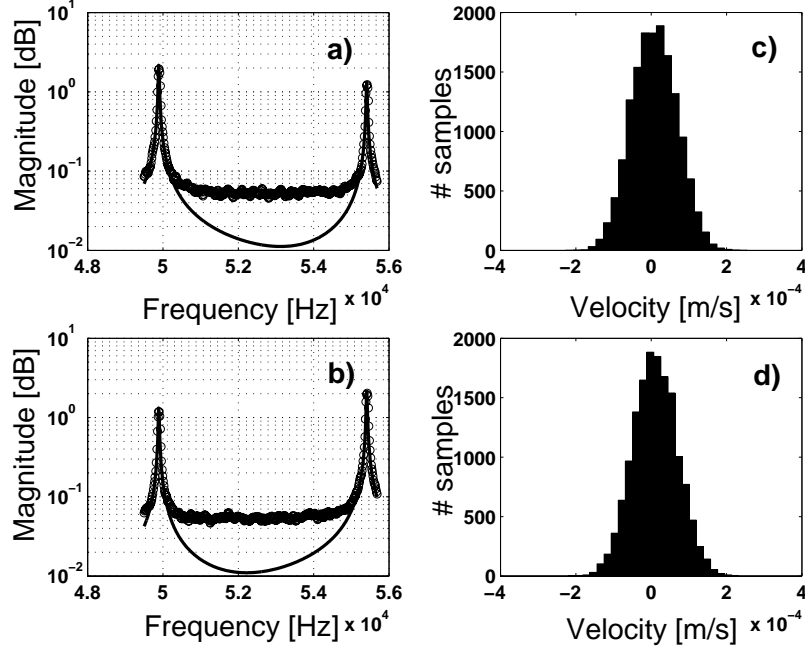


Figure 6.18: Fit of PSD of thermal noise to determine Γ : a) cantilever 1, b) cantilever 2. The region between the two peaks is below the noise level of our instrumentation. c,d) Experimental characterization of noise distribution (10^4 samples of the noise signal at the vibrometer output).

of the transfer function of cantilever 1 turns out to be

$$n_1(s) = b_1 s(s^2 + \nu_2 s + \omega_{r2}^2 - 2\Gamma - K_e V_o^2 + 2K_T) = b_1 s(s^2 + \nu_2 s + \tilde{\omega}_{z1}^2).$$

From this expression we can see that also in this case the location of the zero is related to the changes with the amplitude of the AC voltage applied, V_o .

It is worth noting that the equivalent stiffnesses corresponding to these electrostatic coupling parameters are quite large, indicating significant cou-

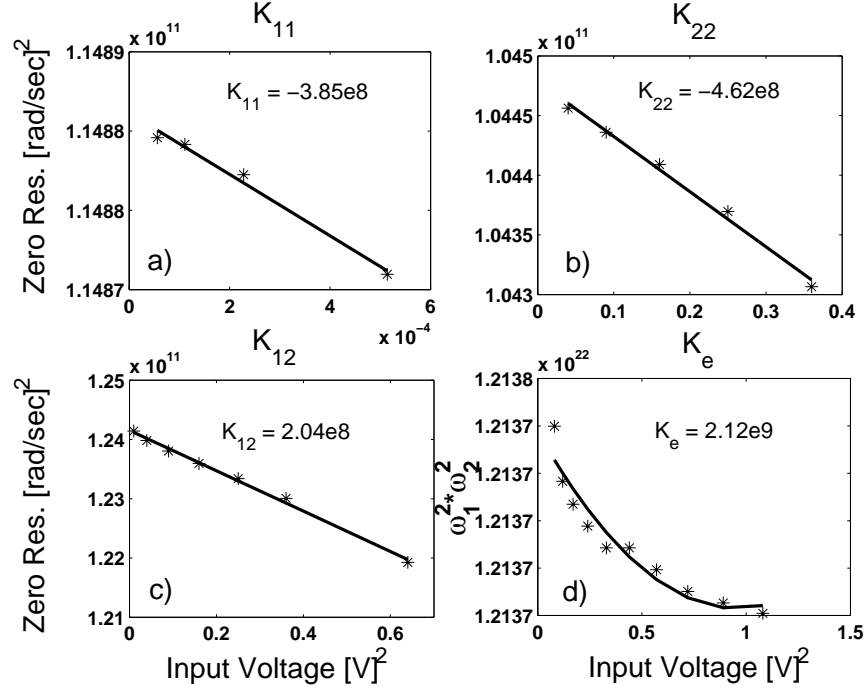


Figure 6.19: Experimental estimation of the electrostatic coefficients. K_{ij} are the coefficients of the electrostatic coupling force, $F_{ec,i}$; K_e is the coefficient of the attractive force, $F_{e,i}$, between the cantilever and its ground plate.

pling in this system, but two orders of magnitude smaller than the mechanical stiffness of the uncoupled cantilever, justifying the notation of (6.15), where they are represented as a perturbation to a time invariant equation.

Finite Element Method Simulations

We performed simulations using finite element methods to verify the experimental findings. The pair of cantilevers has been modelled according

to the actual physical configuration, as shown in Fig.(6.16). In particular, both the anchor and the overhang which connects the two beams have been explicitly incorporated in the model. The geometry generated in ANSYS is shown in Fig.(6.20 a). The values of the first two modes, found by modal analysis using the element *Solid92*, match well with the values of the two peaks in the frequency response found experimentally. Fig.(6.20 b,c) shows the ANSYS model corresponding to the isolated cantilevers. These models have been used to determine the resonant frequency of the uncoupled cantilevers. Table I presents values of several significant parameters ob-

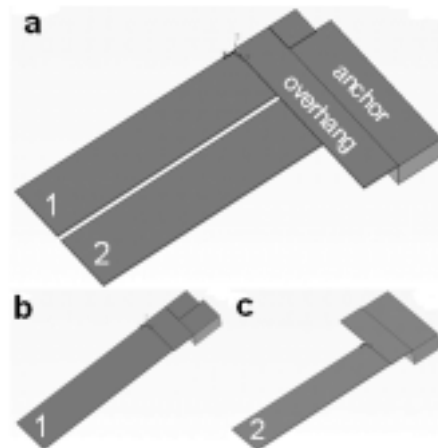


Figure 6.20: Ansys model of the cantilever pair a), and of the single cantilevers b,c).

tained by identification and compares them with the value obtained by finite element simulations. The agreement is satisfactory.

As the amplitude of the driving signal increases, so do the values of ϵ_i and γ_2 and this linear time-invariant approximation of the system is no

Table 6.1: Comparison between the values obtained by testing and by finite element simulations of some relevant parameters of the model.

	ω_{pk1}	ω_{pk2}	ω_{r1}	ω_{r2}	Γ
FEM	50045	55868	48830	51681	$1.10e^{10}$
Testing	48896	55417	48870	51520	$1.02e^{10}$
Error	2.3%	0.8%	0.1%	0.3%	7.8%

longer appropriate. In order to predict and explain the rich dynamics that the system shows, we have to return to the original equations (6.10).

6.3.2 Parametric Resonance

Ignoring damping and external excitations, (6.10) can be written as

$$\ddot{Z} + [\Delta + \epsilon E \cos(2\omega t)]Z = 0 \quad Z \in \mathbb{R}^{2 \times 1}, \quad (6.15)$$

which can be considered the vector extension of a standard Mathieu equation. In Section 3.3 we have demonstrated that parametric resonance occurs also in systems described by equations of this form. In particular, we have shown that each region of parametric amplification in this case can be composed by multiple tongues. The location of these tongues is determined by the system parameters, and more specifically by the eigenvalues of Δ in (6.15). These eigenvalues coincide with the normal mode frequencies of the system, which are approximately equal to the peaks in the frequency response. Hence, from (3.23) we have that the tongues can emanate from

$$\omega_{pk,i}T = n\pi \quad n \in \mathbb{N},$$

and

$$(\omega_{pk,1} \pm \omega_{pk,2})T = 2n\pi \quad n \in \mathbb{N},$$

with $T = \frac{\pi}{\omega}$ in (6.15), so that in terms of the frequency of excitation we have

$$\omega \approx \frac{\omega_{pk,i}}{n} \quad n \in \mathbb{N}, i = 1, 2$$

and

$$\omega \approx \frac{\omega_{pk,1} \pm \omega_{pk,2}}{2n}. \quad n \in \mathbb{N} \quad (6.16)$$

It is worth noting that also in this case the presence of a damping term has the effect of making the tongues narrower and shifting them upwards, so that there is a critical voltage amplitude above which parametric resonance can be induced [83], but does not affect the stability analysis.

Figure (6.21) shows the experimental mapping of the first region ($n = 1$) for our pair of cantilevers. During these experiments one of the inputs was set to zero, while the other was set to $V_i = \frac{V_o}{2}\sqrt{1 + \cos \omega_o t}$. Which input is selected is in fact inconsequential, given the symmetry of the device, and the results can be reproduced using either one of them. Note that when the input is a square-rooted sinusoid, (3.23) needs to be modified, to give $\omega = 2\omega_{pk,i}/n$ and $\omega = (\omega_{pk,1} \pm \omega_{pk,2})/n$. Figure (6.21 a) and b) shows the cases corresponding to the driving frequency being varied around to a) $2\omega_{pk1}$ and b) $2\omega_{pk2}$. For $n = 1$ we find that the parametric resonance can be induced also by $\omega = \omega_{pk1} + \omega_{pk2}$, which is the case depicted in part c) of the same figure. However, we could not induce parametric amplification for $\omega = \omega_{pk1} - \omega_{pk2}$.

During parametric amplification, the beams exhibit an oscillation that is bounded by the system nonlinearities. For large oscillation amplitudes,

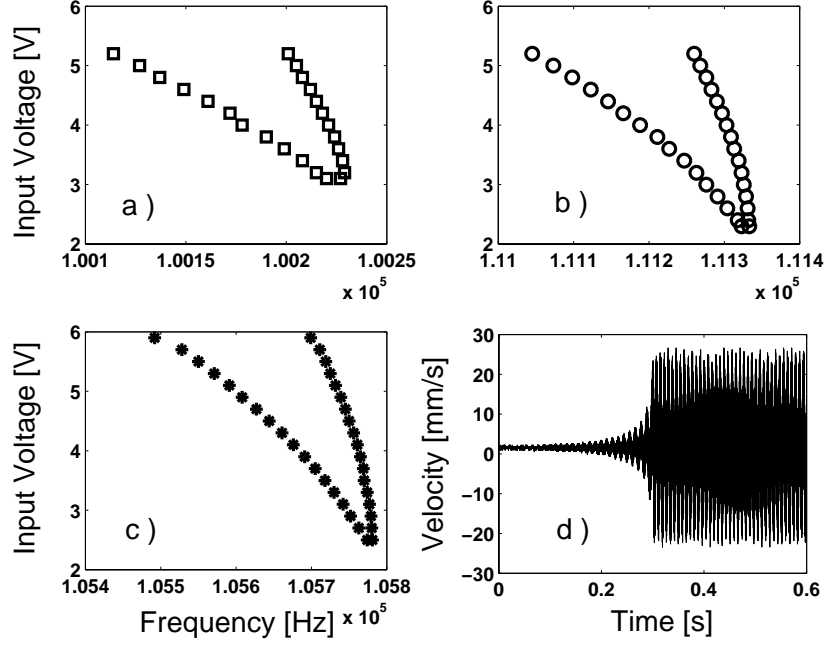


Figure 6.21: First region of coupled parametric amplification, with the electric signal applied to one cantilever only. The three tongues correspond respectively to a) $\omega = 2w_{pk1}$; b) $\omega = 2w_{pk2}$; c) $\omega = w_{pk1} + w_{pk2}$. Picture d) shows the exponential growth of the output inside the region of parametric amplification.

both the linear spring model and the linear electrostatic force need to be corrected by adding cubic terms. Equation (6.10) becomes

$$\ddot{Z} + \nu\dot{Z} + [\Delta + \epsilon E \cos(2\omega t)]Z + A_3 Z^3 = kU,$$

where the matrix A_3 , which is diagonal, describes the effective cubic stiffness of each beam. When driving the cantilever in parametric resonance regime we observe: in case a) and b) a subharmonic 2 : 1 oscillation at half

the frequency of excitation; in case *c*) an oscillation having both frequency components. Also, note that during the transition from non-parametric to parametric region, the response shows a characteristic exponential growth, as expected (see Figure 6.21d)) [83].

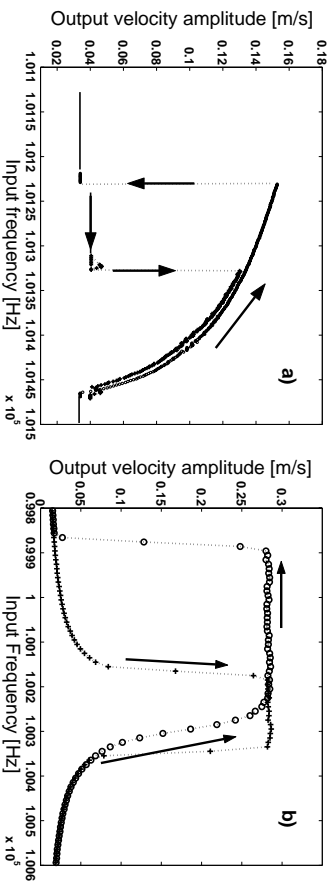


Figure 6.22: Frequency response above critical driving voltage : a) single cantilever b) coupled cantilevers in region a) of Figure(6.21).

Figure (6.22) is a comparison of the frequency response of a cantilever during parametric resonance, in the uncoupled and coupled cases. Part a) refers to an isolated cantilever. Part b) refers to coupled cantilevers and to region a) of Figure (6.21). In both cases, the data collected is the velocity amplitude, as the driving frequency is swept from low to high ('+' points) and from high to low ('o' points). The input applied is a square rooted sinusoidal signal: in the case of two cantilevers, during this experiment one of them was grounded. The data shown in part b) corresponds to only one region and only one of the two cantilevers, because (qualitatively), they show the same behavior, in all three resonant regions. Also, note that the flattening of the oscillation amplitude is due to the cantilever touching the

substrate.

We notice that, when sweeping the frequency from low to high, in both cases, the entrance to the parametric region is marked by a sharp jump in the amplitude of the cantilevers oscillation. This phenomenon was already noticed in Section 6.2 and its relevance in terms of potential engineering applications was mentioned. In the case of two cantilevers one has the additional advantage of having three parametric regions and therefore the option of selecting the frequency range where to work. Moreover, at the design stage of the device, the tongues can be placed as desired by tuning the mechanical coupling coefficient.

Inside the parametric region, as the driving frequency increases, the periodic subharmonic solution is stable and shows decreasing amplitude in case a), and increasing amplitude in case b). We reiterate that the flattening of the output is an experimental artefact, which is due to the fact that the cantilever is touching the substrate. Upon exiting the region, while in case a) the oscillation is reduced to zero, in case b) the periodic solution remains stable and its amplitude virtually keeps increasing, until it goes back to zero. The location of this second jump is not predictable and depends on the amplitude of the frequency increments. If we reverse the process and start decreasing the frequency, the output amplitude starts to increase and keeps increasing, in both cases, even after leaving the parametric region. Again, this large periodic solution eventually collapses to zero at some unpredictable time.

From a dynamical systems point of view, the different behavior in Fig. (6.22) a) and b) corresponds to a different phase portrait. In particular,

while the single cantilever has a bistable region only on the left side of the tongue (where both the periodic and the trivial solutions are stable), the coupled cantilevers have a bistable region on both sides of the tongue. Interestingly, when subject to both harmonic and parametric excitation, that is for instance when excited by a sinusoidal input having a small DC offset, a single cantilever exhibits a behavior similar to what depicted in Fig. (6.22 b). Since the electrostatic force depends on the square of the voltage, this implies that the cantilever is excited both at the driving frequency ω and at 2ω , implying the coexistence of both harmonic (ω) and parametric (2ω) forcing. For the case of two cantilevers, this behavior can be explained intuitively by the following approximate argument. From (6.15) define $x := z_1 + z_2$ and $y := z_1 - z_2$, and consider the case of a square rooted sinusoidal input : the equations of motion are given by:

$$\ddot{x} + (\bar{\omega}_1^2 + \bar{\epsilon}_1 \cos(\omega t))x = -(\Delta\omega + \Delta\epsilon \cos(\omega t))z_2, \quad (6.17)$$

$$\ddot{y} + (\bar{\omega}_2^2 + \bar{\epsilon}_2 \cos(\omega t))y = (\Delta\omega + \Delta\epsilon \cos(\omega t))z_1, \quad (6.18)$$

where $\bar{\omega}_1^2 = \omega_1^2 + \gamma_1$, $\bar{\epsilon}_1 = \epsilon_1 + \gamma_2$, $\bar{\omega}_2^2 = \omega_2^2 - \gamma_1$, $\bar{\epsilon}_2 = \epsilon_2 - \gamma_2$, $\Delta\omega = \omega_2^2 - \omega_1^2$, $\Delta\epsilon = \epsilon_2 - \epsilon_1$. Now, ignoring the right hand sides, (6.17,6.18) represent a pair of uncoupled, standard Mathieu equations. Hence, their parametric regions of the first order are obtained for $\omega = 2\bar{\omega}_1$ and $\omega = 2\bar{\omega}_2$ respectively, which correspond roughly to the peaks of the frequency responses in Fig.(6.17) and to the values obtained by the previous analysis. From the definition of x we can infer that, when excited at $\omega = 2\bar{\omega}_1$, z_1 and z_2 oscillate in phase at $\omega = \bar{\omega}_1$. Hence, z_2 on the RHS of (6.17) acts as a harmonic excitation, justifying the phase portrait observed experimentally. A similar argument can be repeated for (6.18), where z_1 oscillates with

opposite phase from z_2 and provides the harmonic excitation.

*

Chapter 7

Observer Design

In this chapter we address the problem of designing a dynamical system capable of providing an estimate \hat{x} for the cantilevers displacement, based on the measurement of the current through the cantilevers. This approach that we call “indirect” sensing, has the advantage of allowing for compact devices, by removing the usually cumbersome apparatus used in optical sensing techniques [38, 39, 40, 1]. The optimal observer design, formulated and solved in Section 7.1, is used as an analysis tool to tune both the frequency of excitation of the cantilever and the parameters of a reduced order observer (Section 7.2) to obtain the best achievable performance in terms of \mathcal{H}_∞ -norm of the closed loop system.

7.1 Optimal Observer Design

One of the main goals of our research project has been to design an observer to reconstruct the displacement of cantilevers from an indirect mea-

surement. The fact that the system is time-varying has made the problem less straightforward to solve. In this section we illustrate how this problem has been tackled and provide simulation results to demonstrate the performance of the observer.

We have started our analysis by considering a single cantilever. The observer problem in the Linear Fractional Transformation (LFT) framework can be formulated as an \mathcal{H}_∞ filtering problem, by defining the variable $z = x - \hat{x}$ (estimation error), and considering the generalized plant shown in Fig.7.1 and described by

$$G_{gen} := \left[\begin{array}{c|cc} A(t) & B_1 & 0 \\ \hline C_1 & 0 & D_{12} \\ C_2(t) & D_{21} & 0 \end{array} \right] = \left[\begin{array}{c|cc} A(t) & [M \ 0] & 0 \\ \hline I & 0 & -I \\ C(t) & [0 \ N] & 0 \end{array} \right], \quad (7.1)$$

where the exogenous input $w = [d \ n]^T$ represents process and measurement noise, the matrices M and N are respectively the process and measurement noise weight, the matrices $A(t)$, $C(t)$ are as in (5.7) and the input $u = \hat{x}$ is the output of the observer system. Notice that we do not need to account for the signals u_f and v_f in (5.7): since they are known, their presence does not affect the observer design.

In this framework, the optimal observer problem amounts to finding a dynamical system G_{obs} such that the \mathcal{H}_∞ norm of the transfer function T_{zw} from w to z is minimized. If the system is time-invariant, and has the structure of (7.1), where $D_{21}'B_1 = 0$, than the optimal filter is an observer, whose gain L comes from the solution of an appropriate algebraic Riccati equation [95]. It turns out that a similar result holds in the time-varying case as well. The details have been presented in Section 2.1, where the

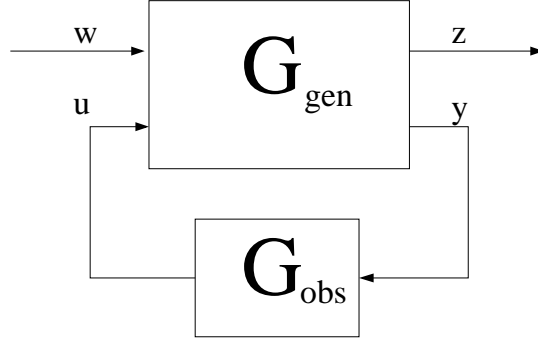


Figure 7.1: A block diagram of the observer problem.

solution for the periodic case is derived from the results of [50]. If the system is periodic, the algebraic Riccati equation is replaced by a periodic differential Riccati equation (2.2), which we recall here

$$\dot{P}(t) = A(t)P(t) + P(t)A(t)' - P(t)[C(t)'C(t) - \frac{1}{\gamma^2}I]P(t) + B(t)B(t)'. \quad (7.2)$$

If the periodic non-negative definite solution of this equation $P(t)$ is stabilizing, the optimal filter has the structure of an observer and is given by

$$\dot{\hat{x}} = A(t)\hat{x} + \mathbf{P}(t)\mathbf{C}(t)'[y(t) - C(t)\hat{x}].$$

While we do not necessarily wish to implement this optimal observer, we propose a method where we use the driving frequency ω_o as a design parameter in (7.2) and tune its value so that the closed loop system has the minimum attainable H_∞ norm. Recall, from the cantilever dynamical equations (5.7), that ω_o enters as a parameter in the expression of A and C . In other words, we propose to use the optimal observer design to actually design the system (rather than the observer), by selecting the excitation

frequency that produces the least estimation error. This procedure requires solving (7.2) for every ω_o and computing the norm of the corresponding closed loop time-varying system. We have followed two approaches.

In the first approach [53], we have applied lifting to (7.1), and have reformulated the optimal observer problem in the lifted domain. As discussed in Section 2.2, by lifting, the periodic system G can be associated with an equivalent time-invariant *infinite dimensional* system \hat{G} . In its turn, by fast-sampling, \hat{G} can be approximated by a shift-invariant *finite dimensional* system \tilde{G} . It is for this latter, almost equivalent problem that the observer problem has been finally explicitly solved. The expressions of the matrices describing \tilde{G} , discrete, shift-invariant and finite dimensional

$$\tilde{G} := \left[\begin{array}{c|cc} \text{F} & G_1 & 0 \\ \hline H_1 & J_{11} & J_{12} \\ H_2 & J_{21} & 0 \end{array} \right],$$

are given in Section 2.2. Standard techniques can be applied to this system, both for solving the observer problem and for computing the closed loop norm. In particular, the lifted observer corresponds to a constant matrix L , whose elements are the Fourier coefficients of the corresponding time varying gain $L(t)$. It was proved in [56] that this approximation converges at the rate of $1/N$, if T/N is the sampling period, and T the period of the system. Hence, by increasing the number of samples per period we can approximate the optimal solutions of the original system to any prescribed degree of accuracy [56].

Figure 7.2 describes the dependence of the closed loop \mathcal{H}_∞ -norm on the frequency of excitation, ω_o . The parameters of the cantilever used in

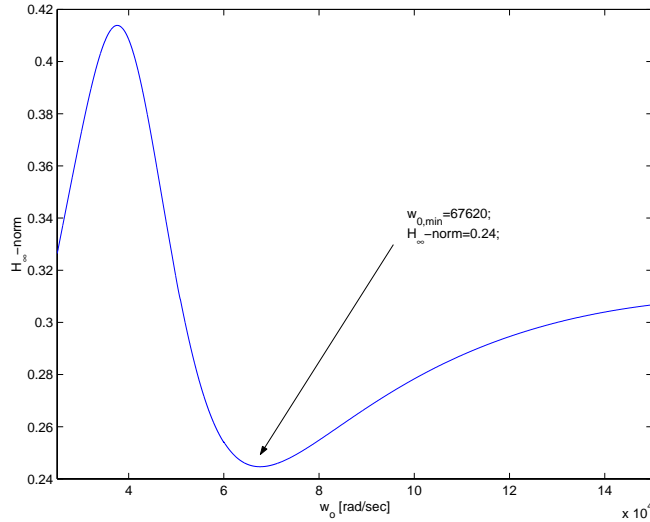


Figure 7.2: \mathcal{H}_∞ –norm vs. frequency of excitation for the lifted, fast sampled system.

this simulation are based on a preliminary design, later revised, and are as follows: length $L = 300\mu m$, width $w = 50\mu m$, thickness $t = 1\mu m$ and gap $d = 10\mu m$.

The second approach we have pursued was based on the observation that by designing the observer in the lifted domain with the procedure outlined above, we had not incorporated a causality constraint, so that the observers corresponding to the data of Fig. 7.2 are both causal and a-causal [96]. The causality constraint, which amounts to imposing that the observer gain L be diagonal, cannot be easily incorporated in the formulation above. Hence, we decided to go back and use directly (7.2) for the observer design.

In this second approach, we have solved numerically the periodic Riccati

equation for each ω_o and for the least admissible γ that corresponds to a stabilizing solution. The difficulty now lies in the fact that this procedure requires knowledge of the initial condition P_o corresponding to the periodic stabilizing solution of (7.2). The method developed to tackle this problem was described in Section 2.1. More precisely, we have defined a map \mathcal{P} (2.2) whose fixed points correspond to the unknown P_o . Whence, the search over the initial conditions is transformed into a fixed point seeking problem, which is solved via an iterative scheme using the secant method.

Figure 7.3 describes the dependence of the closed loop norm from the frequency of excitation, ω_o . The parameters of the cantilever used in this analysis are those obtained by system identification and are given in Section 6.2. In particular, for the length we have used its effective value. Notice that the minimum is reached at different values of the driving frequency, depending on the measurement noise weight N and not necessarily coinciding with the resonance frequency. We note that the analysis here is done solely for the optimal observer design problem. In any realistic application of micro-cantilevers, there will be other control objectives as well. The problem setup, then, would involve a compound cost function that involves both observations and control. For such a problem, the best driving frequency will probably be different than the one obtained here, and its value will depend on the particular tradeoffs between control and estimation. The framework we present here should be easily extended to incorporate control objectives as well.

As a second step we have turned our attention to the case of pairs of coupled cantilevers. Under the assumption that the inputs applied are the

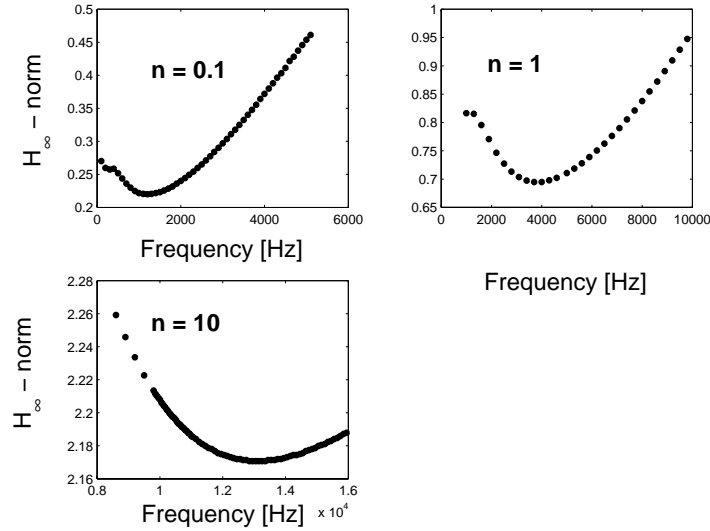


Figure 7.3: H_∞ -norm vs. frequency of excitation with a causal observer.

same, we can apply the procedure outlined above to the periodic system comprising both cantilevers. The state space has dimension four in this case, and so has $P(t)$ in the Riccati equation (7.2), but there is no conceptual difference in treating this case from the previous one. The difficulty arises when the inputs have different, non commensurate frequencies. In this case the coupled equations are not even periodic, making the design of the observer for the coupled system much harder.

In Fig. 7.4 we show a block diagram of the observer structure that we propose for the cantilever pair. In this configuration, the subsystems corresponding to the observers are designed for each cantilever as if they were decoupled, i.e. treating the coupling variables z_j in the linearized

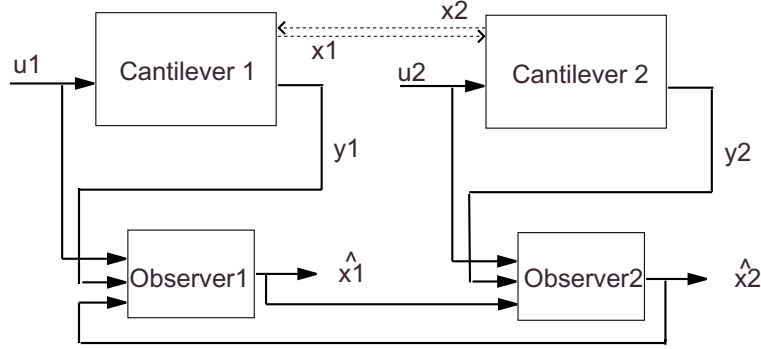


Figure 7.4: A schematic of the observer. The dashed lines represent the coupling interaction.

model as if they were exogenous inputs

$$\ddot{z}_i + \nu_i \dot{z}_i + \omega_i^2 z_i = b_1 V_i^2 - \gamma_1 z_j, \quad (7.3)$$

where γ_1 accounts for both mechanical and electrostatic coupling. In this fashion, not only can we recast the problem in the framework of periodic systems theory, but also we gain flexibility. In fact, now the design does not depend on the number of units (cantilevers) considered and can be easily extended to the case of an array of microcantilevers, which will be discussed later in this section.

The observers in Fig. 7.4 are designed following the procedure outlined above for a single cantilever. Note that, in this “decoupled” design the optimal observers do not necessarily guarantee stable error dynamics for the overall system. In fact, from Theorem 2.2, Section 2.1 the solution $P_i(t)$ to each Riccati equation guarantees that $[A_i - P_i(t)C_i'(t)C_i(t)]$ is stable. However, if we denote by e_1, e_2 the estimation errors on the state

variables of the first and second cantilever respectively, in the absence of noise their dynamics are now described by the following equations

$$\begin{aligned} \dot{e}_1 &= [A_1 - P_1(t)C_1'(t)C_1(t)]e_1 + G_c e_2, \\ \dot{e}_2 &= G_c e_1 + [A_2 - P_2(t)C_2'(t)C_2(t)]e_2, \end{aligned} \quad (7.4)$$

that is they are coupled, with $G_c = \begin{bmatrix} 0 & 0 \\ \gamma_1 & 0 \end{bmatrix}$. Using the small gain theorem, we can establish the stability of (7.4) if we can guarantee that the I/O norm of the two error subsystems Σ_i is small enough, $\|\Sigma_1\| \|\Sigma_2\| < 1$. This condition can be included in a compound optimal objective. To this end we introduce the augmented state variable $\bar{x}_i := [x_i, \hat{x}_i]^T \in \mathbb{R}^4$ and consider the closed loop system

$$\begin{aligned} \begin{bmatrix} \dot{x}_i \\ \dot{\hat{x}}_i \end{bmatrix} &= \begin{bmatrix} A_i & 0 \\ L(t)C_i & A_i - L(t)C_i \end{bmatrix} \begin{bmatrix} x_i \\ \hat{x}_i \end{bmatrix} \\ &+ \begin{bmatrix} \frac{B_1}{\gamma} & 0 \\ \frac{B_1 - L(t)D_{21}}{\gamma} & -G_c \end{bmatrix} \underbrace{\begin{bmatrix} w_i \\ e_j \end{bmatrix}}_{\mathbf{w}} + \begin{bmatrix} G_c \\ G_c \end{bmatrix} \underbrace{x_j}_{\mathbf{u}}, \end{aligned} \quad (7.5)$$

$$z_i = [I \quad -I] \begin{bmatrix} x_i \\ \hat{x}_i \end{bmatrix}, \quad (7.6)$$

where B_1, D_{21} are as defined in (7.1). In this formulation, the coupling between x_i and x_j is treated as an external “known” input \mathbf{u} for the cantilever dynamics, while the estimation error e_j is treated as a disturbance. The problem now can be formulated as that of finding the periodic matrix $L(t)$ that makes $\|T_{\mathbf{w},z_i}\| < 1$. This condition guarantees $\|T_{w_i,z_i}\| < 1$, which corresponds to the old filtering problem, with γ now included in the state matrices. At the same time, it also guarantees the condition $\|T_{e_j,z}\| < 1$,

and so the stability of the error dynamics.

Simulations have been performed to assess the performance loss, if any, caused by this choice of “decoupled” design. In these simulations the cantilevers are assumed to be equal, with a natural resonant frequency of $\omega_{rn} = 51\text{kHz}$, and damping $\xi = 2e^{-3}$, one order of magnitude larger than its experimental value, to guarantee a faster convergence. The driving inputs are sinusoids of equal frequency, with a DC term added to reproduce the most general case, $u_i(t) = V_{DCi} + V_{ACi} \cos \omega t$. The solution to the full order Riccati equation, when the two cantilevers are considered as one system, is denoted by P_4 . The solutions to the single Riccati equations for the respective cantilevers are denoted by P_1 , and P_2 . Figure 7.5 compares the performance of the two observer schemes. In this simulation the input parameters are set to: $V_{ac1} = 10 \text{ mV}$, $V_{ac2} = 50 \text{ mV}$, $V_{dc1} = 200 \text{ mV}$, $V_{dc2} = 100 \text{ mV}$, $f_1 = f_2 = 50.5 \text{ kHz}$. Note how, even during the transient, the behavior of the two schemes is not appreciably different. Figure 7.6 demonstrates that, at steady-state, they both achieve practically exact state estimation.

In other words, there is no appreciable loss in performance in adopting the decoupled design over the full order one. In order to understand this result, which is indeed surprising at first glance, we have looked at the structure of the observers obtained with the two different design schemes. In the “decoupled” design, the equations of the overall observer subsystem

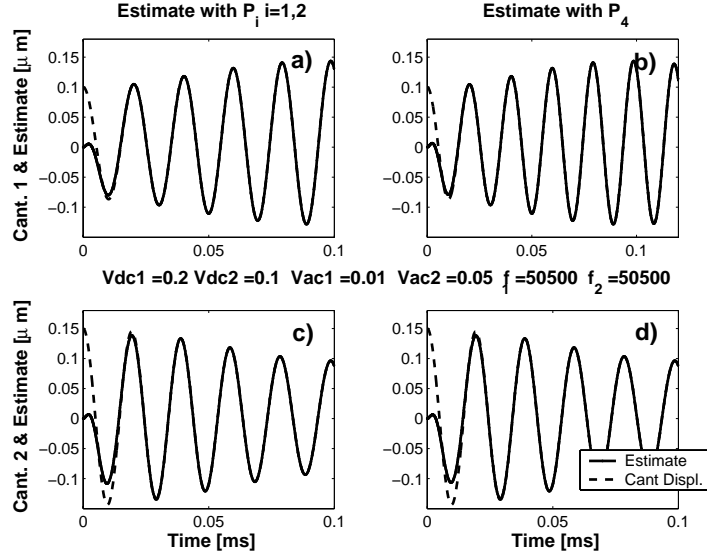


Figure 7.5: Comparison of the performance of the observers defined by P_4 (part b,d) and P_i , $i = 1, 2$ (part a,c) during transient. The plots in a,b refer to cantilever 1, the plots c,d) to cantilever 2. Notice how the transient of the two observer schemes is not significantly different.

are given by

$$\begin{aligned}
 \begin{bmatrix} \dot{\hat{x}}_1 \\ \dot{\hat{x}}_2 \end{bmatrix} &= \begin{bmatrix} A_1 & G_c \\ G_c & A_2 \end{bmatrix} \begin{bmatrix} \hat{x}_1 \\ \hat{x}_2 \end{bmatrix} + \\
 \begin{bmatrix} P_1(t) & 0 \\ 0 & P_2(t) \end{bmatrix} \begin{bmatrix} C'_1(t) & 0 \\ 0 & C'_2(t) \end{bmatrix} &\left\{ \begin{bmatrix} y_1 \\ y_2 \end{bmatrix} - \begin{bmatrix} C_1(t) & 0 \\ 0 & C_2(t) \end{bmatrix} \begin{bmatrix} \hat{x}_1 \\ \hat{x}_2 \end{bmatrix} \right\}.
 \end{aligned} \tag{7.7}$$

The structure of this equation suggests that this design corresponds to the special case of a diagonal P_4 . Whence, if we partition P_4 in four 2×2

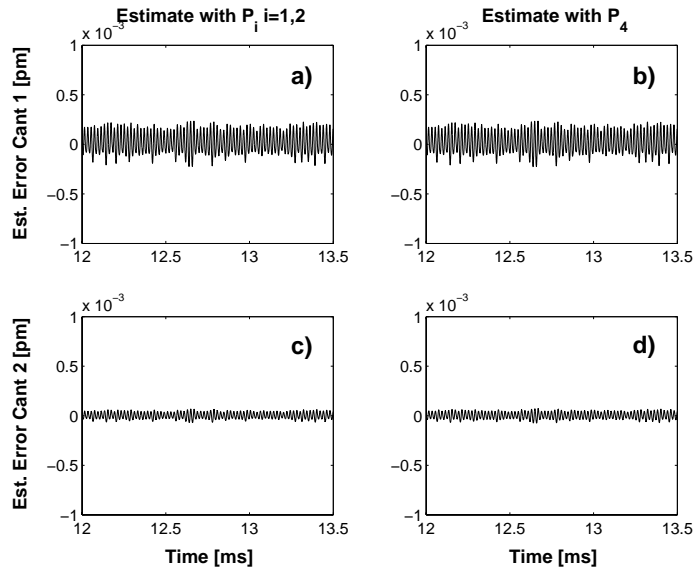


Figure 7.6: Estimation error at steady state. Parts a,b) refer to cantilever 1, parts c,d) to cantilever 2. Note that the vertical scale is in pm.

blocks

$$P_4 = \begin{bmatrix} \mathbf{P}_{11} & \mathbf{P}_{12} \\ \mathbf{P}_{21} & \mathbf{P}_{22} \end{bmatrix},$$

we can identify corresponding blocks in the two designs and compare them to explain the simulations. It turns out, as shown in Fig. 7.7, that there is an extremely small discrepancy between P_i , $i = 1, 2$, and the corresponding blocks \mathbf{P}_{ii} of P_4 . Furthermore, the elements of the extra diagonal blocks $\mathbf{P}_{i,j}$ of P_4 are in comparison very small, as shown in Fig. 7.8. An intuitive explanation of why this might be the case can be sought in the structure of the matrices in (7.2), when the Riccati equation is rewritten for the full order system. In this case all the system matrices but the state matrix A

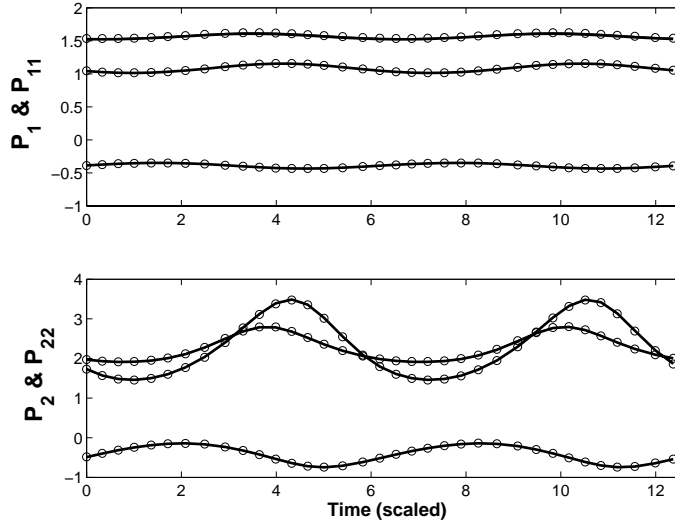


Figure 7.7: Comparison between the components of P_i , $i = 1, 2$ (solid lines) and the corresponding elements of the diagonal blocks \mathbf{P}_{ii} , $i = 1, 2$ of P_4 (circles).

are diagonal. A itself has an almost diagonal structure

$$A = \begin{bmatrix} A_1 & G_c \\ G_c & A_2 \end{bmatrix} = \begin{bmatrix} A_1 & \begin{bmatrix} 0 & 0 \\ \gamma_1 & 0 \end{bmatrix} \\ \begin{bmatrix} 0 & 0 \\ \gamma_1 & 0 \end{bmatrix} & A_2 \end{bmatrix},$$

where A_i are the state matrices for the single cantilevers, and G_c models the coupling. If we scale the equation by the value of the resonant frequency, γ_1 turns out to be also relatively small. Whence the almost decoupled structure of P_4 .

To conclude this section, we consider the problem of the multicantilever array. If we assume that all the cantilevers are identical and the inputs applied are the same, the whole structure can be treated as a distributed

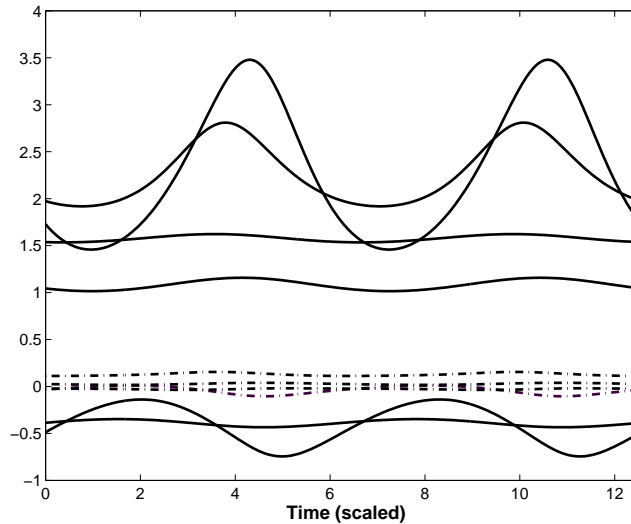


Figure 7.8: Components of P_4 . The solid lines represent the components that P_4 has in common with P_1, P_2 , also shown in Figure 7.7. The dashed lines are the components of P_4 belonging to the extra diagonal blocks \mathbf{P}_{12} and \mathbf{P}_{21} .

spatially-invariant time-periodic system. As illustrated in Section 2.3, this implies that, in order to study the multicantilever, we do not need to deal with the infinite dimensional model corresponding to the complete array. We can use instead the parameterized finite dimensional model obtained by applying the spatial Fourier transform

$$\ddot{z}(t, \theta) + c\dot{z}(t, \theta) + \hat{a}(\theta)z = u(t, \theta), \quad (7.8)$$

where $\hat{a}(\theta) = a - \sum_{m \neq n} (\Gamma_{n,m} + a_{n,m})e^{-i\theta m}$ contains all the coupling terms. For more details on the notation we refer the reader to Section 2.3. The optimal observer problem for this model can be solved analogously to what

we presented above for the single cantilever case . Equation (7.2) is now replaced by a parameterized periodic Riccati equation

$$\begin{aligned} \dot{P}(t, \theta) = & A(t, \theta)P(t, \theta) + P(t, \theta)A(t, \theta)' & (7.9) \\ & -P(t, \theta)[C(t, \theta)'C(t, \theta) - \frac{1}{\gamma^2}I]P(t, \theta) + B(t, \theta)B(t, \theta)', \end{aligned}$$

and the observer itself will be a distributed system. A schematic of its architecture is shown in Figure 7.9, which shows the coupling between the n^{th} observer unit and the neighboring units. In general, the $P(t, \theta)$ that solves (7.9) will be an irrational function of θ . This means that the observer needs to receive information from distant units in the array to provide an estimate at each given point. Given the number of cantilevers involved in the coupling interaction, the strength of this coupling depends on the analytic properties of $P(t, \theta)$. If its Laurent expansion coefficients decay to zero fast enough, it is reasonable to expect that a satisfactory suboptimal observer, dealing only with “local” information, can be achieved by truncating the infinite series expansion. In fact, from the insight gained from the study of the two cantilevers case we expect this decay rate to be indeed quite fast.

Besides this strategy, as outlined in the two cantilevers case, the alternative is to design an optimal observer for each cantilever as if it were isolated, treating coupling as another external excitation. The advantage deriving from this approach is twofold. First of all, it allows us to treat the case where the input signals are not at the same frequency. Second, the cantilevers can be different, which is not allowed in the previous design, since in this case the system would not fall in the category of spatially-invariant distributed systems. The drawback is that we are not guaranteed

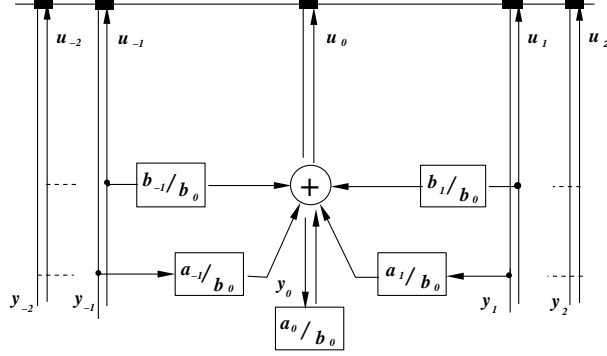


Figure 7.9: Schematic of the distributed observer.

stable error dynamics, similarly to what happened in the two cantilevers case. In the following derivation, we consider the case of nearest neighbor interaction. The estimation error for each cantilever in this case is given by

$$\dot{e}_i = [A_i(t) - P_i(t)C_i'(t)C_i(t)]e_i + G_c e_{i-1} + G_c e_{i+1} = A_{e_i}(t)e_i + G_c e_{i-1} + G_c e_{i+1},$$

where G_c is the coupling matrix that has been defined previously. We define the global estimation error variable \mathcal{E} as the collection of these vectors

$$\mathcal{E} = \begin{bmatrix} \vdots \\ e_{-1} \\ e_0 \\ e_1 \\ \vdots \end{bmatrix}.$$

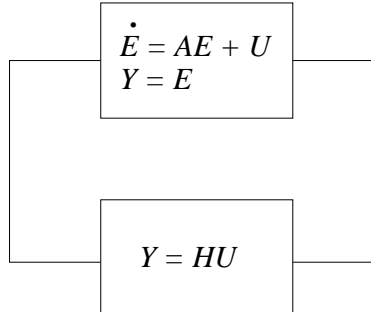


Figure 7.10: Schematic representation of the small gain theorem for the infinite dimensional array.

The other system is diagonal. Its norm is the sup over all norms of the decoupled subsystems. Even though the parameters of these subsystems might be different, their value will be very close. Hence it will be possible to find an upper bound η to their norms. The error dynamics will be stable if $\eta < \frac{1}{2\gamma_1}$.

7.2 The Reduced Order Observer

In this section we consider the problem of designing a reduced order observer. In particular, we are interested in defining a procedure to tune its parameters, so that it is a sub optimal implementation of the \mathcal{H}_∞ optimal observer derived in the previous section.

A reduced order observer allows us to exploit the information about the state of the system that is provided by the output signal and leave to the observer the task of estimating a smaller portion of the state vector.

The details of this standard technique can be found in any book on linear systems theory, and for instance in [86]. Its synthesis is based on the definition of an appropriate change of coordinates, such that in the new coordinates the output of the system becomes a state variable. The matrix that defines such coordinate transformation is time varying in this case, and is given by

$$T^{-1} = \begin{bmatrix} H(t) \\ C(t) \end{bmatrix} = \begin{bmatrix} c_2^{-1} \cos \omega_o t & -c_1^{-1} \sin \omega_o t \\ c_1 \sin \omega_o t & c_2 \cos \omega_o t \end{bmatrix},$$

where c_i , $i = 1, 2$ are the constant coefficients of $c_i(t)$ in (5.7), $T^{-1} \in \mathbf{C}^1$ and $\det(T^{-1}) = 1$ at each t . Notice that to be well-defined, this change of coordinates requires consideration of a “noiseless” output, i.e. $\tilde{y} = C(t)x$, in contrast to the formulation of the optimal observer problem (7.1). It will become clear later, when we analyze the simulation results, how this assumption influences the performance of the two observers.

After few algebraic steps the equations of the observer turn out to be

$$\begin{aligned} \dot{\hat{v}} &= (A_{11}(t) + L(t)A_{21}(t))\hat{v} + M(t)y \\ \hat{z} &= T(t) \begin{bmatrix} \hat{v} - L(t)y \\ y \end{bmatrix}, \end{aligned} \tag{7.11}$$

where A_{11} , A_{21} , M are T -periodic functions that can be computed from the system matrices in (5.7). In particular,

$$A_{11} = d_o + d_1 \sin 2t + d_2 \sin 4t + d_3 \cos 2t \tag{7.12}$$

$$A_{21} = d_4 + d_5 \cos 2t + d_6 \cos 4t + d_7 \sin 2t, \tag{7.13}$$

with

$$\begin{aligned}
d_0 &= -d_3 = \frac{c}{2}, \\
d_1 &= -\frac{1}{2} \left(\frac{c_1}{c_2} - \frac{c_2}{c_1} a \right), \\
d_2 &= -\frac{1}{2} \frac{c_2}{c_1} q, \\
d_4 &= \frac{1}{2} (-ac_2^2 - c_1^2 + 2c_1c_2 + qc_2^2), \\
d_5 &= \left(qc_2^2 + \frac{1}{2}(-ac_2^2 + c_1^2) \right), \\
d_6 &= \frac{qc_2^2}{2}, \\
d_7 &= \frac{1}{2} c_1 c_2 c,
\end{aligned} \tag{7.14}$$

where all the parameters have been defined in (5.7). $M(t)$ turns out to be given by the expression

$$M(t) := A_{12} - L(t)A_{22} + L(t)(A_{11} + L(t)A_{21}) - \dot{L}(t),$$

where

$$A_{12} = d_8 + d_9 \cos 2t + d_{10} \cos 4t + d_{11} \sin 2t, \tag{7.15}$$

$$A_{22} = d_{12} + d_{13} \cos 2t + d_{14} \sin 2t. \tag{7.16}$$

with

$$\begin{aligned}
d_8 &= \frac{1}{2} \left(\frac{1}{c_2^2} - \frac{c_2}{c_1} a + \frac{q}{2c_1^2} - \frac{2}{c_1c_2} \right), \\
d_9 &= \frac{1}{2} \left(-\frac{2q}{c_1^2} + \frac{1}{c_2^2} - \frac{a}{c_1^2} \right), \\
d_{10} &= \frac{q}{2c_1^2}, \\
d_{11} &= \frac{c}{2c_1c_2}, \\
d_{12} &= -\frac{c}{2}, \\
d_{13} &= \left(2\frac{c_2}{c_1}q - \frac{c}{2} \right), \\
d_{14} &= \frac{1}{2} \left(\frac{c_1}{c_2} - \frac{c_2}{c_1} a \right).
\end{aligned} \tag{7.17}$$

$L(t)$ in (7.11) is the design parameter, through which we can adjust the behavior of the observer.

The state estimation error, $e_z := z - \hat{z}$ is described by

$$e_z = T \begin{bmatrix} e_v \\ 0 \end{bmatrix} + D_z(t)w, \quad (7.18)$$

with $D_z = n \begin{bmatrix} 0 & 0 & c_2 L(t) \cos t - \frac{1}{c_1} \sin t \\ 0 & 0 & -c_1 L(t) \sin t - \frac{1}{c_2} \cos t \end{bmatrix}$ and n sensor noise weight.

Here e_v is governed by the equation

$$\dot{e}_v = (A_{11}(t) + L(t)A_{21}(t))e_v + B_v(t)w, \quad (7.19)$$

with $B_v = m[\frac{\cos t}{c_2} - L(t) \sin t \quad - \frac{\sin t}{c_1} - c_2 L(t) \cos t \quad - nM(t)]$, m system noise weight, n sensor noise weight and M defined above.

$L(t)$ needs to be chosen so that (7.19) is asymptotically stable. As pointed out in Section 3.2, for a T -periodic system this is equivalent to say that the characteristic multipliers are in norm less than 1, $|\lambda(\Phi(T))| < 1$. Since we are dealing with a scalar system, $\Phi(T)$ can be easily computed

$$\Phi(T) = e^{\int_0^T (A_{11} + LA_{21})(\sigma) d\sigma}, \quad (7.20)$$

and the condition on the characteristic multipliers is equivalent to the condition $\int_0^T (A_{11} + LA_{21})(\sigma) d\sigma < 0$. In particular, from the analytical expression of the integrand

$$\begin{aligned} A_{11} + L(t)A_{21} &= d_o + d_1 \sin 2t + d_2 \sin 4t + d_3 \cos 2t \\ &+ L(t) [d_4 + d_5 \cos 2t + d_6 \cos 4t + d_7 \sin 2t], \end{aligned} \quad (7.21)$$

it can be seen that the condition on the characteristic multipliers can be satisfied also by a static gain, ($L = L_o < -d_o$).

Figure 7.11 compares the performance of such a static reduced order observer to the optimal observer described in the previous section ($L = P(t)C(t)'$). Figure 7.12 shows the components of $P(t)$, obtained as a solution to (7.2) for $\gamma = 10$.

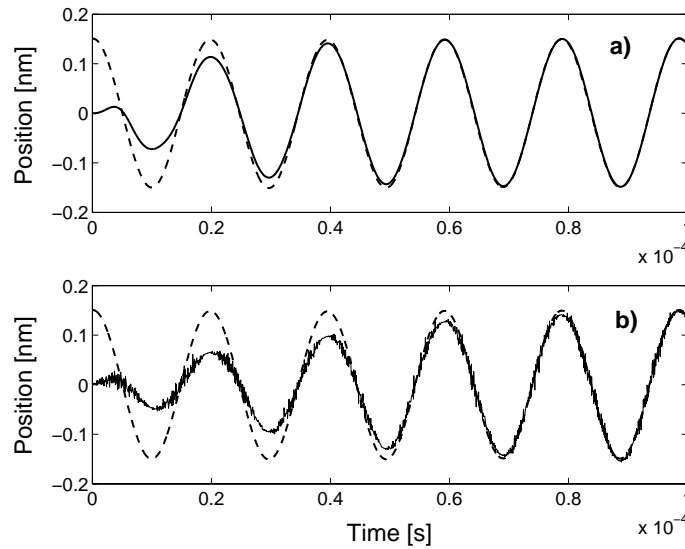


Figure 7.11: Performance of the observers in the presence of measurement noise and initial estimation error. The dashed line is the measured position signal, the solid line its estimate. a) Optimal observer b) Reduced order observer.

At this moment the implementation of the circuit to measure the current is still under study. Therefore we have generated the current signal starting from the experimentally measured velocity and position, using the

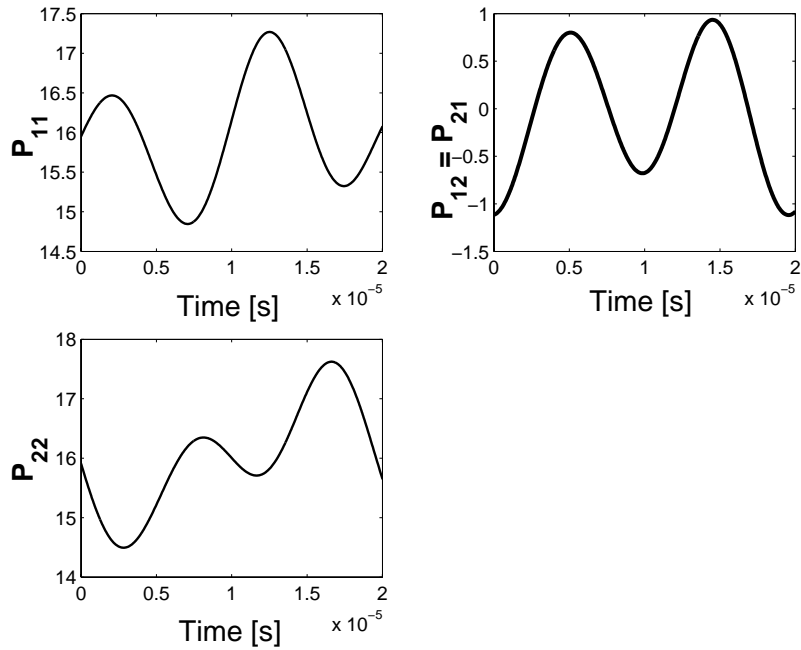


Figure 7.12: Components of $P(t)$.

nonlinear model $i(t) = d/dt[C(x,t)V(t)]$, where $C(x,t)$ is the capacitance (5.1), and $V(t)$ is the input voltage. Gaussian noise, corresponding to a S/N of approximately 12.5, has been added to mimic a real measurement, with the result shown in Fig.7.13.

As can be seen in Figure 7.11, the estimate of both observers converges quite fast to the measured displacement signal: only four cycles for the optimal observer and six for the reduced order observer. However, the latter is affected more heavily by the presence of noise, as expected. The price to pay for its simpler dynamics is a degradation of its performance.

For this reason we want to consider a time-varying observer gain, $L(t) =$

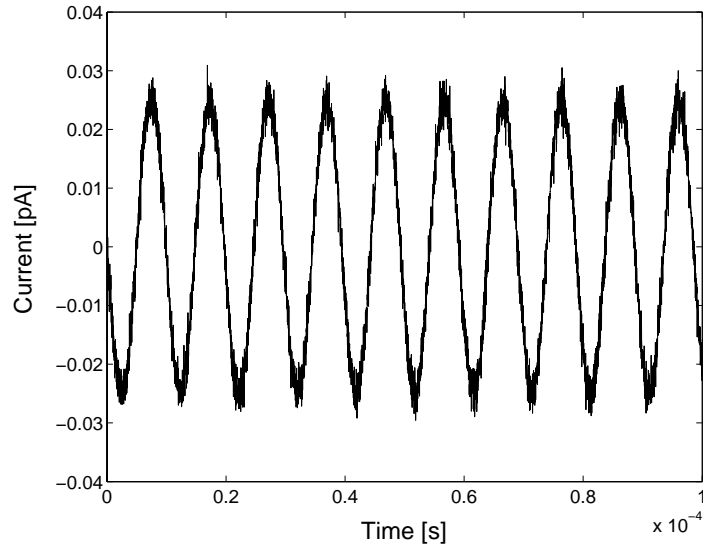


Figure 7.13: Expected current signal from experimental velocity and position data.

$k \cos(\alpha t + \phi)$. This way its parameters can be selected not only to ensure stable error dynamics, but also to optimize its performance, with the \mathcal{H}_∞ -norm as its measure. In particular, from (7.21) it can be seen that the stability condition is met for $\alpha = 2$ and by taking $d_o + kd_5 \cos \phi < 0$, where d_o and d_5 have been defined in (7.14). In fact, if $\alpha = 1$ the system has period $T = 2\pi$ and integration of (7.21) over one period gives a characteristic multiplier $\mu = d_o > 0$. For the computation of the \mathcal{H}_∞ -norm of the closed-loop periodic system, as our closed loop system is, we have used lifting and fast-sampling [55, 56]. Figure (7.14) depicts the value of the closed loop norm as k and ϕ vary in \mathbb{R} and $[0 \ 2\pi)$ respectively. Based on this plot, a better informed choice of k and ϕ turns out to be $k = 0.001$ and $\phi = 3.63$,

which give \mathcal{H}_∞ -norm=45.

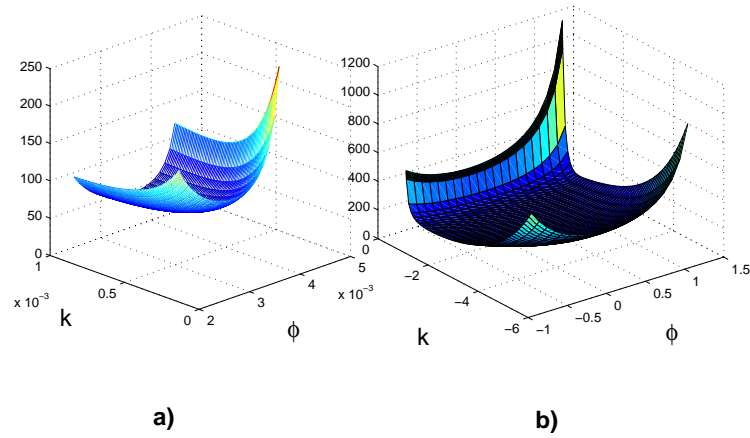


Figure 7.14: Estimation error for different values of the observer gain: a) $k > 0 \cos(\phi) < 0$, b) $k < 0 \cos(\phi) > 0$.

The above procedure can be generalized to any number of cantilevers, where the parameters of each suboptimal observer are tuned independently, according to the architecture chosen for the optimal observer.

*

Chapter 8

Control Design

In order to increase the throughput of a multi probe device, it is desirable to have the largest number of probes in the smallest possible space. On the other side, the proximity of the probes induces coupling in their dynamics, which increases the complexity of the overall device and can deteriorate its performance. For these reasons, multi probe devices are currently designed with large spacings between the individual elements [11, 29, 97, 23, 24, 9, 19]. In this chapter we illustrate the concept of “electronic decoupling” through two case studies, where by means of a distributed controller we are able to achieve decoupled dynamics in tightly packed arrays of individually actuated microcantilevers.

The devices we consider are different. In Section 8.1 we refer to the electrostatically actuated array analyzed throughout the thesis. For this system, we design a decoupling controller, based on the displacement estimate provided by the observer in Section 7. Simulation results are provided to show the effectiveness of the controller. The array considered in Section

8.2 corresponds to a preliminary design for the array (Fig. 1.2), where the actuation was not electrostatic. For this system, we formulate and solve the optimal \mathcal{H}_2 control problem and discuss the synthesis of suboptimal controllers. In particular, with this example we intend to investigate the architecture of a distributed controller in terms of the information it needs to collect from neighboring units to achieve a desired performance.

Both examples demonstrate the ability of control to effectively decouple the dynamics of coupled cantilevers, so that they behave as isolated units in spite of the existing physical coupling.

8.1 Decoupling Controller for Arrays of Electrostatically Actuated Cantilevers

In this section we design a decoupling controller for the electrostatically actuated array described in the previous chapters, and demonstrate that physical coupling can be removed by using an appropriate control action. Indeed if we consider the two cantilevers system, from Equation (7.3) it is clear that we would be able to cancel out the effects of coupling if we could generate an input signal of the form

$$V_i(t) = \sqrt{V_{DC} + V_{AC} \cos(\omega_i t) + \frac{\gamma_1}{b_1} z_j},$$

where the DC offset needs to be large enough so that V_i is always well defined. Note that this does not represent an unfeasible constraint since, in the linear regime of operation, both z_j and V_{AC} are small. However, the problem with this choice of input is that it requires the direct measurement

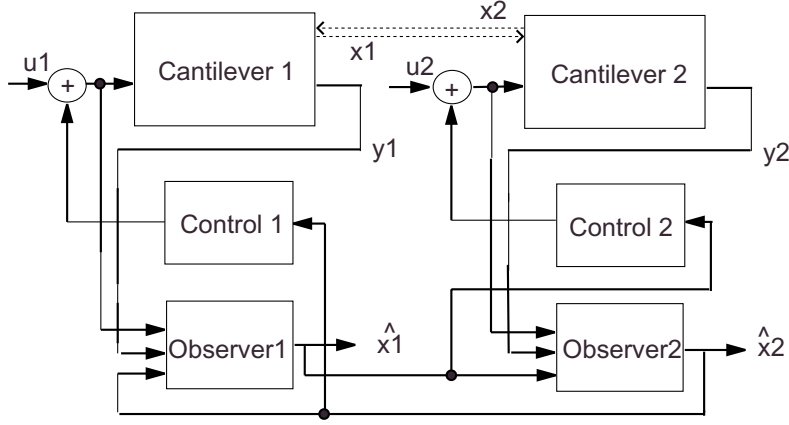


Figure 8.1: Schematic of the observer based decoupling controller. The dashed lines represent internal coupling.

of z_j , which is something we want to avoid.

The control architecture that we propose is represented schematically in Fig.8.1. Here the i -th controller uses an estimate of the displacement of the j -th cantilever, \hat{z}_j produced by the corresponding observer. The input signal, is then given by

$$V_i(t) = \sqrt{V_{DC} + V_{AC} \cos(\omega_i t) + \frac{\gamma_1}{b_1} \hat{z}_j}.$$

Notice that, given the dependence of the current from the input, this choice of control signal represents a problem for the synthesis of the optimal observer gain. In fact, it requires a priori knowledge of \hat{z}_j . However, by considering that in the linear regime of operation of the device, this signal is much smaller than V_{DC} and V_{AC} , we can neglect it in the computation of $P(t)$, without compromising the performance of the observer, as will be shown in the sequel.

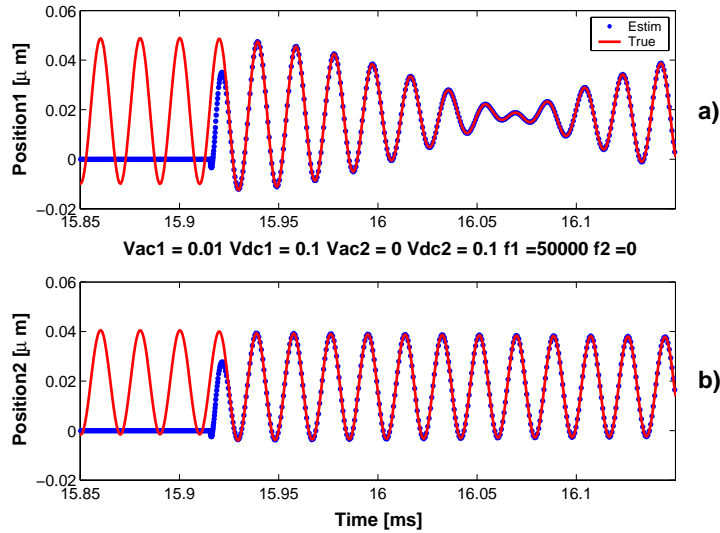


Figure 8.2: Steady state oscillation of Cantilever 1 (a) and Cantilever 2 (b) with detail of the transient when the controller is switched on. The solid line is the cantilever oscillation, the dotted line its estimate. Notice the fast transient of the observer.

Figure 8.2 shows the result of a simulation where one of the cantilevers (Cantilever 1) is excited close to its resonance frequency ($V_{DC}=.1V$, $V_{AC}=10mV$, $f_1=50kHz$), while the other has a constant input ($V_{DC}=.1V$). In particular, we show the instant when the observer/controller is switched on. Notice how prior to this time, as a consequence of coupling, both cantilevers are oscillating (at the same frequency).

Figure 8.3 shows the transient of the controller. In spite of the very fast response of the observer, whose estimation error goes to zero almost instantaneously, the time constant of the controller is much longer. This is due to the fact that, after removing the coupling, the evolution of each

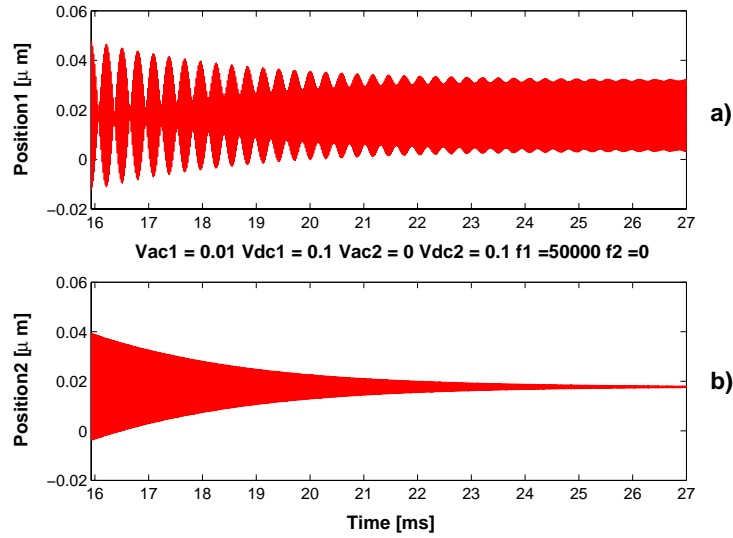


Figure 8.3: Oscillation of Cantilever 1 (**a**) and Cantilever 2 (**b**) after the controller is switched on, showing the controller transient. This longer transient is dominated by the system’s time constant.

cantilever is dictated by its own time constant, and because of its very lightly damped modes, it takes some time to reach steady state.

Figure 8.4 is a comparison of the steady state oscillation of the now decoupled cantilevers, with the oscillation that isolated (uncoupled) identical cantilevers would exhibit if excited by the same input. Notice the excellent performance of the decoupling controller, confirmed also in Fig. 8.5, which shows the decoupling error, defined as the difference between the displacements of the corresponding coupled, $x_{i,coup}$ and uncoupled, $x_{i,uncoup}$ cantilevers, $e_{i,dec} := x_{i,coup} - x_{i,uncoup}$. At steady state this error amounts only to few pm.

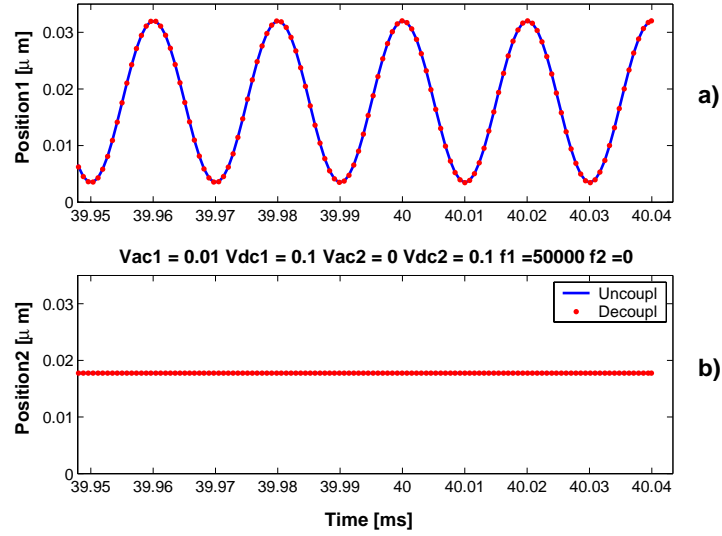


Figure 8.4: Comparison between the decoupled cantilevers oscillation and identical single (uncoupled) cantilevers subject to the same external inputs : **a)** Cantilever 1, **b)** Cantilever 2. The solid line represents the decoupled cantilevers oscillation, the dotted line the uncoupled cantilevers oscillation.

Simulations were performed also to check the effect of measurement noise on the performance of the decoupling controller. Keeping all other parameters unchanged, noise has been added to the output signal, as shown in Fig.8.6. Figure 8.7 compares the oscillations of the coupled cantilever pair, decoupled by the controller action, and the oscillation of single uncoupled cantilevers subject to the same input. Figure 8.8 represents the decoupling error. Compared to the noiseless case, the performance of the decoupling controller is certainly degraded, but remains satisfactory, with a decoupling error in the order of few nm.

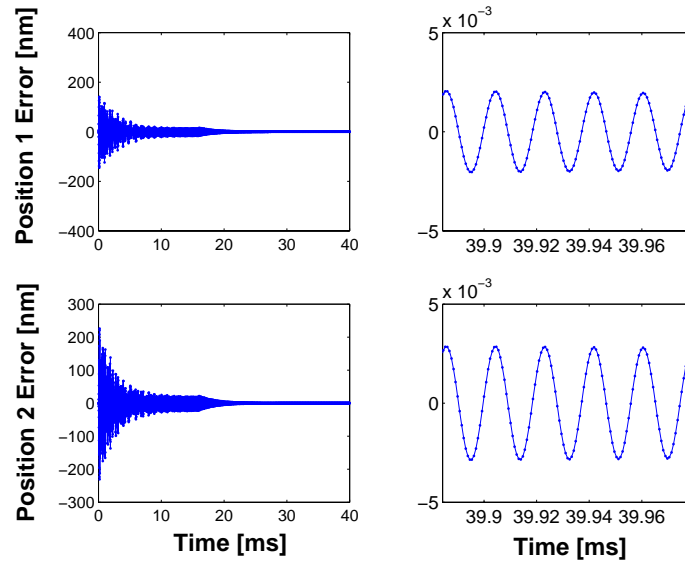


Figure 8.5: Decoupling error (entire trajectory and detail). Note that the scale is nm.

Finally, we have evaluated the performance loss caused by using a reduced order observer instead of an optimal one. The simulation parameters are the same as in the previous simulations. Figure 8.9 compares the oscillations of the coupled cantilever pair, decoupled by the controller action, and the oscillation of single uncoupled cantilevers subject to the same input. Figure 8.10 represents the decoupling error. There is evidence that the persistence of the error, that does not decay to zero even at steady state, is a numerical problem. In fact, by decreasing the integration step, its value becomes smaller (notice that in the figure it is in the order of 10^{-9}).

Even though the performance of the control scheme has been tested

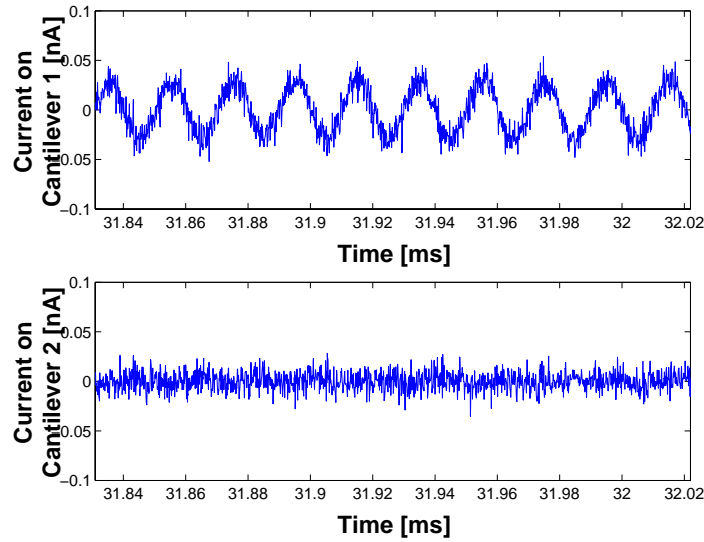


Figure 8.6: Simulation of sensor noise: current on both cantilevers.

only in the case of two cantilevers, the methodology proposed here lends itself to an easy extension to the case of arrays of probes. The overall controller is given by the repetition of (almost) identical units, that have the same coupling structure as the underlying system. Once the cantilevers are decoupled, one could think of designing an appropriate *local* control action to achieve the desired performance objectives, which will depend on the particular application considered.

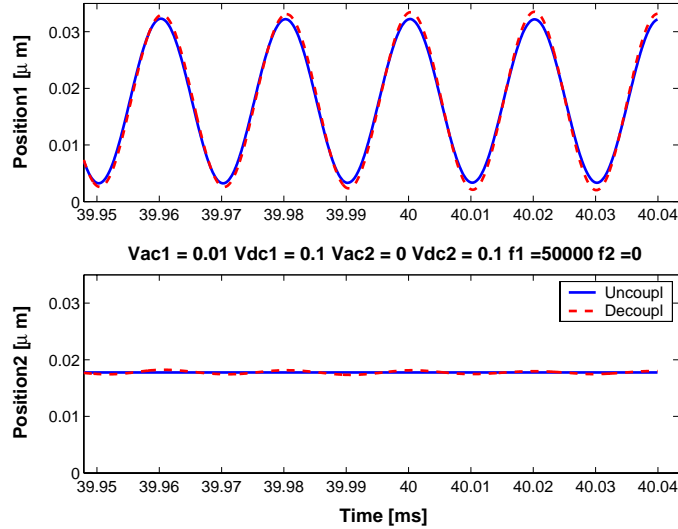


Figure 8.7: Comparison between decoupled and uncoupled oscillation of same cantilevers in the presence of measurement noise.

8.2 Optimal Control for an Array of Micro-cantilevers

The analysis in this section considers a different array of microcantilevers. More precisely, the model refers to a preliminary design, corresponding to the device of Fig. 1.2. In that design, the actuation was supposed to be piezoelectric. Hence, the resulting model is time-invariant and coupling among adjacent cantilevers is only mechanical. Moreover, we assumed that the operating mode of the device would be contact, therefore the model includes the interaction of the cantilevers with the surface forces of a sample in an AFM.

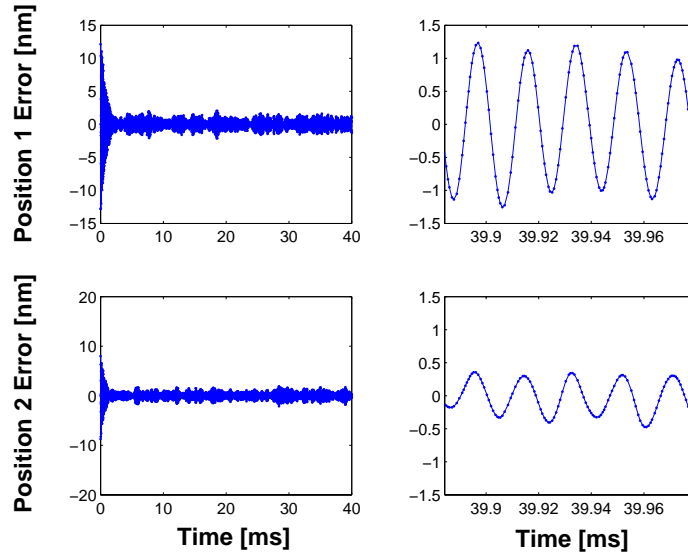


Figure 8.8: Decoupling error in the presence of measurement noise (entire trajectory and detail).

For this system, we formulate and solve the optimal \mathcal{H}_2 control problem. The main goal of this analysis is to provide insights into the architecture of the controller for a multicantilever structure. The solution of the optimal problem leads, as expected, to a distributed controller [98]. However, we are interested in investigating its communication range. More precisely, we want to understand how localized the structure of the optimal controller and its sub-optimal approximations can be, while still retaining a desired performance. From an implementation point of view, this property is crucial, since a localized controller would require to exchange information with fewer units in the array, and therefore result in a simpler circuitry.

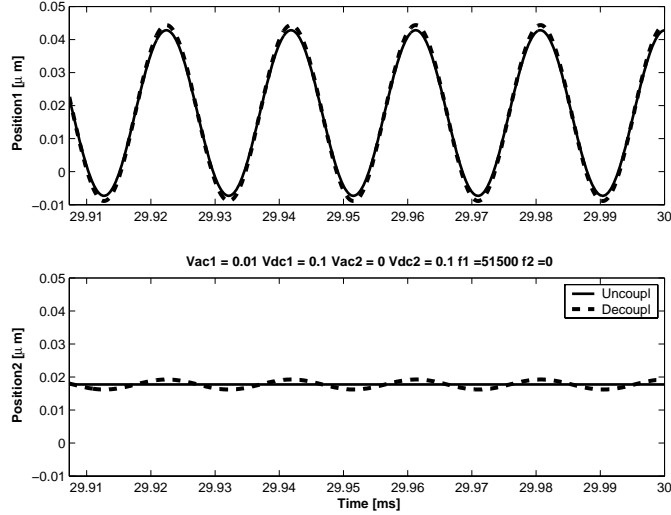


Figure 8.9: Comparison between decoupled and uncoupled oscillation of same cantilevers with a reduced order observer.

8.2.1 Mathematical Model of Microcantilever Arrays with Sample Interaction

In the unimodal approximation, the cantilever-tip-sample system is modeled by a sphere of radius R and mass m , which is suspended by a spring of stiffness k . The deflection from the equilibrium position, Z , which represents the distance from the microcantilever to the sample when only the gravity is acting on it, is measured by x . The interaction with the sample is modeled by the Lennard-Jones potential,

$$V(x, Z) = \frac{A_1 R}{1260(Z + x)^7} - \frac{A_2 R}{6(Z + x)}, \quad (8.1)$$

whose two terms describe, respectively, the short range repulsive forces and the long range attractive forces between the molecules of the tip and those

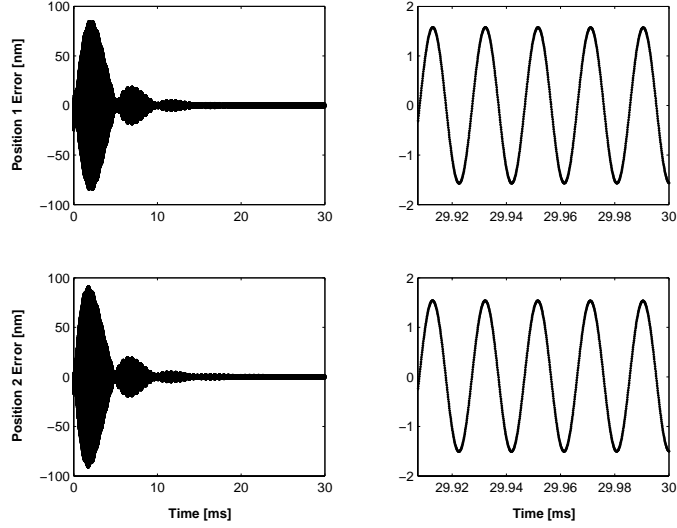


Figure 8.10: Decoupling error with a reduced order observer.

of the surface. A_1 and A_2 are the Hamacker constants for the repulsive and attractive potentials. The net energy of the system scaled by the effective mass m of the cantilever is given by

$$H(x, \dot{x}, Z) = \frac{1}{2}\dot{x}^2 + \frac{1}{2}\omega_1^2 x^2 - \frac{D\omega_1^2}{(Z+x)} + \frac{\sigma^6 D\omega_1^2}{210(Z+x)^7}, \quad (8.2)$$

where, $\omega_1 = \sqrt{\frac{k}{m}}$ is the first modal frequency of the system, $\sigma^6 = \frac{A_1}{A_2}$ and $D = \frac{A_2 R}{6k}$. Note that $H(x, \dot{x}, Z)$, which is the Hamiltonian of the system, is a constant of the dynamics (invariant of motion) since there is no dissipation.

Introducing the state variables $x_1 = x$ and $x_2 = \dot{x}$, we can derive from

(8.2) the equations which govern the dynamics of a single cantilever

$$\dot{x}_1 = x_2 \quad (8.3)$$

$$\dot{x}_2 = -\omega_1^2 x_1 - \frac{D\omega_1^2}{(Z + x_1)^2} + \frac{\sigma^6 D\omega_1^2}{30(Z + x)^8}. \quad (8.4)$$

In order to study the qualitative behavior of the system, it is convenient to perform the following change of variables. By setting $\tau = \omega_1 t$, and dividing the left and right hand sides of (8.3) and (8.4) by $Z_s = \frac{3}{2}(2D)^{\frac{1}{3}}$, we get

$$\xi_1' = \xi_2 \quad (8.5)$$

$$\xi_2' = -\xi_1 - \frac{d}{(\alpha + \xi_1)^2} + \frac{\Sigma^6 d}{30(\alpha + \xi_1)^8}, \quad (8.6)$$

where $\xi_1 = \frac{x_1}{Z_s}$, $\xi_2 = \frac{x_2}{\omega_1 Z_s}$, $d = \frac{4}{27}$, $\alpha = \frac{Z}{Z_s}$, and $\Sigma = \frac{\sigma}{Z_s}$. Notice that the prime denotes the derivative with respect to non-dimensional time τ . Z_s is the critical value of Z , below which the attractive force is greater than the spring force, and in the absence of the repulsive force the surface snaps the tip into contact, [99]. Note that the equations describing the dynamics of the dimensionalized system (8.3) and (8.4) and of the non-dimensionalized one (8.5) and (8.6) are formally the same. Hence, we can study the dynamical behavior of the former, using the equations of the latter.

As α varies over $[0, \infty]$, the number of equilibrium points of the system varies too. In particular in [100] it is shown that there are two critical values of α , α_{sl} and α_{sv} . When $\alpha < \alpha_{sv}$ there is only one equilibrium point. If $\alpha_{sv} < \alpha < \alpha_{sl}$ the equilibrium points become three. Finally, if $\alpha > \alpha_{sl}$ there is again only one equilibrium point.

A multicantilever structure consists of an array of microcantilevers connected to the same beam and is represented schematically in Fig. (8.11).

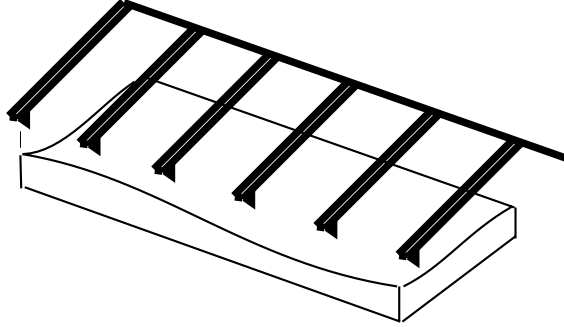


Figure 8.11: A schematic of a multicantilever structure.

Though each cantilever is actuated independently, the presence of the beam implies that its dynamics is affected by the behavior of the others. As a consequence, the model we introduced for the single cantilever has to be modified to take into account this correlation. We have modelled this interaction via a symmetric infinite matrix $a_{i,k}$, so that the state equations for the i -th cantilever become

$$\xi_1'(t, i) = \xi_2(t, i) \quad (8.7)$$

$$\xi_2'(t, i) = -\xi_1(t, i) - \frac{d}{(\alpha + \xi_1(t, i))^2} + \frac{\Sigma^6 d}{30(\alpha + \xi_1(t, i))^8} + \sum_{\substack{k=-\infty \\ k \neq i}}^{+\infty} a_{i,k} \xi_1(t, k). \quad (8.8)$$

Notice that the symbol t from now on denotes the nondimensional time τ introduced above. Moreover, due to the fact that the microcantilevers are similar, the coefficients $a_{i,k}$ satisfy $a_{i,k} = a_{i,-k}$, and decay as k goes to infinity.

Linearization of equations (8.7) and (8.8) around an equilibrium point leads to the following expression for the local model

$$\begin{aligned}\dot{\xi}(i, t) &= \begin{bmatrix} 0 & 1 \\ -1 + \frac{2d}{(\alpha + \bar{\xi}_{1,i})^3} - \frac{4\Sigma^6 d}{15(\alpha + \bar{\xi}_{1,i})^9} & 0 \end{bmatrix} \xi(i, t) + \sum_{j \neq i} \begin{bmatrix} 0 & 0 \\ a_{i-j} & 0 \end{bmatrix} \xi(j, t) \\ &= F \xi(i, t) + \sum_{j \neq i} B_{i-j} \xi(j, t).\end{aligned}$$

If we now apply the discrete Fourier transform in the spatial domain, introduced in Section 2.3, we get the one-dimensional parameterized system

$$\dot{\xi}(\theta, t) = \begin{bmatrix} 0 & 1 \\ a(\lambda) & 0 \end{bmatrix} \xi(\theta, t) + \begin{bmatrix} 0 \\ 1 \end{bmatrix} u(\theta, t), \quad (8.9)$$

where

$$a(\lambda) = -1 + \frac{2d}{(\alpha + \bar{\xi}_{1,i})^3} - \frac{4\Sigma^6 d}{15(\alpha + \bar{\xi}_{1,i})^9} + \sum_{\substack{k=-\infty \\ k \neq 0}}^{\infty} a_k e^{-ik\lambda}. \quad (8.10)$$

8.3 \mathcal{H}_2 Optimal Controller

As shown in [88], once we have parameterized the distributed problem by a family of finite dimensional state space problems through the application of the Fourier transform, we can use the same results of classical finite dimensional \mathcal{H}_2 theory (see [64, 88]). More precisely, after using spatial transforms, the problem can be stated as the minimization of the cost functional

$$J = \frac{1}{2\pi} \int_0^{2\pi} \int_0^{\infty} [\xi(\theta, t)^* Q \xi(\theta, t) + u(\theta, t)^* R u(\theta, t)] dt d\theta$$

subject to

$$\dot{\xi}(\theta, t) = F(\theta) \xi(\theta, t) + B(\theta) u(\theta, t),$$

with $\xi(\theta, 0) = \xi_0(\theta)$. Since the system is stabilizable, its unique solution is given by the feedback control law

$$u(\theta, t) = -R^{-1}(\theta)B^*(\theta)P(\theta)\xi(\theta, t)$$

where $P(\theta)$ is the positive definite solution of the parameter-dependent algebraic Riccati equation

$$F^*(\theta)P(\theta) + P(\theta)F(\theta) + Q(\theta) - P(\theta)B(\theta)R^{-1}(\theta)B^*(\theta)P(\theta) = 0. \quad (8.11)$$

In our case, the state model is given by (8.9), and if we take

$$R = \begin{bmatrix} 1 & 0 \\ 0 & 1 \end{bmatrix} \quad Q = \begin{bmatrix} q & 0 \\ 0 & q \end{bmatrix}$$

the matrix which defines our stabilizing controller is

$$K(\theta) = - \left[a(\theta) + \sqrt{a(\theta)^2 + q} \quad \sqrt{2a(\theta) + 2\sqrt{a(\theta)^2 + q} + q} \right],$$

where $a(\theta)$ is as defined in equation (8.10). Notice that this controller is not a dynamical system: it merely performs algebraic operations on its input data. The fact that $K(\theta)$ is irrational in θ means that the controller needs to look at distant points to compute the control input at each given point. In real time, the feedback control law is implemented using the coefficients of a Laurent series expansion of $K(\theta)$ in an open annulus that contains the unit circle. If $K(z)$ is the analytic extension of $K(\theta)$ in such an annulus, its Laurent power series expansion will be

$$K(z) = \sum_{h=-\infty}^{\infty} K(h)z^h \quad , \quad (8.12)$$

so that the resulting optimal control law is given by

$$u(h, t) = \sum_{i=-\infty}^{\infty} K(i)\xi(h - i, t).$$

From an implementation point of view, the issue of how large is the number of state variables the controller needs to know is crucial. If the Laurent expansion coefficients of $K(\theta)$ decay to zero fast enough, it is reasonable to expect that a satisfactory suboptimal control law can be achieved by truncating the infinite series expansion.

8.4 Suboptimal Controllers and Communication Range

The analytic properties of the feedback matrix $K(\theta)$ have a strong impact on the structure of the optimal control law. By analyzing $K(\theta)$ we want to derive some information concerning the possibility of implementing a suboptimal control law, through the truncation of the above series (8.12). Therefore, it becomes important to determine the decay rate of its coefficients.

This information is related to the location in the complex plane of the singularities of (8.12). More precisely, the decay rate of the coefficients of (8.12) corresponding to positive powers of z is determined by the singularity

$$\theta_M = \min\{\theta(K) \quad : \quad |\theta(K)| > 1\}$$

while for the decay rate of the coefficients corresponding to negative powers

of z we have to consider

$$\theta_m = \max\{\theta(K) \quad : \quad |\theta(K)| < 1\}.$$

From the analytical expression of the matrix $K(\theta)$, it follows that such singularity points are solutions of the equations

$$a(\theta)^2 + q = 0 \tag{8.13}$$

and

$$2a(\theta) + 2\sqrt{a(\theta)^2 + q} + q = 0, \tag{8.14}$$

which are equivalent respectively to

$$a(\theta) \pm i\sqrt{q} = 0, \tag{8.15}$$

and

$$a(\theta) + \frac{q}{4} - 1. \tag{8.16}$$

Analyzing the expression of $a(\theta)$

$$a(\theta) = -1 + \frac{2d}{(\alpha + \bar{\xi}_{1,i})^3} - \frac{4\Sigma^6 d}{15(\alpha + \bar{\xi}_{1,i})^9} + \sum_{\substack{k=-\infty \\ k \neq 0}}^{\infty} a_k e^{-ik\theta},$$

it is easy to see that, when the number of interacting cantilevers N is finite, (8.13) and (8.14) are reciprocal equations of degree N , with N even.

Reciprocal equations with even degree are equations of the form

$$ax^{2k} + bx^{2k-1} + cx^{2k-2} + \dots + rx^k + \dots + cx^2 + bx + a = 0, \tag{8.17}$$

that can be easily rewritten as

$$a(x^k + x^{-k}) + b(x^{k-1} + x^{-k+1}) + c(x^{k-2} + x^{-k+2}) + \dots + r = 0.$$

Defining $t := x + x^{-1}$, it is not difficult to verify that $t^2 - 2 = x^2 + x^{-2}$, $t^3 - 3t = x^3 + x^{-3}$ and, in general, $x^m + x^{-m}$ is a polynomial of degree m in t . It follows that the reciprocal equation (8.17) can be rewritten as an equation of degree k in the variable t . Hence, the solution of a reciprocal equation of degree $2k$ can in general be reduced to solving one polynomial equation of degree k , as well as at most k quadratic equations. In what follows, we use this property to reduce the order of the polynomials defining the singularities and find an explicit analytical expressions for them.

We explicitly consider, at first, the case where the dynamics of each cantilever is affected only by the presence of the two closest cantilevers, i.e. the case where in (8.8) only $a_1 = a_{-1}$ are different from zero. It follows that, from (8.13), we obtain four singularity points, which after some algebraic calculations, are given by

$$\theta_{1,2,3,4} = -\frac{1}{2} \frac{a_0 \pm i\sqrt{q}}{a_1} \pm \frac{1}{2} \sqrt{\left(\frac{a_0 \pm i\sqrt{q}}{a_1}\right)^2 - 4},$$

while from (8.14) we get

$$\theta_{5,6} = -\frac{1}{2} \frac{4a_0 + q - 4}{4a_1} \pm \frac{1}{2} \sqrt{\left(\frac{4a_0 + q - 4}{4a_1}\right)^2 - 4},$$

where in both cases $a_0 = -1 - \frac{2d}{(\alpha + \xi_{1,i})^3} + \frac{4\Sigma^6 d}{15(\alpha + \xi_{1,i})^9}$.

In the simulations that we performed, we set $\alpha = 1.2$ and $\Sigma = 0.03$. For this value of α the nonlinear system has three equilibrium points, therefore it can be associated with three linearized systems. Fig. (8.12) shows how the maximum and minimum modulus singularities, respectively θ_M and θ_m , move as a_1 varies in $[\frac{a_0}{8}, \frac{a_0}{4}]$ for these three systems. As expected, the value of θ_M tends to decrease, while the value of θ_m tends to increase,

meaning that the decay rate of the coefficients becomes slower: as the influence of the neighbouring cantilevers becomes stronger, the controller needs more information to stabilize and optimize the performance of the system.

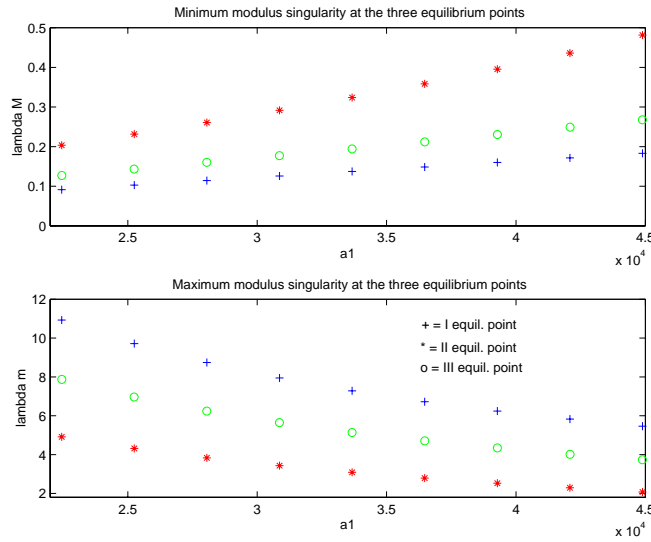


Figure 8.12: Variation of the minimum and maximum modulus singularities.

We then considered the case of four interacting cantilevers. The explicit expression for the singularities is, from (8.13)

$$\theta_{1,\dots,8} = -\frac{a_1}{4a_2} \pm \frac{\sqrt{a_1^2 - 4a_2(a_0 \pm i\sqrt{q} - 2a_2)}}{4a_2} \pm \frac{1}{2} \sqrt{\left(-\frac{a_1}{2a_2} \pm \frac{\sqrt{a_1^2 - 4a_2(a_0 \pm i\sqrt{q} - 2a_2)}}{2a_2}\right)^2 - 4},$$

and from (8.14)

$$\theta_{9,\dots,12} = -\frac{a_1}{4a_2} \pm \frac{\sqrt{a_1^2 - a_2(4a_0 + q - 4 - 8a_2)}}{4a_2}$$

$$\pm \frac{1}{2} \sqrt{\left(-\frac{a_1}{2a_2} \pm \frac{\sqrt{a_1^2 - a_2(4a_0 + q - 4 - 8a_2)}}{2a_2}\right)^2 - 4.}$$

Simulations show that the decay rate of the coefficients of K is slower as in Fig. (8.13).

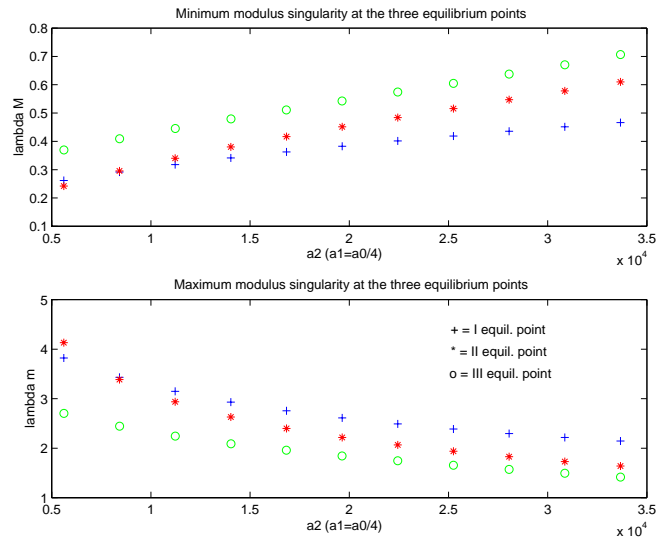


Figure 8.13: Variation of the minimum and maximum modulus singularities.

Chapter 9

Conclusions and Future Directions

9.1 Conclusions

In this dissertation, we have presented the analysis of an electrostatically actuated cantilever array. The device was designed to consist of tightly packed microcantilevers, so that we could investigate the effects of coupling between neighboring microbeams. The interest in this kind of configuration is not merely academic. From a practical point of view, this architecture allows for an increase in throughput, while keeping the size of the device as small as possible.

In our design, each cantilever in the array constitutes the movable plate of a microcapacitor and its displacement can be independently controlled by applying a voltage across the plates. We have shown that the dynamics of a single cantilever are governed by a periodic differential equation,

the Mathieu equation. In the array case, after incorporating the information about coupling, we obtain a set of coupled Mathieu equations, which have been analyzed using results from the theory of spatially invariant distributed parameters systems. These models have been experimentally validated, both in the linear regime of operation, where they can be approximated as time-invariant, and in parametric resonance. The results show very good agreement with the theoretical predictions.

One of the main goals of our research has been the replacement of the direct measurement of the cantilever displacement, commonly performed with optical methods, with an estimate obtained from a state observer. To provide this estimate, the observer uses the current through the cantilevers as sensing signal. The advantage of such an arrangement is the fact that it would result in more compact devices, while retaining or improving the measurement accuracy offered by commercially available instruments. To this end, we have formulated and solved the optimal observer problem for periodic systems. In the architecture we have proposed for the array, the design of the observer is done for each cantilever independently, as if they were decoupled, treating the coupling variables as exogenous inputs. We have shown that with this approach there is no loss in performance, because the problem is naturally “almost” decoupled. The optimal observer design, not necessarily intended for implementation, is used to tune the parameters of a reduced order observer, so that the overall system has the best achievable noise rejection properties.

Finally, we have shown how the dynamics of coupled cantilevers can be “electronically diagonalized” by the use of an appropriate control action.

To illustrate this point, we have presented two examples: an optimal \mathcal{H}_2 design and a decoupling controller. The multicantilever arrays considered in the two cases differ in the model of the coupling interactions. In both cases, we show that by means of a distributed controller, we do not need to impose constraints on the geometrical parameters of the device (in particular, the lateral spacing between cantilevers) to obtain decoupled dynamics. It is the use of control that “diagonalizes” the system.

9.2 Future Directions

The analysis presented in this dissertation, far from being complete, is in a way the starting point for posing other interesting questions that have not been addressed here.

One of the first issues that comes to mind regards the design of a control action to achieve objectives other than the simple decoupling of the dynamics. Now that the physical coupling is eliminated and the cantilevers are indeed independent units, we can think of superimposing a second, fully localized controller to achieve or satisfy performance objectives that will depend on the particular application considered. For instance, one immediate goal could be to reduce the time constant of the system, and speed up the convergence of the decoupling control.

Another issue that deserves more attention regards the assumptions about the cantilever parameters, and in particular the hypothesis that they are all equal. This is not an unreasonable assumption for the nominal parameters of each cantilever, and in fact it is conceivable that in a

typical application we might want to have identical units. However, due to inhomogeneities in the fabrication process and/or slight asymmetries in the device, it is highly likely that there are small discrepancies in these values. Therefore it will be important to consider a robust observer and controller design where we allow for differences between the parameters of the cantilevers, and also uncertainty in their values.

In the past few months we have been working at the implementation of an observer. A prerequisite to its implementation is the ability to measure very small currents (in the order of pA) at high frequencies (in the order of $100kHz$). We have some promising results, but more work needs to be done in terms of characterizing the circuit that measures the current. Moreover, one of the critical questions we are faced with concerns noise and the ability of the circuit to filter it out.

Finally, it will be interesting to test the device in a real implementation, and demonstrate that we can in fact guarantee or even improve the performance of existing devices.

Appendix A

On the Implementation of the Observer

A.1 The Current Measurement

The normal mode of operation for our multicantilever array will have the cantilevers driven close to their resonant frequency. For a sinusoidal input $V = V_o \sin(\omega_o t)$, the current through the cantilevers is given by

$$y = i(t) = \frac{d}{dt}(CV) = c_1 \sin(\omega_o t)z + c_2 \cos(\omega_o t)\dot{z} + v(t), \quad (\text{A.1})$$

where $v(t) = \frac{\epsilon_o A V_o w_o}{d} \sin(\omega_o t)$ and c_1, c_2 , are a function of the system parameters, defined in (5.6). From (A.1) it is easy to see that the current has two components

$$y = i_{mot}(2\omega_o t) + i_{inp}(\omega_o t),$$

with

$$i_{inp} = v(t),$$

depending only on the input, and

$$i_{mot} = c_1 \sin(\omega_o t)z + c_2 \cos(\omega_o t)\dot{z},$$

carrying the information about the cantilever dynamics. This is the “useful” component that the observer uses to reconstruct the cantilever displacement.

The measurement of i_{mot} turned out to be quite challenging. Its amplitude, when the cantilever is in its linear regime of operation, is in the order of few picoamperes, and about two to three orders of magnitude smaller than the amplitude of i_{inp} . Moreover, when the cantilever is driven close to its resonant frequency, i_{mot} has a frequency of about 100kHz. In particular, note that i_{inp} is always at the driving frequency ω_o , while i_{mot} is at $2\omega_o$.

It turned out that there are no off-the-shelf instruments able to perform the measurement of such a small current at such a high frequency. The next section presents the schematic of the circuit we have designed to perform the measurement. The project is a collaboration with Craig Olroyd.

A.2 Circuit Design

Figure A.1 shows diagram of the circuit to measure the current. The circuit is composed of two amplifying stages, to reduce noise and parasitic impedances and obtain an amplification gain of about 10^6 with a bandwidth of 300kHz.

Figure A.2 shows the printed circuit board (PCB) with the circuit and the cantilever die inside one of our IC carriers, during testing. The PCB was custom made so that the circuit could be placed as close as possible to

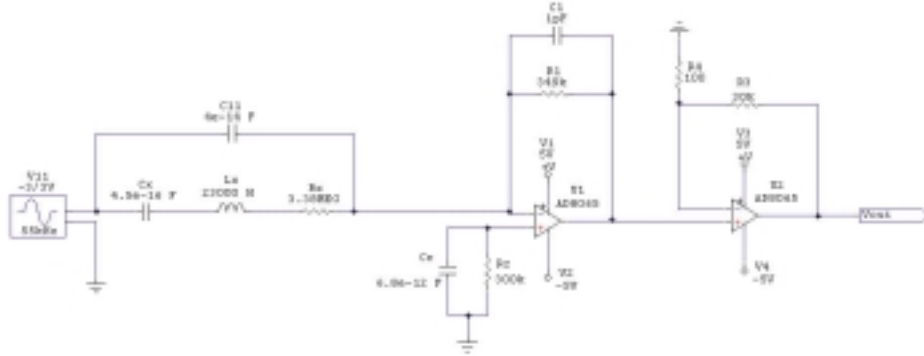


Figure A.1: Schematic diagram of the circuit to measure the current.



Figure A.2: Picture showing the PCB and the cantilever die during testing.

the cantilever die. The output terminal of the cantilever is wire-bonded to the input of the first stage operational amplifier, to further minimize any source of noise and parasitic impedances.

A.3 Offline Implementation of the Observer

Figure A.3 shows the result of a first set of experiments regarding the offline implementation of the optimal observer, using the circuit described above for the measurement of the current. The input applied during this experiment was a sinusoidal function with amplitude $V_o = 300$ mV and frequency $f = 53100$ Hz.

In Section A.1 we noticed that i_{inp} and i_{mot} are respectively at ω_o and $2\omega_o$ and that i_{inp} is the useful component, carrying the information about the cantilever displacement. The small separation in frequency makes the extraction of i_{mot} from the measurement of i difficult, since i_{inp} can be hardly filtered out of i .

Figure A.3 a) represents the output of the circuit, once deprived of the component relative to i_{inp} . In this case, i_{inp} has been subtracted out of i , based on the model of the circuit and the identified parameters of the cantilever. Figure A.3 b) compares the estimate of the cantilever displacement (solid line) obtained with an optimal observer, to measured data (dashed line). Notice how, in spite of the large amount of noise, the optimal observer is able to provide an estimate of the cantilever displacement, not too far off from its actual value. Even though the performance is not satisfactory yet, this result shows that indeed the sensing scheme proposed might be a viable alternative to existing devices. In particular we expect that, once we succeed in reducing the level of noise in the current measurement, this scheme will be able to offer comparable or better accuracy in the reconstruction of the cantilever displacement than the other available sensing schemes.

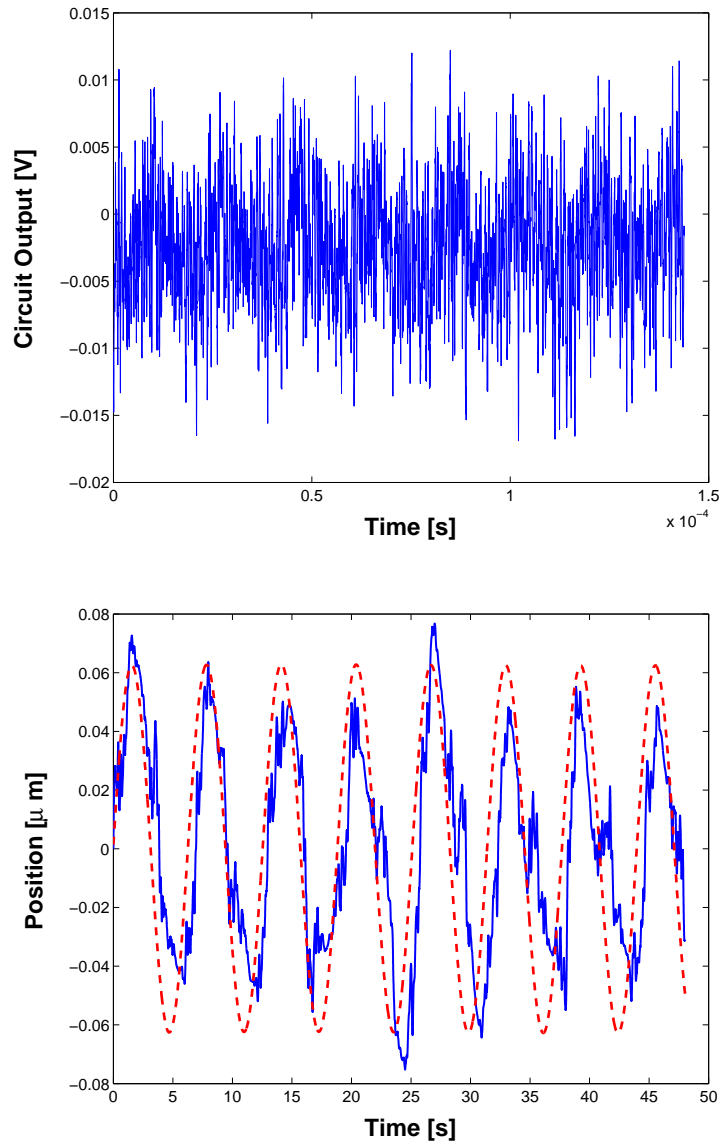


Figure A.3: a) Circuit output due to $i_{mot} =$, b) Comparison between estimated (solid line) and measured (dashed line) cantilever displacement.

Bibliography

- [1] K. Turner, P. Hartwell, and N. Macdonald, “Multi-dimensional MEMS motion characterization using laser vibrometry,” in *Digest of Technical Papers Transducers'99, Sendai, Japan*, 1999.
- [2] G.Tritto, “Needs of microtechnologies for microsurgery. microsurgeons make easy microtechniques.,” in *Proc. 23rd Ann. Int. IEEE Conf. of the Eng. in Med. and Biol. Soc.*, 2001.
- [3] K. Ikuta et al., “Remote microsurgery system for deep and narrow space - development of new surgical procedure and micro-robotic tool.,” in *MICCAI 2002 - 5th Int. Conference, Berlin Germany*, pp. 163–72, 2002.
- [4] Il-seok Son and A.Lal, “A remotely actuated magnetic actuator for microsurgery with piezoresistive feedback.,” in *2nd Annual Int. IEEE-EMBS Conf. on Microtech. in Medicine and Biology*, pp. 332–36, 2002.
- [5] G. Bar et al., “Atomic-scale imaging of anisotropic organic conductors by scanning probe techniques (STM/AFM),” *Ultramicroscopy*,

- vol. 42, pp. 644–52, Jul. 1992.
- [6] S.Ferrero, A.Piednoir, and C.Henry, “Atomic scale imaging by UHV-AFM of nanosized gold particles on mica,” *Amer. Chem. Soc.*, vol. 1, no. 5, pp. 227–30, May 2001.
 - [7] H. Holscher et al., “Imaging of sub-unit-cell structures in the contact mode of the scanning force microscope,” *Amer. Phys. Soc.*, vol. 59, no. 3, pp. 1661–64, Jan. 1999.
 - [8] M. Lutwyche et al., “Microfabrication and parallel operation of 5×5 2d AFM cantilever arrays for data storage and imaging,” in *XI Int. Workshop on MEMS, Heidelberg, Germany*, January 1998.
 - [9] P. Indermhule et al., “Fabrication and characterization of cantilevers with integrated sharp tips and piezoelectric elements for actuation and detection for parallel AFM applications,” *Sensors & Actuators A-Physical*, vol. A60, no. 1-3, pp. 186–190, May 1997.
 - [10] H. Mamin et al., “High density data storage using proximal probe techniques,” *IBM J. Res. Develop.*, vol. 39, no. 6, pp. 681–700, 1995.
 - [11] M. Despont et al., “VLSI-NEMS chip for parallel AFM data storage,” *Sensors & Actuators A-Physical*, vol. A80, no. 2, pp. 100–107, 10 March 2000.
 - [12] P. Vettiger et al., “The millepede - more than one thousand tips for future AFM data storage,” *IBM J. Res. Develop.*, vol. 44, no. 3, pp. 323–40, May 2000.

- [13] E. Snow and P.M.Campbell, "AFM fabrication of sub-10-nanometer metal-oxide devices with in situ control of electrical properties," *Science*, vol. 270, pp. 1639–41, 8 Dec. 1995.
- [14] M. Wendel et al., "Nanolithography with an atomic force microscope for integrated fabrication of quantum electronic devices," *Appl. Phys. Lett.*, vol. 65, no. 14, pp. 1775–77, Oct. 1994.
- [15] S. Minne et al., "Atomic force microscope lithography using amorphous silicon as a resist and advances in parallel operation," *J. Vac. Technol. B*, vol. 13, no. 3, pp. 1380–85, 1995.
- [16] H. Lee et al., "Nanometer-scale lithography on H-passivated Si(100) by atomic force microscope in air," *J. Vac. Sci. Technol. A*, vol. 15, no. 3, pp. 1451–54, June 1997.
- [17] T. Thundat et al., "Chemical, physical and biological detection using microcantilevers," in *Proc. of the 3rd Symp. on Microstructures and Microfabricated Syst., Montreal, Canada*, 1997.
- [18] J. Fritz et al., "Translating biomolecular recognition into nanomechanics," *Science*, vol. 288, pp. 316–318, 14 April 2000.
- [19] C. Britton et al., "Multiple-input microcantilever sensors," *Ultramicroscopy*, vol. 82, no. 1-4, pp. 17–21, Feb. 2000.
- [20] A. Moulin et al., "Microcantilever-based biosensors," *Ultramicroscopy*, vol. 82, pp. 23–31, 2000.

- [21] M. Tortonese, R. Barrett, and C. Quate, "Atomic resolution with an atomic force microscope using piezoresistive detection," *Appl. Phys. Lett.*, vol. 62, no. 8, pp. 834–836, Feb. 1993.
- [22] Y. Shiba et al., "Capacitive AFM probe for high speed imaging," *Trans. of the IEE of Japan*, vol. 118E, no. 12, pp. 647–50, 1998.
- [23] T. Itoh, T. Ohashi, and T. Suga, "Piezoelectric cantilever array for multiprobe scanning force microscopy," in *Proc. of the IX Int. Workshop on MEMS, San Diego, CA*, pp. 451–455, 1996.
- [24] S. Minne, S. Manalis, and C. Quate, "Parallel atomic force microscopy using cantilevers with integrated piezoresistive sensors and integrated piezoelectric actuators," *Appl. Phys. Lett.*, vol. 67, no. 26, pp. 3918–3920, 1995.
- [25] B. Chui et al., "Independent detection of vertical and lateral forces with a sidewall-implanted dual-axis piezoresistive cantilever," *Appl. Phys. Lett.*, vol. 72, no. 11, pp. 1388–1390, March 1998.
- [26] Q. Huang and N. Lee, "A simple approach to characterizing the driving force of polysilicon laterally driven thermal microactuators," *Sensors & Actuators A-Physical*, vol. A80, no. 3, pp. 267–272, 15 March 2000.
- [27] P. Attia et al., "Fabrication and characterization of electrostatically driven silicon microbeams," *Microelectronics J.*, vol. 29, pp. 641–44, 1998.

- [28] N. Blanc et al., “Scanning force microscopy in the dynamic mode using microfabricated capacitive sensors,” *J. Vac. Sci. Technol. B*, vol. 14, no. 2, pp. 901–905, Mar/Apr 1996.
- [29] P. Vettiger et al., “The millepede - nanotechnology entering data storage,” *IEEE Trans. on Nanotech.*, vol. 1, no. 1, pp. 39–55, March 2002.
- [30] A. Kraus et al., “Parametric frequency tuning of phase-locked nanoelectromechanical resonators,” *Applied Physics Letters*, vol. 79, no. 21, pp. 3521–3523, 19 Nov. 2001.
- [31] A. Olkhovets et al., “Non-degenerate nanomechanical parametric amplifier,” in *Technical Digest MEMS 2001, 14th IEEE Int. Conf. on MEMS, Interlaken, Switzerland*, 2001.
- [32] K. Turner et al., “Five parametric resonances in a MicroElectroMechanical system,” *Nature*, vol. 396, no. 6707, pp. 149–156, 12 Nov. 1998.
- [33] M. Yu et al., “Realization of parametric resonances in a nanowire mechanical system with nanomanipulation inside a scanning electron microscope,” *Physical Review B*, vol. 66, no. 073406, pp. 1–4, 2002.
- [34] W. Dougherty et al., “Detection of AC magnetic signals by parametric mode coupling in a mechanical oscillator,” *Measurement Science and Technology*, vol. 7, no. 12, pp. 1733–1739, Dec. 1996.

- [35] D. Rugar and P. Grutter, “Mechanical parametric amplification and thermomechanical noise squeezing,” *Physical Review Letters*, vol. 67, no. 6, pp. 699–702, 5 Aug. 1991.
- [36] M. Napoli et al., “Understanding mechanical domain parametric resonance in microcantilevers,” in *Proc. of the IEEE 16th Annual Int. Conf. on MEMS, Kyoto JP*, pp. 169–172, 2003.
- [37] M. Napoli et al., “Dynamics of mechanically and electrostatically coupled microcantilevers,” in *Proc. of Transducers’03, Boston MA*, 2003.
- [38] S. Alexander et al., “An atomic-resolution atomic-force microscope implemented using an optical lever,” *J. of Appl. Phys.*, vol. 65, pp. 164–67, 1989.
- [39] G.Meyer and N.M.Amer, “Novel optical approach to atomic force microscopy,” *Appl. Phys. Lett.*, vol. 53, pp. 1045–47, 1988.
- [40] C.Schonenberg and S.F.Alvarado, “A differential interferometer for force microscopy,” *Review of Scientific Instruments*, vol. 60, pp. 3131–34, 1989.
- [41] C.T.Nguyen, *Micromechanical Signal Processors*. PhD thesis, University of California at Berkeley, 1994.
- [42] C. Nguyen and R. Howe, “Design and performance of CMOS micromechanical resonator oscillators,” in *IEEE Proceedings 1994 International Frequency Control Symposium*, pp. 127–134, 1994.

- [43] C. Nguyen, “Frequency selective MEMS for miniaturized low-power communication devices,” *IEEE Trans. on Microwave Theory and Technique*, vol. 47, no. 8, pp. 1486–503, 1999.
- [44] M. Napoli et al., “Optimal control of arrays of microcantilevers,” *J. of Dyn. Sys. Meas. and Control*, vol. 121, pp. 686–690, Dec. 1999.
- [45] K.I.Schiffmann, “Investigation of fabrication parameters for the electron-beam-induced deposition of contamination tips used in atomic force microscopy,” *Nanotechnology*, vol. 4, pp. 163–169, 1993.
- [46] Y.Akama, E.Nishimura, and A.Sakai, “New scanning tunneling microscopy tip for measuring surface topography,” *J. Vac. Sci. Technol. A*, vol. 8, no. 1, pp. 429–433, Jan/Feb 1990.
- [47] M. Yamaki et al., “Efficient microtip fabrication with carbon coating and electron beam deposition for atomic force microscopy,” *J. Vac. Sci. Technol. B*, vol. 10, no. 6, pp. 2447–2450, Nov/Dec 1992.
- [48] Digital Instruments, *Scanning Probe Microscopy Training Notebook*. 1998.
- [49] P. Gaucher et al., “Piezoelectric bimorph cantilever for actuation and sensing applications,” *J. Phys. IV France*, vol. 8, pp. 235–238, 1998.
- [50] K. Nagpal and P. Khargonekar, “Filtering and smoothing in an H_∞ setting,” *IEEE Trans. on Automatic Control*, vol. 36, no. 2, pp. 152–66, Feb. 1991.

- [51] Y. Martin et al., “Atomic force microscope force mapping and profiling on a sub 100-Å scale,” *J. of Appl. Phys.*, vol. 61, pp. 4723–29, 1987.
- [52] Polytec, *User Manual - Laser Doppler Vibrometer*. 2002.
- [53] M. Napoli and B. Bamieh, “Modeling and observer design for an array of electrostatically actuated microcantilevers,” in *Proc. 40'th IEEE Conf. on Dec. and Cont., Orlando FL*, December 2001.
- [54] S. Bittanti and P. Bolzern, “Stabilizability and detectability of linear periodic systems,” *Syst. & Cont. Lett.*, vol. 6, pp. 141–145, July 1985.
- [55] T. Chen and B. Francis, *Optimal Sampled-Data Control Systems*. Springer, 1995.
- [56] B. Bamieh et al., “Minimization of the l^∞ -induced norm for sampled-data systems,” *IEEE Trans. on AC*, vol. 38, no. 5, pp. 717–32, 1993.
- [57] K. Chu, “Decentralized control of high-speed vehicular strings,” *Transportation Science*, pp. 361–384, Nov. 1974.
- [58] B. Shu, “Robust longitudinal control of vehicle platoons on intelligent highways,” Master’s thesis, Dept. of ECE, Univ. of Illinois at Urbana-Champaign, 1996.
- [59] S. Melzer and B. Kuo, “Optimal regulation of systems described by a countably infinite number of objects,” *Automatica*, vol. 7, pp. 359–366, 1971.

- [60] C.Ho and Y.Tai, “Review : MEMS and its applications for flow control,” *ASME J. of Fluids Eng.*, vol. 118, pp. 437–447, Sept. 1996.
- [61] T.R.Bewley and S.Liu, “Optimal and robust control and estimation of linear paths to transition,” *J. Fluid Mechanics*, vol. 365, pp. 305–349, June 1998.
- [62] M.R.Jovanović and B.Bamieh, “Frequency domain analysis of the linearized Navier-Stokes equations,” in *Proceedings of the 2003 American Control Conference*, pp. 3190–3195, 2003.
- [63] M.R.Jovanović and B.Bamieh, “Componentwise energy amplification in channel flows,” *Submitted to J. Fluid Mech.*, 2003.
- [64] E. W. Kamen, “Stabilization of linear spatially-distributed continuous-time and discrete-time systems,” in *Multidimensional Systems Theory* (N. Bose, ed.), Hingham, MA: Kluwer, 1985.
- [65] R. Baskaran et al., “Experimental characterization of an electrostatically coupled oscillator MEM filter,” in *Proc. of the SEM annual meeting, MEMS symposium, Milwaukee, WI*, 2002.
- [66] W. Zhang et al., “Effect of cubic nonlinearity on auto-parametrically amplified resonant MEMS mass sensor,” *Sensors & Actuators A-Physical*, vol. A102, no. 1-2, pp. 139–150, 1 Dec. 2002.
- [67] W.Zhang, R.Baskaran, and K.Turner, “Tuning the dynamic behavior of parametric resonance in a micromechanical oscillator,” *Applied Physics Letters*, vol. 82, no. 1, pp. 130–2, 1 Jan. 2003.

- [68] J. Rhodes et al., “Parametrically excited mems-based filters,” in *Proc. of IUTAM 2003, Italy*, 2003.
- [69] E. Watcher and T. Thundat, “Micromechanical sensors for chemical and physical measurements,” *Rev. Sci. Instrum.*, vol. 66, no. 6, pp. 3662–67, 1995.
- [70] T. Thundat et al., “Microcantilever sensors,” *Microscale Thermophysical Engineering*, vol. 1, pp. 185–199, 1997.
- [71] P. Datskos and I. Sauer, “Detection of 2-mercaptoethanol using gold-coated micromachined cantilevers,” *Sensors & Actuators B*, vol. 61, pp. 75–82, 1999.
- [72] J. Yang et al., “Mechanical behavior of ultrathin microcantilever,” *Sensors & Actuators*, vol. 82, pp. 102–7, 2000.
- [73] M. Ward and D. Buttry, “In situ interfacial mass detection with piezoelectric transducers,” *Science*, vol. 249, pp. 1000–1007, 1990.
- [74] K. Giwzewski et al., “Observation of a chemical reaction using a micromechanical sensor,” *Chem Phys. Letters*, vol. 217, no. 5-6, pp. 589–93, 1994.
- [75] J. Lai et al., “Optimization and performance of high-resolution micro-optomechanical thermal sensors,” *Sensors & Actuators A*, vol. 58, pp. 113–19, 1998.
- [76] G. Barnes et al., “A femtojoule calorimeter using micromechanical sensors,” *Rev. Sci. Instrum.*, vol. 65, no. 12, pp. 3793–98, Dec. 1994.

- [77] M. Viani et al., “Small cantilevers for force spectroscopy of single molecules,” *J. App. Phys.*, vol. 86, no. 4, pp. 2252–62, 1999.
- [78] A. D.T.Mook, *Nonlinear Oscillations*. John Wiley & sons, New York, 1979.
- [79] M.Cartmell, *Introduction to Linear, Parametric and Nonlinear Vibrations*. Chapman and Hall, 1990.
- [80] N. McLachlan, *Theory and Applications of the Mathieu Functions*. Oxford University Press, London, 1951.
- [81] M. Farkas, *Periodic Motions*. NY Springer Verlag - Applied Mathematical Sciences, 1994.
- [82] V. Arnold, *Mathematical Methods of Classical Mechanics*. Springer, 1988.
- [83] R. Rand, *Lecture Notes on Nonlinear Vibrations*. available online <http://www.tam.cornell.edu/randdocs/>, 2001.
- [84] E.Mathieu, “Mémoire sur le mouvement vibratoire d’une membrane de forme elliptique,” *Jour. de Math. Pures et Appliquées*, vol. 13, p. 137, 1868.
- [85] G. J. Michael, “Explicit stability criteria for the damped Mathieu equation,” *IEEE Trans. on Automatic Control*, vol. 12, no. 3, pp. 337–338, June 1967.
- [86] W. J. Rugh, *Linear System Theory*. Prentice Hall, 1993.

- [87] M. Vidyasagar, *Nonlinear Systems Analysis*. SIAM, 1993.
- [88] B.Bamieh, F.Paganini, and M.A.Dahleh, "Optimal control of distributed actuator and sensor arrays," in *Proc. SPIE 5'th Ann. Intl. Symp. on Smart Structures and Materials, San Diego Ca*, March 1998.
- [89] D. Sarid, *Scanning Force Microscopy*. Oxford University Press, New York, 1994.
- [90] S. Salapaka et al., "High bandwidth nano-positioner: A robust control approach," *Review of Scientific Instruments*, vol. 73, no. 9, pp. 3232–41, 2002.
- [91] A. Daniele et al., "Piezoelectric scanners for atomic force microscopes: design of lateral sensors, identification and control," in *Proc. of the 1999 American Control Conference, San Diego, CA*, June 1999.
- [92] K. Turner, *Applications and Analysis of Parametric Resonance in Microelectromechanical Systems*. PhD thesis, Cornell University, 1999.
- [93] F.D.Bannon, J.R.Clark, and C.T.C.Nguyen, "High-Q HF microelectromechanical filters," *IEEE J. of Solid-State Circuits*, vol. 35, no. 4, pp. 512–26, April 2000.
- [94] T. D. Rossing and N. H. Fletcher, *Principles of Vibration and Sound*. Springer, 1999.

- [95] M.Green and D. Limebeer, *Linear Robust Control*. Prentice Hall, 1995.
- [96] M. Napoli et al., “Mathematical modeling, experimental validation and observer design for a capacitively actuated microcantilever,” in *Proc. 2003 IEEE Amer. Control Conf., Denver CO*, 2003.
- [97] M. Lutwyche et al., “ 5×5 2D AFM cantilever arrays a first step towards a Terabit storage device,” *Sensors & Actuators A - Physical*, vol. 73, no. 1, pp. 89–94, Mar. 1999.
- [98] B. Bamieh, F. Paganini, and M. Dahleh, “Distributed control of spatially invariant systems,” *IEEE Trans. on AC*, vol. 47, no. 7, pp. 1091–107, 2002.
- [99] M. Ashhab et al., “Control of chaos in atomic force microscopes,” in *Proc. 1997 IEEE Amer. Control Conf., Albuquerque NM*, June 1997.
- [100] M. Ashhab et al., “Melnikov-based dynamical analysis of microcantilevers in scanning probe microscopy,” in *UCSB Technical Report*, 1997.